Manipulating Carrier Polarization in Pure and Doped Metal Oxide Semiconductor Nanocrystals

by

Chenwei Zhang

A thesis
presented to the University of Waterloo
in fulfillment of the
thesis requirement for the degree of
Master of Science
in
Chemistry

Waterloo, Ontario, Canada, 2021

AUTHOR'S DECLARATION

I hereby declare that I am the sole author of this thesis. This is a true copy of the thesis, including any required final revisions, as accepted by my examiners.

I understand that my thesis may be made electronically available to the public.

Abstract

Moore's Law will soon be inadequate to keep up with the needs of technological developments as the currently used materials have reached their natural performance limits. Hence, the development of a new technology to replace traditional semiconductor electronics is imminent. Spintronics has been emerged as a promising alternative to control charge properties as well as electron spin to improve the device performance. Metal oxide and chalcogenide semiconductor nanocrystals (NCs) have generated much research due to their unique properties and relatively low cost. In contrast to noble metal nanoparticles (NPs), the semiconductor NCs with tunable free charge carrier concentration are regarded as promising materials in technological applications including multifunctional quantum devices and next-generation electronic devices. In this thesis, I investigated the magnetoplasmon resonances in antimony-doped SnO_2 NCs and demonstrated the defect-related excitonic band splitting in ZnO and SnO_2 NCs.

In the first major chapter, I featured the influence of the synthesis methodology and post-synthesis treatment on the plasmonic properties of Sb-doped SnO_2 NCs. I successfully synthesized the nanocrystal (NC) samples having various doping concentrations by two different approaches and found that Sb-doped SnO_2 NCs prepared by solvothermal method display strong localized surface plasmon resonance (LSPR) in the near-infrared (NIR) region, which is absent in the coprecipitation-synthesized NCs. After the thermal annealing process, the LSPR absorption appears in the NCs prepared by the coprecipitation method, and increases in intensity in solvothermally-synthesized NCs. These NCs were investigated by magnetic circular dichroism (MCD) spectroscopy. The raise in excitonic MCD intensity coincides with

that in plasmon absorption upon extending annealing durations. Furthermore, the plasmon intensity is correlated to the oxidation of Sb^{3+} to Sb^{5+} ions by using X-ray photoelectron spectroscopy. The results showcase that the synthesis approach and post-synthesis processing can significantly impact the plasmonic properties of aliovalently-doped semiconductor NCs through the dopant oxidation state.

In the other major chapter, I first demonstrated the carrier polarization related to oxygen deficiencies in ZnO and SnO_2 NCs. The ZnO NC samples showing various defect-related photoluminescence (PL) emission were synthesized by the non-injection method under oxidizing and reducing conditions. The as-prepared ZnO NCs present distinct variable-field and variable-temperature MCD spectra, indicating their different defect concentrations that lead to varying degrees of excitonic band splitting. Upon thermal annealing in an oxygen-rich atmosphere, the Curie-type decay associated with unpaired localized electrons vanished as shown by temperature-dependent MCD measurements, verifying the loss of paramagnetism due to the filling of oxygen vacancies. Similar to ZnO NCs, SnO_2 NCs also exhibit such magneto-optical properties, and their defect-related carrier polarization and Zeeman splitting could also be controlled by synthesis conditions and post-synthesis treatment. Taken together both NC samples, the results corroborate the defect-induced carrier polarization and NC band splitting in ZnO and SnO_2 NCs without introducing additional magnetic dopants.

The result of this thesis provides an ability to manipulate charge carrier polarization in pure and doped metal oxide semiconductor NCs and opens up a window for the application of spintronics.

Acknowledgements

First, I would like to express my great gratitude to my supervisor Dr. Pavle V. Radovanovic for his guidance during my master's study. I am inspired a lot by his enthusiasm and rigour towards science.

I would like to acknowledge my advisory committee members, Dr. Michael Pope and Dr. Jonathan Baugh for their advice and encouragement. I would also like to thank Dr. Pu Chen's group for giving me access to the centrifuge.

I would like to thank my past and current co-workers, Paul, Penghui, Natalie, Yufeng, Shuoyuan, Yi, Nathaniel, Mahdieh, Wenhuan, Archisman, Victor, I-husan, Khue, Aaron, and Wilson for their support in my program. Special thanks to Paul, Penghui, and Wenhuan for their help in my study and life.

Last but not least, I am grateful to my parents and my girlfriend Qiuyu Shi for all their patience, support, and love.

Dedication

I would like to dedicate this thesis to my dad Zhenguo Zhang and mom He Feng for their undivided love and tremendous support.

Table of Contents

List of Figures

List of Tables

List of Abbreviation

ATO	Antimony-doped Tin Oxide
AZO	Aluminum-dope Zinc Oxide
bcc	Body-Center Cubic
CB	Conduction Band
CD	Circular Dichroism
DDA	Dodecylamine
DDOL	1-Dodecanol
DMSs	Diluted Magnetic Semiconductors
DMSOs	Diluted Magnetic Semiconductor Oxides
EDX	Energy Dispersive X-ray
FIR	Far-Infrared
FTIR	Fourier Transform Infrared Spectroscopy
FWHM	Full Width of Half Maximum
ICO	Indium-doped Cadmium Oxide
LCP	Left Circularly Polarized
LO	Longitudinal Optical
LSPR	Localized Surface Plasmon Resonance
MCD	Magnetic Circular Dichroism
MIR	Mid-Infrared
NCs	Nanocrystals
NIR	Near-Infrared

NPs	Nanoparticles
NWs	Nanowires
OA	Oleic Acid
OAm	Oleylamine
ODE	1-Octadecene
PL	Photoluminescence
QDs	Quantum Dots
RBF	Round Bottom Flask
RCP	Right Circularly Polarized
Tc	Curie Temperature
TCE	Tetrachloroethylene
TCO	Transparent Conducting Oxide
TEM	Transmission Electron Microscopy
TO	Transverse Optical
TOPO	Tri-n-octylphosphine Oxide
UV-Vis-NIR	Ultraviolet-Visible-Near-Infrared
VB	Valence Band
XPS	X-ray Photoelectron Spectroscopy
XRD	Powder X-ray Diffraction

Chapter 1
Introduction

1.1 Plasmonic Properties in Semiconductor Nanocrystals

The glass of the Lycurgus cup is one of the earliest remaining examples of a dichromic material that shows different colours in transmission and reflection. The exploration of this unique phenomenon has never stopped, although at that time the techniques and knowledge to study this nanoscopic material were scarce and primitive. With the progress of nanoscience and nanotechnology, people have gradually constructed a well-established system to explain the plasmonic optical-effects of noble metals that mostly occur in the range of visible light. Meanwhile, though, the research field of plasmonics has been also extended to some certain semiconductor nanocrystals (NCs) with such optical properties in the infrared region. At the heart to evaluating plasmonic properties is to understand the localized surface plasmon resonance, abbreviated as LSPR.

1.1.1 Localized Surface Plasmon Resonance

The LSPR is defined as coherent free electron oscillations at the interface between two media with positive and negative dielectric constants,[1] and these oscillations can robustly enhance optical fields on surfaces.[2] The plasma is a result of the collective oscillation of the electron "gas" in a metal or a semiconductor excited with an external electric field.[3] Surface plasmons are electron "gas" oscillations at the interface, which can be excited by external

incident light.[4] The photons can couple with surface plasmons only if the frequencies of incident electromagnetic waves correspond to those of free electrons at the interface.[3] Moreover, when surface plasmons are confined in NPs with a size comparable to or smaller than the wavelength of the incident light, these free electrons can contribute to collective oscillations, commonly termed LSPR modes (Figure 1.1).[5]

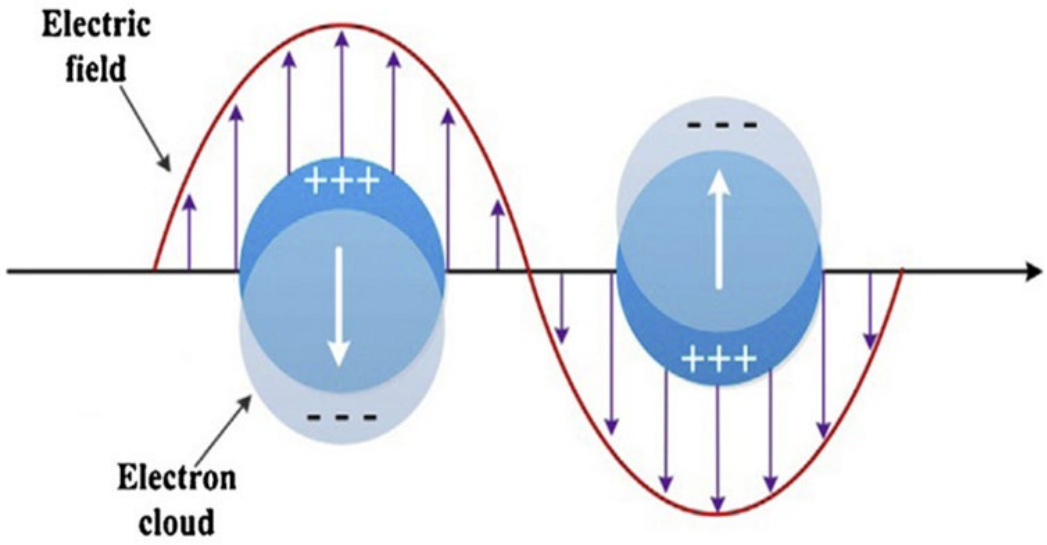

Figure 1.1 Schematic illustration of the LSPRs of a spherical nanoparticles excited by incident light. The collective oscillations are induced by the oscillating electromagnetic field of incident light.[3]

LSPRs recently have been drawing attention of many physicists, chemists, and engineers, and numerous studies have been conducted to explore these optical properties. The class of materials with LSPR properties, known as plasmonic NCs, have been applied in chemical probes,[6] biomolecular sensors,[6] as well as energy storage devices.[7] As previous studies demonstrated, natural LSPR frequencies of noble metal nanoparticles (NPs) like gold

(Au) and silver (Ag) lie in the range of the visible spectrum owing to high free carrier concentration.[8] Most interestingly, the LSPR is not restricted in metal NPs, however, it also exists in some n-type metal oxide NCs (Figure 2, top panel), p-type copper chalcogenide NCs (Figure 2, bottom panel), as well as given metal nitride/phosphide and aliovalently-doped Si NCs (Figure 2, bottom panel). The plasmonic semiconductor NCs usually have a large free carrier concentration to exhibit LSPR properties from near- to mid-infrared spectral range.[9] Furthermore, in contrast to that of noble metals, the free charge carrier concentration of semiconductor NCs is tunable,[9] which causes LSPR spectra ranging from visible to far-infrared (FIR).[10]

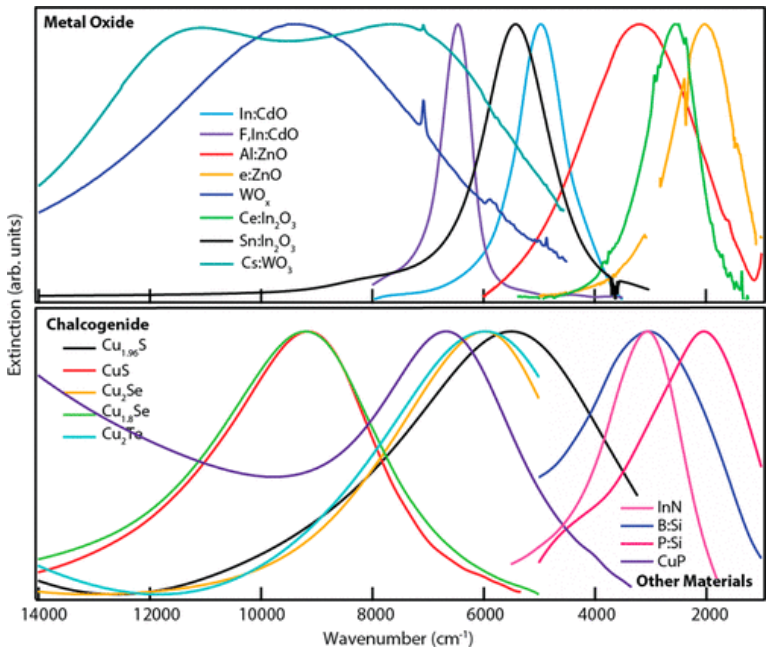

Figure 1.2 LSPR extinction spectra of metal oxide (top panel), copper chalcogenide (bottom panel), and other plasmonic nanocrystal materials such as InN, boron- and phosphorus-doped Si, and CuP (bottom panel).[1]

1.1.2 Physical Models in Plasmonic Semiconductor NCs

The LSPR orienting free electrons in semiconductor NCs can be quantitatively evaluated through solving Maxwell's equations on the basis of light-matter interaction theory. For simplicity, we will concentrate on the case of semiconductor NCs with spherical shapes and isotropic dielectric constant. Therefore, Mie theory is suitable for solving Maxwell's equations. For other geometric NCs, Maxwell's equations usually need to be settled by numerical computational methods.

Mie theory, a theory characterizing absorption and scattering of plane electromagnetic waves, is the simplest way to describe and understand LSPR properties.[11] Equation (1.1) depicts the calculation of the extinction cross section (C_{ext}) of a metal nanosphere:

$$C_{ext} = \frac{24\pi^2 R^3 {\varepsilon_m}^{3/2}}{\lambda}\left[\frac{\varepsilon_i}{(\varepsilon_r + 2\varepsilon_m)^2 + {\varepsilon_i}^2}\right] \qquad (1.1)$$

where λ is the excitation wavelength, R is the radius of the metal nanosphere, ε_m is the relative dielectric constant of the surrounding medium, and ε_r and ε_i are the real part and imaginary part of dielectric functions of the metallic NP, respectively.[12]

According to this equation, the dielectric function of NPs including a real part ε_r and an imaginary part ε_i will determine the magnitude of C_{ext}. When the denominator of the bracketed part approaches zero, *i.e.*, ε_r would usually be negative and equal to -2ε_m and ε_i is approximately close to zero, C_{ext} will become infinitely large, leading to exceedingly strong optical absorption and scattering under this criterion.[5] Although it is impractical to find a kind

of dielectric with ε_r close to -2ε_m, this theory still offers a guideline to enhance LSPRs by seeking a material with both a negative ε_r and a nil ε_i.

A common way to tune LSPR properties is by altering the free carrier concentration, which is based on the Drude-Lorentz theory.[13] The Drude-Lorentz theory of the free electron "gas" in metals applies to predicting and understanding the LSPR properties of both metals[14] and semiconductors.[15] The dielectric function of the Drude-Lorentz theory is a complex function.[16]

$$\varepsilon_p(\omega) = \varepsilon_r(\omega) + i\varepsilon_i(\omega) = \left[\varepsilon_b - \frac{{\omega_p}^2}{(\omega^2+\gamma^2)}\right] + i\frac{{\omega_p}^2\gamma}{\omega(\omega^2+\gamma^2)} \qquad (1.2)$$

Here, ε_p is the dielectric constant of the plasmonic media, ε_b is the background dielectric constant from the bound electrons in the crystal, γ is the damping rate, and ω_p is the bulk plasma frequency that is depicted as:

$$\omega_p = \sqrt{\frac{Ne^2}{m^*\varepsilon_0}} \qquad (1.3)$$

where m^* is the effective mass of a free electron, e is the electron charge, ε_0 is the vacuum dielectric constant, and N is the free carrier concentration.[16]

For the LSPR frequency (ω_{LSPR}) of NPs, the Equation (1.3) can be modified as:[17]

$$\omega_{LSPR} = \sqrt{\frac{{\omega_p}^2}{1+2\varepsilon_m} - \gamma^2} \qquad (1.4)$$

The equation above clearly explains the frequency position of the bulk plasmon material. ω_p is proportional to the square root of free carrier density, and ω_{LSPR} depends on the LSPR peak-broadening factor γ.[18] Moreover, the absorption coefficient (α_{el}) of free electrons is linearly dependent on *N*:[19]

$$\alpha_{el} = \frac{Ne^2}{m^* \varepsilon_0 c \tau \omega^2} \qquad (1.5)$$

where τ is the mean free time between two electron scattering events,[20] also known as relaxation (damping) time,[19] and ω and c are the frequency and speed of light, respectively.

Theoretically, the tunability of LSPR absorption and other properties can be simply achieved by modulating the dopant concentration as described in Equations (1.3), (1.4), and (1.5). One group collected and plotted data (Figure 1.3) for LSPR frequency of NCs for different free carrier densities.[21] The figure illustrates that noble metals (Au and Ag) have significantly larger LSPR frequencies than those of degenerately doped semiconductors. Semiconductors have a wide range of LSPR frequencies relying on tunable doping density (shown in Figure 1.4).[22] The fixed free carrier concentration and the high cost of noble metals generally limit their applications.

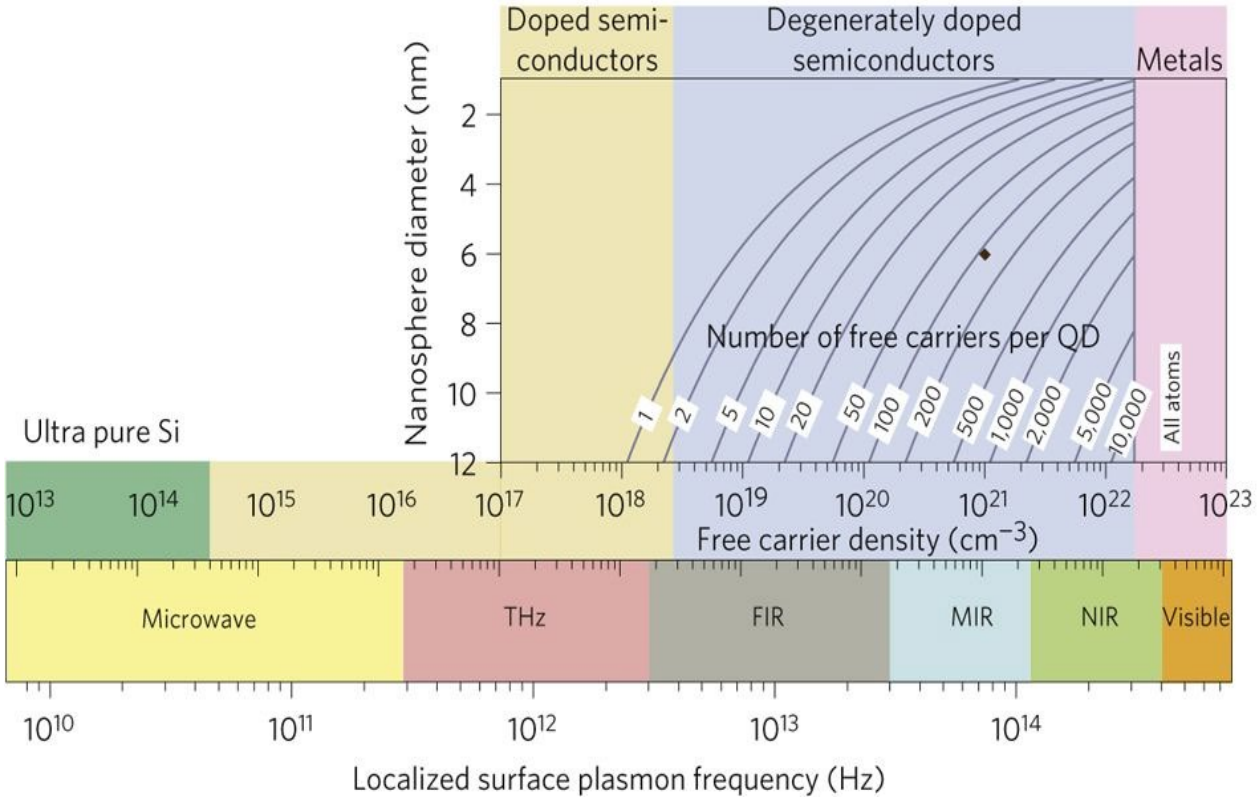

Figure 1.3 Illustration of the LSPR frequency dependence on free carrier concentration and doping constraints in quantum dots (QDs) of metals, doped, and degenerately doped semiconductors.[21]

While increasing the free carrier density shifts LSPRs toward higher frequencies, it brings about considerable optical loss, attributed to two reasons: (i) higher doping levels will increase the imaginary part of the dielectric function in Equation (1.1), leading to C_{ext} declining and a further decrease in LSPRs absorption,[23] and (ii) an increase in a damping constant,[24] which is the rate of energy loss from a free carrier excitation.[1] Several scattering mechanisms impacting energy loss containing electron-electron/hole-hole scattering

($\gamma_{e-e/h-h}$), electron/hole-impurity scattering ($\gamma_{e/h-im}$), electron/hole-phonon scattering ($\gamma_{e/h-ph}$), inter or intraband transition scattering (γ_{ib}), as well as surface scattering (γ_s) have been studied in recent years.[1] Matthiessen's rule provides a succinct equation to describe the interplay among these factors:[23,25]

$$\gamma = \sum \gamma_i = \gamma_{e-e/h-h} + \gamma_{e/h-ph} + \gamma_{ib} + \gamma_s + \gamma_{e/h-im} + \cdots \qquad (1.6)$$

In semiconductor NCs, impurities and vacancies play a salient role in scattering, which contributes to defect scattering ($\gamma_{e/h-im}$).[26] As a result of small sizes of NCs, surface scattering can also impact damping significantly.[23] On the other hand, electron-electron or hole-hole scattering cannot dominate damping due to minor interactions between them.[22] Generally, the overlap between free carrier excitation and inter- or intraband excitation in semiconductors is small, imposing a slight influence on inter- or intraband transition scattering (γ_{ib}).[27] Electron/hole-phonon scattering can be considered as a significant contributor to damping only at high temperatures.[24] These scattering factors can shape an LSPR spectrum, *i.e.*, the higher the damping, the broader the resonance.[28] Overall, an improved understanding of the free carrier concentration and damping factors can guide the development of semiconductor NCs with targeted LSPRs properties.

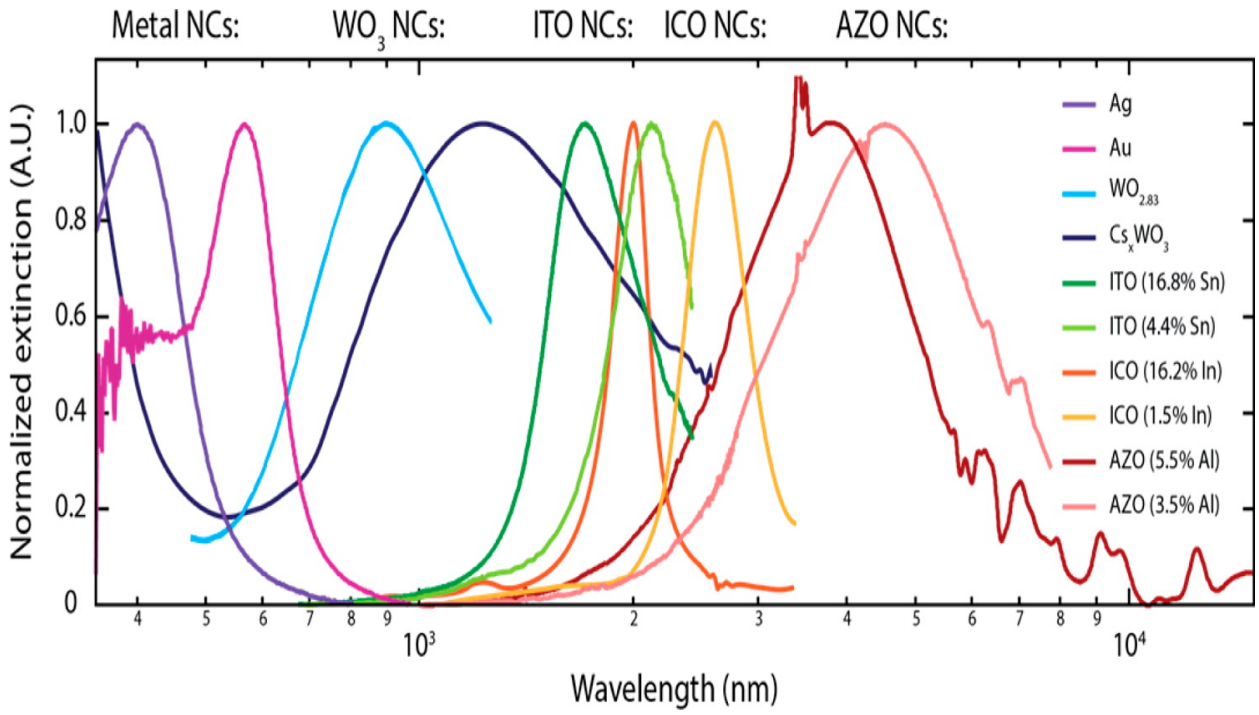

Figure 1.4 Normalized optical extinction spectra of LSPRs in solutions and films of metals NPs such as Ag and Au, and metal oxides NCs such as $WO_{2.83}$, Cs_xWO_3, ITO, ICO, and AZO semiconductor NCs.[22]

1.1.3 Contributing Factors and Dynamic LSPR Modulation in Semiconductor NCs

There are several approaches to tune the free carrier concentration and/or LSPR damping, and then achieve plasmonic frequency modulation in semiconductor NCs. The contributing factors based on the In_2O_3 nanocrystal (NC) system can be summarized as NC size,[29] crystal structure,[30] surface depletion,[31] ensemble broadening,[32] strain effect,[33] and dopant distribution.[34] Crockett *et al.* discovered that the LSPR energy of ITO NCs having nearly identical doping concentration and distribution increases with increasing the NC size,

suggesting higher carrier concentration for larger ITO samples.[29] Wang *et al.* synthesized two types of ITO NCs with different crystal structures, body-center cubic (bcc) structure and metastable corundum structure. Interestingly, they observed strong LSPR behaviour in bcc-ITO NCs but lacking LSPR in corundum phase ITO NCs.[30] It is proposed that for the corundum ITO samples, the band gap energy and separation between the donor state and the conduction band bottom are comparatively large, resulting in high dopant activation energy, and therefore lacking appreciable free electrons in the NCs. Zandi *et al.* found that the depletion layer of ITO NCs could weaken the near-field effect and the LSPR sensitivity to the surrounding environment.[31] Johns *et al.* compared ensemble and single ITO and AZO NC, and demonstrated that the ensemble ones exhibit higher LSPR energy and broader LSPR band width associated with the size, shape, and dopant heterogeneity.[32] Runnerstrom *et al.* showed that compared with ITO NCs, Ce-doped In_2O_3 NCs show remarkably narrower LSPR band width but the similar LSPR energy.[33] They explained that Ce^{4+} ions have relatively similar sizes with In^{3+}, which could minimize the lattice stain to enhance electron mobility, thus reduce LSPR band width. Lounis *et al.* synthesized two series of ITO NCs using different precursors and ligands, and they noticed that these two series of samples have diverse dopant activation energy and different LSPR line shapes, imputing the hybridization between the interstitial oxygen atoms and Sn orbitals near the surface vicinity.[34]

Dynamic LSPR modulation is feasible through change the charge carrier concentration owing to the nature of semiconductor NCs as host materials. Generally, three different approaches have been demonstrated: (1) chemical redox reaction; (2) photochemical charging; and (3) electrochemical charging/discharging.

A chemical redox reaction is one of the commonest ways to tune the LSPR due to its high sensitivity of addition or subtraction of a small amount of free charge carriers.[35,36] Non-stoichiometric $Cu_{2-x}Se$ NCs exhibit reversibly tunable LSPR responses from ca. 0.5 eV to ca. 1.0 eV *via* redox tuning of the Cu stoichiometry.[35] As Figure 1.5 shows, the LSPR absorption of Cu_2Se NCs can be controlled by around 600 nm with the addition of oxidizing agents Ce(IV) or exposure to air (O_2). The reason can be attributed that this oxidation process increases copper deficiency, leading to the increase of free charge carriers which are holes in this case and enhancing the LSPR. On the contrary, the LSPR could be reverted by adding reducing agents such as Cu(I) complex which would decrease copper deficiency followed by lessening the charge concentration and red shifting the LSPR peak. Because of the simple manipulation of redox reaction and extremely robust LSPR response, people apply this robust approach to track electron transfer in complex media, which could detect the optical changes as low as 1 e^- per NC.

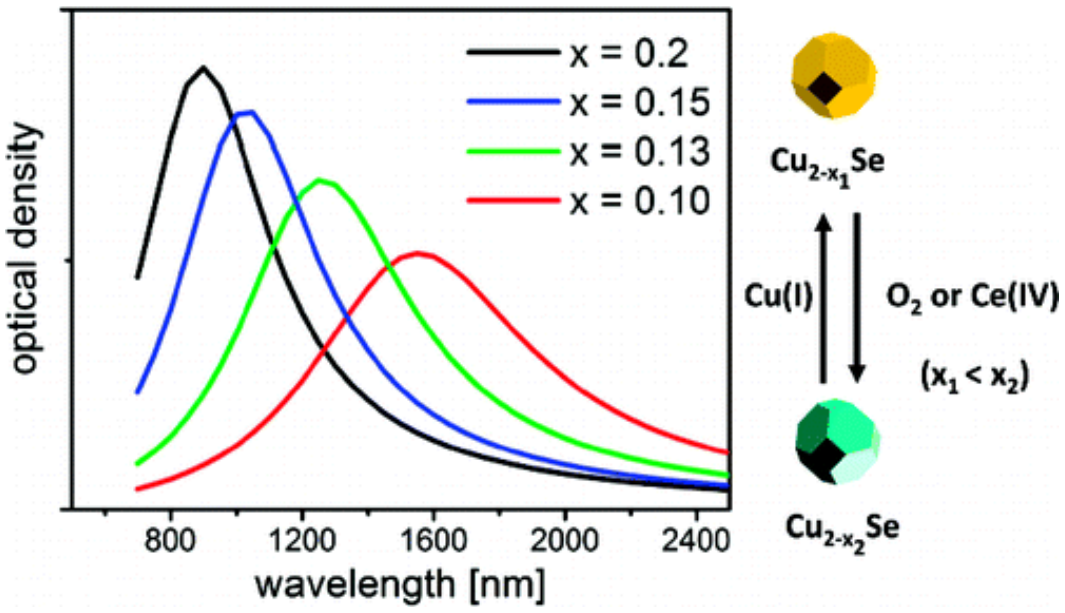

Figure 1.5 Left figure: extinction spectrum of $Cu_{2-x}Se$ NCs with varying stoichiometry. Right figure: the schematic of reversible oxidation/reduction of $Cu_{2-x}Se$ NCs. Oxidizing step is occurred by addition of Ce (IV) or exposure to atmosphere. Reducing step is occurred by adding Cu(I) complex.[35]

Photochemical charging has been considered as a universal approach to dynamically control electron density, thus the LSPR absorption in semiconductor NCs.[37,38] Photochemical charging has been extensively studied on ZnO NCs. It has been found that upon UV illumination, ZnO NCs display a sharp IR peak concomitant with a strong bleach of the interband transition and quenching of photoluminescence (Figure 1.6).[39] This IR absorption eventually is assigned as LSPR behaviour instead of the intra-conduction-band single-electron transitions by Faucheaux *et al.* in the light of three observations.[40] First, they found that the IR peak shifted to higher energy under subsequent charging. Second, the LSPR-based calculation for carrier density of charged NCs was consistent with the reported values collected by chemical titration. Third, compared with a NC dispersion, the IR band red-shifted with the increase of electromagnetic coupling in a film of NCs.

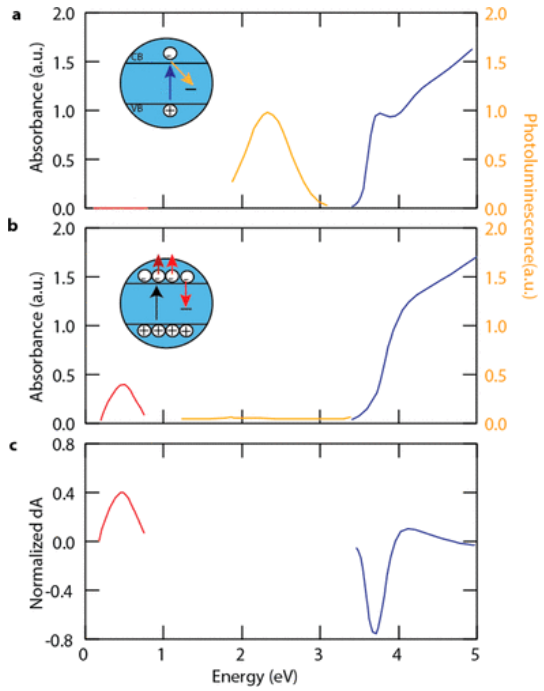

Figure 1.6 Photoexcitation spectra of ZnO NCs: (a) as-synthesized ZnO; (b) charged ZnO; and (c) differential plot.[1] Infrared absorbance peak appears in charged ZnO (red curve in b) due to free electron excitation, but disappears in as-synthesized ZnO (red curve in a). Visible absorption blue shifts to higher energy due to Burstein-Moss effect (blue curve in a, b, and c), and PL emission is quenched owing to the enhancement of Auger recombination (yellow curve in a and b).

Electrochemical charging/discharging is also used to tune the LSPR behaviour as an external voltage can accumulate or deplete charge carriers near their interfaces and surfaces, thus modulate the free charge carrier concentration in semiconductor NCs. Llorente *et al.* demonstrated that the LSPR in p-type Cu_2Se NCs can be well-controlled by potentiostatic potential switching, indicating the free charge carrier (hole) concentration can be modulated electrochemically (Figure 1.7).[41] Similarly, people also demonstrated that this electrochemical way is suitable for n-type semiconductor NCs. Garcia *et al.* achieved the reversible controlling

of LSPR in ITO NCs thin film where the carrier (electron) concentration could be altered by a factor of three.[10]

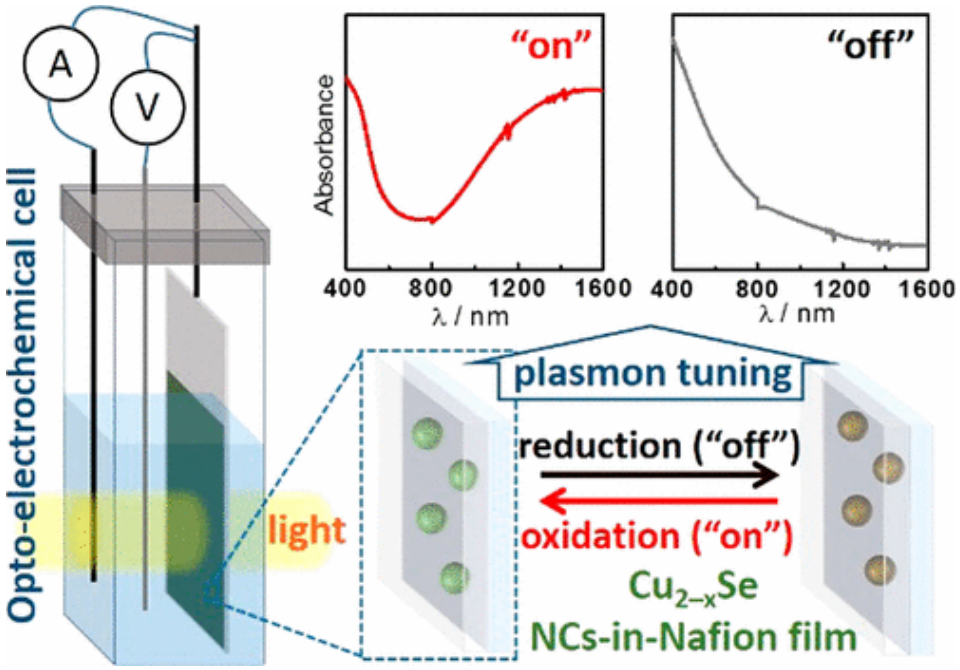

Figure 1.7 Scheme of an opto-electrochemical cell and the mechanism of tuning plasmon in $Cu_{2-x}Se$ NCs-in-Nafion films and the corresponding optical absorption spectra.[41]

1.2 Plasmonic Semiconductor NCs

Crystalline solid-state materials possess particular energy band structures (shown in Figure 1.8). Various band structures determine different electronic characteristics and further make an effect on the optical properties of solid-state materials. The band gap is defined as the energy difference between the conduction band (CB), which is normally unoccupied, and the

valence band (VB) with occupied energy states. Figure 1.8 depicts that there is a large band gap within an insulator indicating extremely high energy needed to promote electrons from VB to CB. A metal, however, has a large overlap between VB and CB, resulting in no energy band gaps. Thus, electrons in metals can move freely across the bands.[42] In the case of intrinsic semiconductor materials, the band gap energy is smaller than that of insulators. And the free electrons donated by shallow donor states can easily jump into CB with photon excitation, after which the semiconductors will have similar behaviour to metals. This small band gap structure of semiconductors renders scientists' tremendous interests.

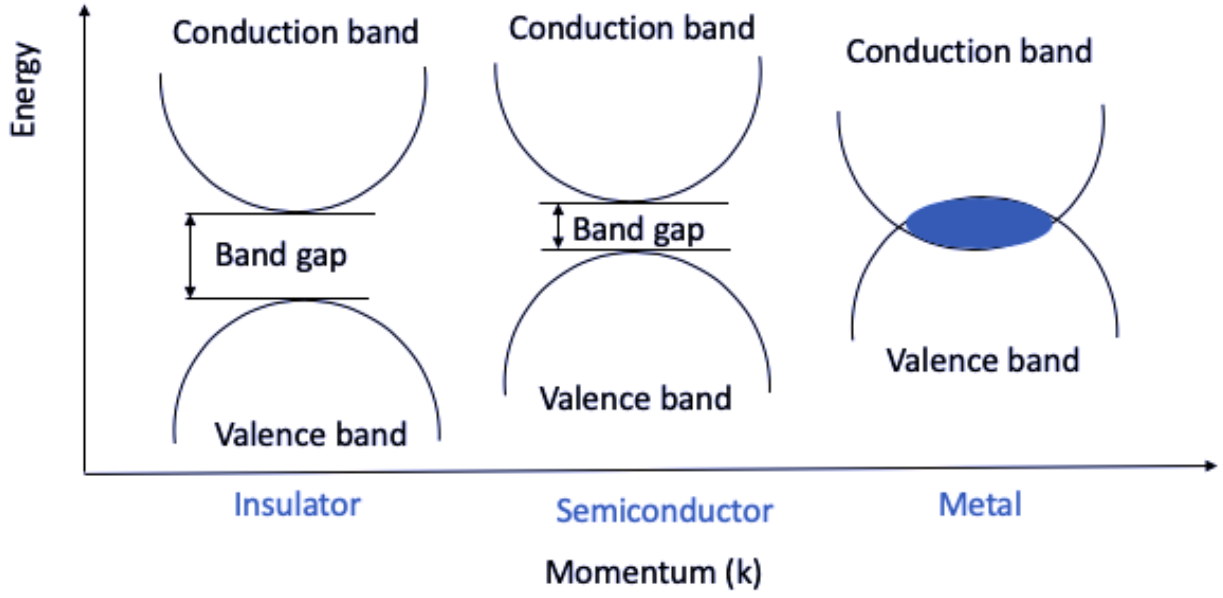

Figure 1.8 Illustration of band structures of insulators with a large band gap (left), semiconductors with a relatively small band gap (middle), and metals without a band gap (right).

1.2.1 Doping Mechanism of Semiconductor NCs

Semiconductors can be classified into two types according to their doping source: intrinsic and extrinsic semiconductors. An intrinsic semiconductor is an undoped or pure semiconductor with charge carriers generated without intentional incorporation of impurities.[43] In intrinsic semiconductors, charge carriers arise are mainly from electron excitation or crystallographic defects.[43] On the contrary, extrinsic semiconductors are formed by incorporating impurities (dopant atoms) into pure semiconductors. These impurities can be either donors or acceptors. An extrinsic semiconductor containing electron donor levels is named an n-type semiconductor because the majority of charge carriers are negative (electrons). Analogously, a p-type semiconductor is defined when a pure semiconductor contains positive holes.[44] The band gap structures of p-type and n-type semiconductors are demonstrated in Figure 1.9.

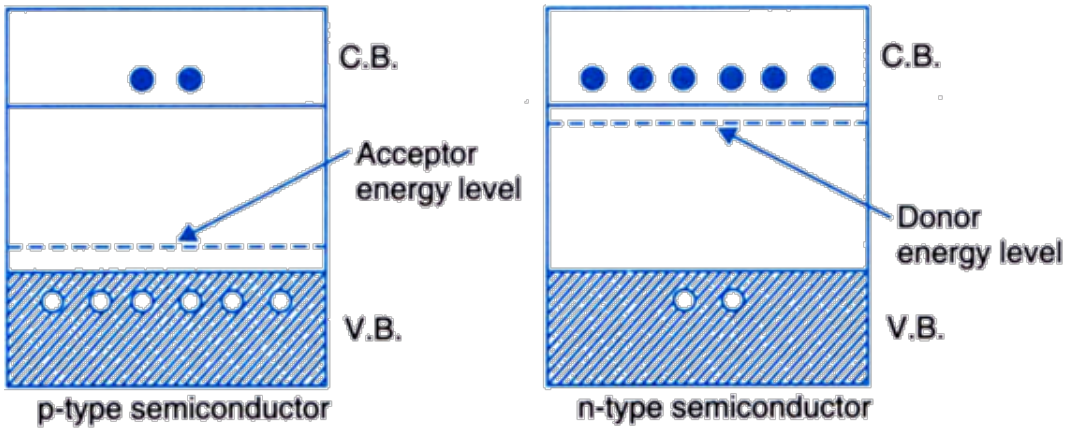

Figure 1.9 Schematic of p-type semiconductors with acceptor energy level close to the valence band (left figure) and n-type semiconductors with donor energy level close to the conduction band (right figure).

There are three major mechanisms of chemical doping of semiconductors, as shown in Figure 1.10: vacancy doping, aliovalent substitutional or interstitial doping, and compensation doping.[45–47] In a vacancy doping system, vacancies can produce either free positive holes or free negative electrons as free charge carriers by controlling the stoichiometry without doping extrinsic ions. An example is Cu vacancies in $Cu_{2-x}S$.[48] Aliovalent doping refers to the host lattice incorporating foreign ions having different valence from the host ions at interstitial or substitutional lattice sites.[49] These impurities can donate a free electron or free hole to the CB or VB, respectively. Synthetically, aliovalent interstitial or substitutional doping can be realized by balancing reactivity between dopants and host precursors during NC growth.[50] Compensation doping, as the name suggests, implies the interplay between extrinsic dopants and intrinsic defects. A representative example is tin-doped indium oxide ($Sn:In_2O_3$) studied by Agoston *et al.* in 2009.[47] They elucidated that the source of free charge carriers comes from substitutional Sn^{4+} atoms (extrinsic), oxygen vacancies (intrinsic), and $2Sn^{\cdot}_{In} - O_i''$ defect complex (compensation).

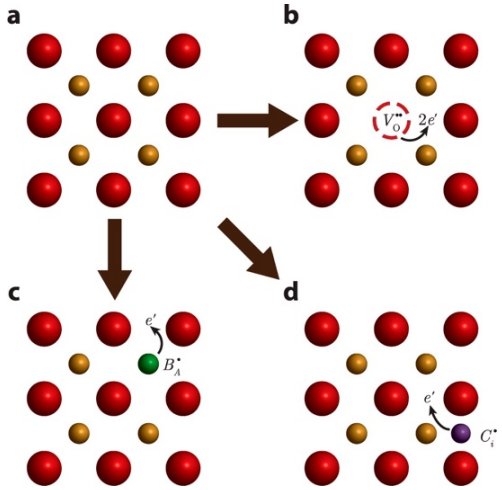

Figure 1.10 Schemes of common doping types with host metal cations (orange spheres) and oxygen anions (red spheres); (b) vacancy doping; (c) aliovalent substitutional doping with external atoms (green spheres); (d) aliovalent interstitial doping with external atoms (purple spheres).[22]

1.2.2 Metal Oxide Semiconductor NCs

Plasmonic metal oxide semiconductors are of major interest in this work. Most of these metal oxides are intrinsic n-type semiconductors, such as In_2O_3,[51] CdO,[52] and ZnO.[53] In such metal oxides, the intrinsic doping occurs since the oxygen vacancy concentration can be modulated through trapping a nonequilibrium concentration or tuning oxygen partial pressure, breaking the original equilibrium oxygen vacancy concentration.[1] Additionally, aliovalent doping has been a subject of intense study in recent years, especially for the following semiconductor materials: Sn:In_2O_3,[20] In:CdO,[24] and Al:ZnO.[54] In these systems, the host lattice ions are substituted by dopant ions having lower or higher valence to achieve n-type doping of

the material. These doping sites can contribute to free charge carrier density and make significant effects on the optical properties of plasmonic semiconductor NCs.

In the intrinsic system, the origin of free charge carriers in the CB is mostly from the intrinsic oxygen vacancies. Several researchers have successfully tuned the oxygen vacancy concentration by controlling the effective oxygen partial pressure in the process of NC synthesis.[55–57] As each oxygen vacancy is compensated by two free electrons to keep charge neutrality, by this means, the carrier concertation generated by defects can reach the order of 10^{19} cm^{-3}, executing the LSPR in undoped metal oxide semiconductor NCs. On the other hand, in the extrinsic regime, free carriers can be generated by cation vacancies or interstitial oxygen forming different defect complexes in host lattices in which the Fermi level is raised or lowered by aliovalent dopants substituting lattice atoms. Several studies have been conducted to investigate activated dopant ions and the impact of defect complex concentration on LSPR properties.[19,27,47] In this thesis, I will focus on both intrinsic doping (SnO_2, ZnO NCs) and aliovalent substitutional doping ($Sb:SnO_2$) regimes.

1.2.3 Metal Chalcogenide Semiconductor NCs

Plasmonic metal chalcogenide compounds such as $Cu_{2-x}E$ [58,59] and HgE [60,61] (E = S, Se, Te) are p-type semiconductor NCs having the LSPR behaviour. Extraordinarily, the research study in plasmonic copper chalcogenide NCs has been a focus over the past few decade. The LSPR in $Cu_{2-x}E$ (E = S, Se, Te) NCs is traceable to the collective oscillation of free holes in the VB and its frequency can be controlled by intrinsic doping through crafting

the stoichiometry of NCs. Generally, it is measured that the concentration of free charge carriers (holes) of as-synthesized $Cu_{2-x}E$ (E = S, Se, Te) NCs is on the order of 10^{21} cm^{-3} bringing about the LSPR in the NIR region.[62] Cu_2S is intrinsically unstable and easy to degrade into copper-deficient $Cu_{2-x}S$ phases under an oxygen atmosphere. Zhao *et al.* successfully synthesized various non-stoichiometric djurleite ($Cu_{1.97}S$), digenite ($Cu_{1.8}S$) and covellite (CuS) NCs through tuning the reduction potential by changing the pH or using different precursor treatments.[63] They were the first to attribute the origin of infrared absorption in $Cu_{2-x}S$ NCs to free carrier collective oscillation or LSPR, and they concluded that the plasmonic absorption shifts to higher energy with increasing cation vacancy concentration (Figure 1.11), implying that the LSPR is dependent on free carrier concentration, in this case, the copper vacancy. Additionally, they found that the phase of $Cu_{1.97}S$ NCs has the most stable characteristic under air conditions. Dorfs *et al.* achieved tuning plasmonic absorption in non-stoichiometric $Cu_{2-x}Se$ NCs from ca. 0.5 eV to ca. 1.0 eV by adding oxidant Ce(IV) complex or reductant Cu(I) complex (Figure 1.5).[35] Kriegel *et al.* extended the understanding of LSPR in vacancy-doped copper chalcogenide NCs to the entire family of $Cu_{2-x}E$ (E = S, Se, Te) NCs.[64] They conducted a straightforward strategy to synthesize $Cu_{2-x}Te$ NCs with well-defined morphology, and all of these prepared $Cu_{2-x}Te$ NCs exhibit pronounced LSPR absorption in the NIR region (Figure 1.12). Furthermore, they found that the standard Drude model is not appropriate for various-shaped $Cu_{2-x}Te$ NCs since the damping could not be neglected for nanorods or tetrapods.

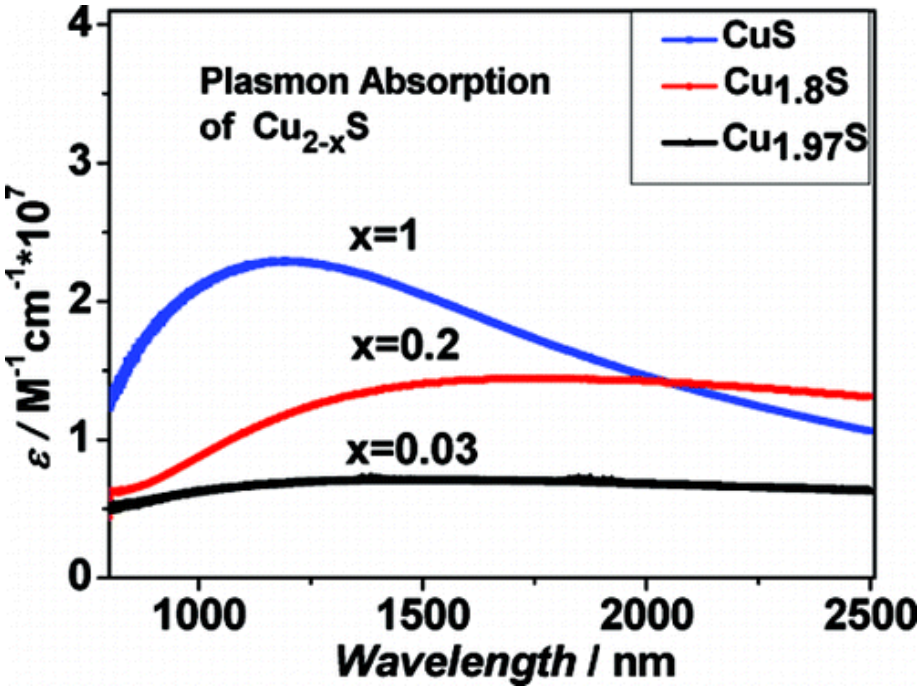

Figure 1.11 Plasmon absorption spectra of $Cu_{2-x}S$ NCs. Blue trace: covellite CuS (x = 1), red trace: digenite $Cu_{1.8}S$ (x = 0.2), and black trace: djurleite $Cu_{1.97}S$ (x = 0.03).[63]

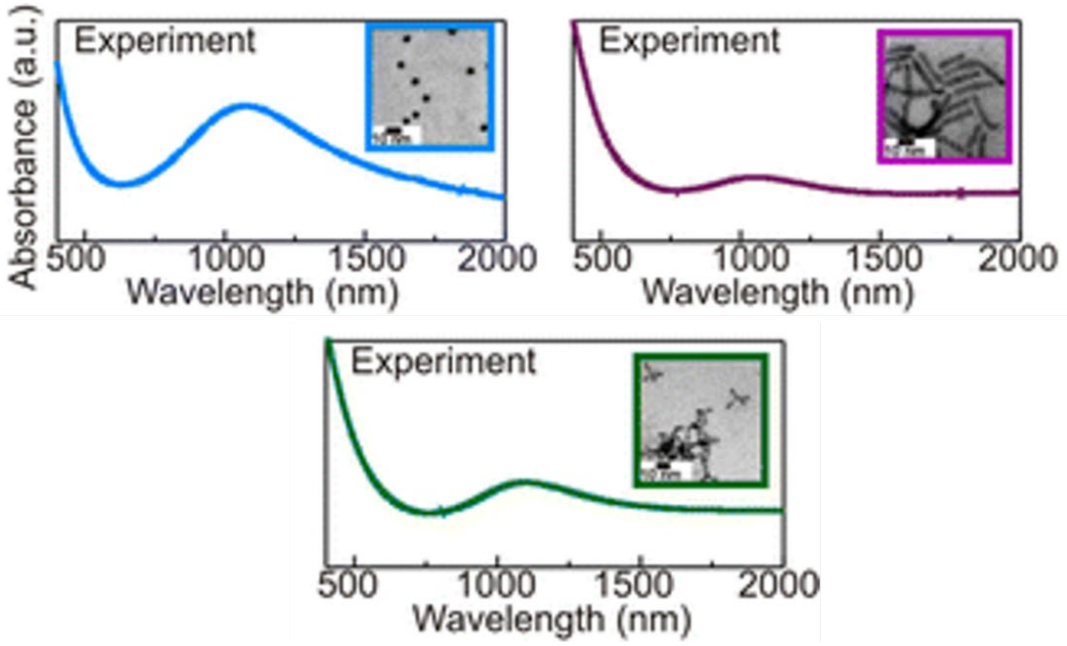

Figure 1.12 Absorption spectra of $Cu_{2-x}Te$ NCs of different shapes: $Cu_{2-x}Te$ spheres (blue curve, λ_{max} = 1074 nm), nanorods (purple curve, λ_{max} = 1069 nm), and tetrapods (green curve, λ_{max} = 1103 nm).[64]

1.3 Interactions between Plasmon and Quasiparticles

In the research study of plasmonic materials, one of the most fundamental problems is the electronic interaction in the quantum regime. Plasmons can interact with other quasiparticles due to the energetic proximity, which provides opportunities for novel discoveries and advanced technologies. Therefore, it is necessary to thoroughly understand the mechanism of interactions between plasmon and other quasiparticles such as phonons and excitons.

1.3.1 Exciton-Phonon Coupling

An exciton is a quasiparticle referring to a bound state of an electron attracted to a hole through the electrostatic Coulomb force. Phonons which are intrinsic property of any solid with any form participate in most excitonic reactions. In the formation of an exciton, phonons play an important role to conserve energy and momentum. Phonons can be classified into two different types, optical phonons having higher energy and acoustic phonons having lower energy. Additionally, the frequency of acoustic phonons increases with phonon wavevectors raising, while that of optical phonons is independent of phonon wavevectors.[65] The exciton-phonon coupling has received wide attention during the past few decades. Perebeinos *et al.*

found a strong effect of exciton-phonon coupling in carbon nanotubes.[66] They theoretically investigated the character of electron-phonon coupling and found strong phonon effects in excitonic spectra. Krauss *et al.* used resonant Raman spectroscopy to examine the strength of the exciton-phonon coupling in PbS NCs and figured out that the strength of the coupling is four orders of magnitude larger than the value calculated from the intrinsic electronic and vibrational wavefunction, while is similar to the value measured in Cd(S, Se) NCs.[67] Moreover, their results also support that the large exciton-phonon coupling is in accord with charge carriers localized at the surface of the NCs.

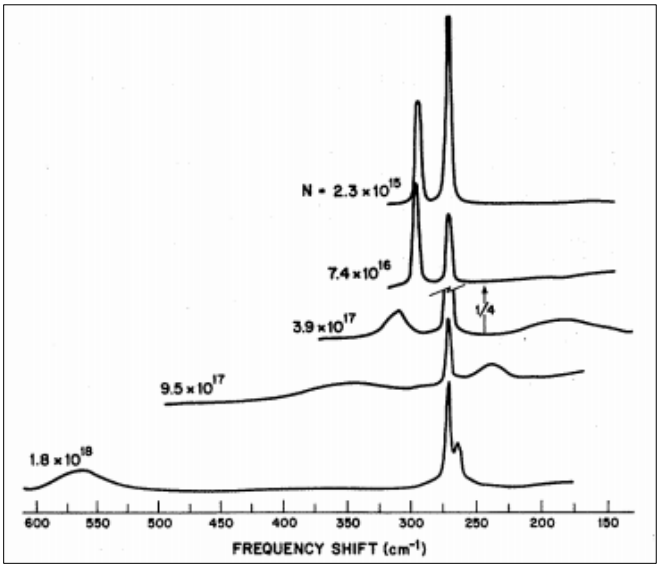

Figure 1.13 Anti-Stokes Raman spectra of n-type GaAs semiconductors. As shown in the figure, the frequency shift scale is not linear. [68]

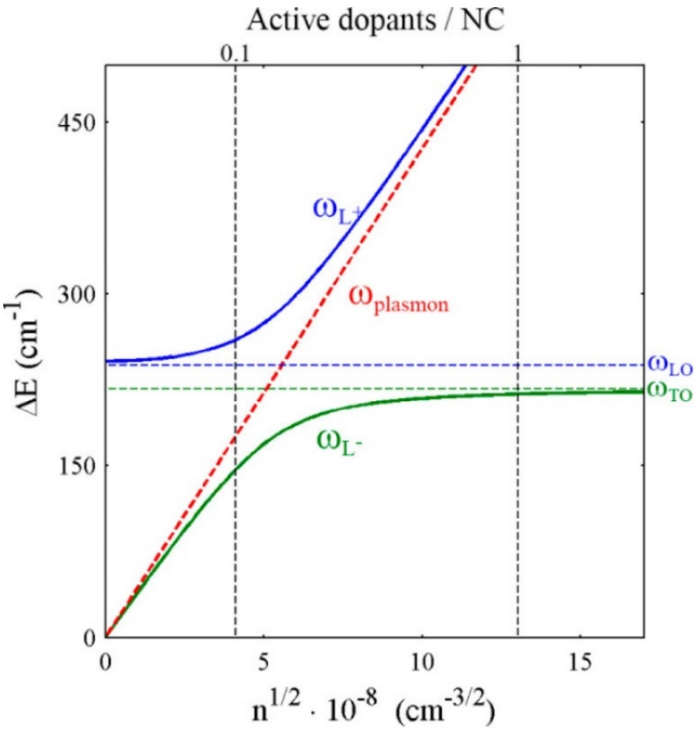

Figure 1.14 Calculated Raman shift of the coupled phonon-plasmon L^+ (blue curve) and L^- (green curve) modes versus the square root of the free electron concentrations in InAs. The longitudinal optical (LO) and transverse optical (TO) scattering energies are displayed by blue and green dashes lines, respectively. The plasmon energy is displayed by the dashed red line. The two vertical dashed black lines from left to right represent the carrier concentrations equivalent to 0.1 and 1 electrons per NC. [69]

1.3.2 Plasmon-Phonon Coupling

The study of the plasmon-phonon coupling could be traced back to the 1960s in which research in III-V semiconductors attracted robust interests.[68,70] At that moment, Mooradian *et al.* first observed the interaction between conduction-electron plasmons and the longitudinal optical (LO) phonon in GaAs semiconductors *via* the Raman spectrum.[68] They detected that as the plasmon frequency approaching the phonon frequency, the LO phonon line in the Raman

spectrum broadens and shifts to higher energy. Meanwhile, there is a second small band with a lower frequency appearing and reaching the transverse optical (TO) phonon frequency at higher carrier concentration (Figure 1.13). These experimental results verified the theoretical predictions of plasmon-phonon behavior.

With further investigation of polarization properties from the plasmon-phonon modes in n-type GaAs semiconductors, they proposed that the TO mode at a certain frequency is not affected by the free carriers.[70] However, these free carriers (plasmons) lead to the formation of upper longitudinal branch L^+ and lower branch L^- in the LO mode.[70] In recent years, Faust *et al.* presented the Raman scattering study in Cu-doped InAs NCs and obtained similar results.[69] As shown in Figure 1.14, the frequency of L^+ and L^- branches are related to the free charge carrier concentration at high doping levels. At high free carrier concentration, the L^+ mode converges closely to the plasmon mode which has a linear relationship with the square root of the free electron concentration, while the L^- mode asymptotically tends to TO mode. These results confirm that the plasmons could couple with LO phonons in semiconductors, which would be promising for the future development of electronic devices.

1.3.3 Plasmon-Exciton Coupling

According to the previous study, the coupling between a plasmon and an exciton exists in plasmonic semiconductor NCs.[71] The plasmon-exciton coupling could be able to not only contribute to the excitonic absorption and emission but also enhance the optical Stark effect.[20,72] For example, Okamoto *et al.* noticed the strong enhancement in PL emission spectra

induced by the exciton-surface-plasmon coupling when InGaN/GaN quantum well materials coat with Ag thin films (Figure 1.15).[73,74] Additionally, the plasmon-exciton coupling was also observed in a metal-semiconductor heterostructure consisting of Au NPs with localized plasmons and CdTe nanowires (NWs) with mobile excitons, and it confirmed that the NW emission becomes stronger and blue-shifted by changing the distance between these two nanocomposites.[75] Similar resonant coupling was detected in Au-CdSe heterostructure as well, where the spin manipulation is tailored as well as the optical Stark effect is enhanced *via* controlling the plasmon resonance.[76]

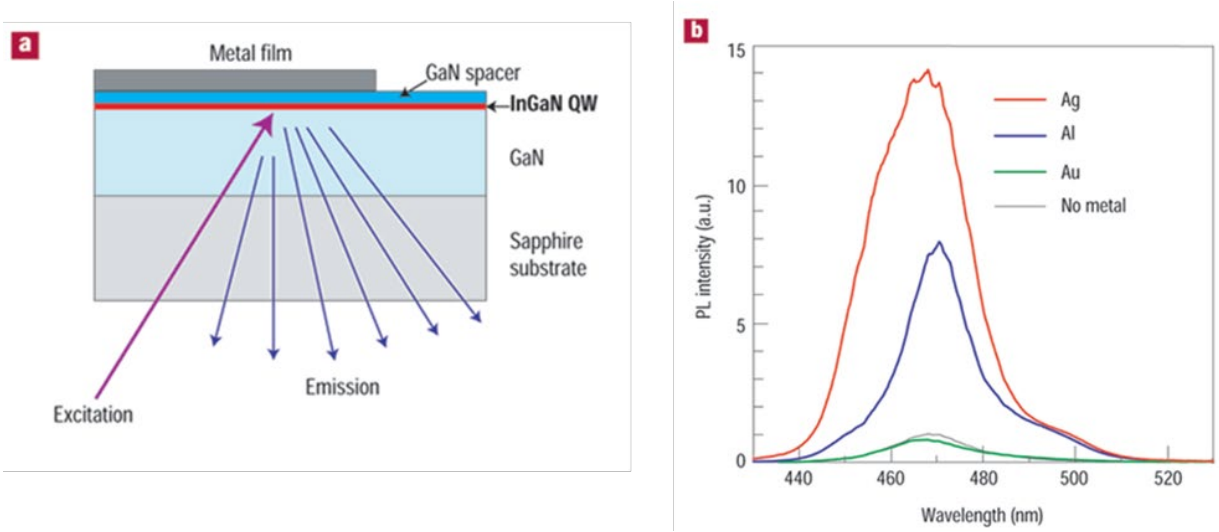

Figure 1.15 a. Sample structure and excitation/emission configuration of PL measurement. b. PL spectra of InGaN/GaN QWs coated with Ag (red curve), Al (blue curve), Au (green curve), and no metal (grey curve).[73]

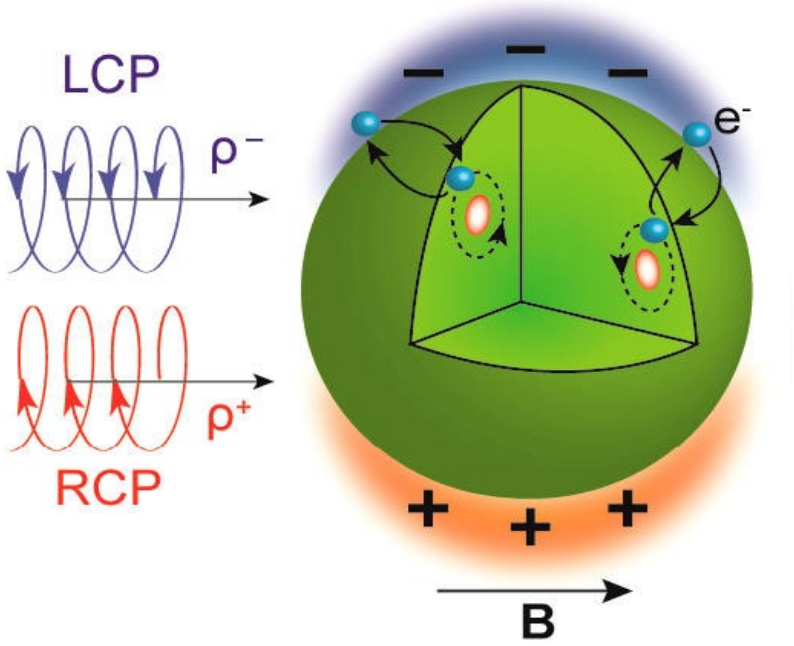

Figure 1.16 Schematic of the degenerate cyclotron plasmonic modes excited by left circularly polarized (LCP) and right circularly polarized (RCP) light with an external magnetic field.[71]

However, a challenge of the plasmon-exciton coupling in single-phase semiconductor NCs arises from the absence of resonance between confined plasmon oscillations and excitonic transitions.[20] Plasmonic metal oxide semiconductor NCs provide a chance to understand the mechanism of interface-free plasmon-exciton coupling. Yin *et al.* designed a creative experiment, for which they generated a degenerately doped In_2O_3 cyclotron magneto-plasmonic mode (Figure 1.16), and then measured the magneto-optical properties by magnetic circular dichroism (MCD) spectroscopy.[20] They hypothesized that the optical phonons, quasiparticles describing vibrational degrees of freedom in lattices, play a critical role in plasmon-exciton coupling because they can couple with both plasmons and excitons in

semiconductor NCs.[66–70] Besides, it has been observed and proven that phonons can transfer angular momentum providing for magneto-plasmonic modes generation and band state splitting, and thus phonons could be considered as the media for plasmon-exciton coupling.[77]

1.4 Magnetic Semiconductor NCs

Magnetic semiconductors perform both ferromagnetic and semiconducting properties, which would provide a new way to control the conduction when they are implemented in devices. Moreover, magnetic semiconductors would also regulate the quantum spin state (up and down), which is considered to be a vital property for spintronics applications.[78]

1.4.1 Diluted Magnetic Semiconductors

Although some traditional magnetic materials such as magnetite also exhibit semiconductor characteristics, it is anticipated that magnetic semiconductors will be extensively adopted only if they are similar to those well-developed semiconductors. To that end, dilute magnetic semiconductor (DMS) has become a novel candidate material in magnetic material study and microelectronics industry application due to its unique spin-dependent magneto-electro-optical properties, which has aroused tremendous interest. DMS is a class of magnetic materials which is created when a non-magnetic semiconductor is non-degenerately doped with magnetic metal atoms, typically transition-metal impurities. The field of dilute magnetic semiconductors (DMSs) emerged in the 1970s then developed with the investigation of II-VI semiconductors (CdSe and HgTe).[79] People realized that introducing a small number

of magnetic dopants would not deteriorate the electronic and optical properties of host materials, whilst would induce a strong magnetic field effect. It can be ascribed to the exchange interaction between s or p-electrons in the host and d-electrons in the dopants.[79] These interactions can be achieved and manipulated at the single nanostructure level,[80,81] which has created a significant interest in designing DMS nanomaterials.[82] The biggest challenge of DMSs is the Curie temperature (T_C) which is below room temperature leading to the loss of magnetic properties. Generally, temperature is a key factor for the ordering amongst magnetic moments since if the thermal energy is larger than the ordering energy, the material will lose its magnetism. Therefore, seeking DMS materials with a high T_C above room temperature is crucial. Recently, some metal oxide with wide band gaps such as SnO_2, ZnO, In_2O_3, and TiO_2 have been widely used as host materials for the research study of diluted magnetic semiconductor oxides (DMSOs).[83–86] Among these materials, the magnetic properties and the T_C are directly controllable by the doping level. Coey *et al.* demonstrated that high T_C could be achieved by an extended hybridized state which is caused due to the interaction between the electronic states of the localized 3d impurity band and delocalized donor states when increasing the donor concentration over the critical one, leading to the impurity band states delocalizing and spin splitting.[84] In this thesis, I will focus on SnO_2 and ZnO NCs in which the defect-correlated band splitting occurs without magnetic dopants, which is analogous to DMS characteristics.

1.4.2 Introduction of Magnetic Circular Dichroism

Orbital polarization can be produced by an external magnetic field in addition to the intrinsic spin angular momentum. In the case of cyclotron LSPR modes exposure to an external electric and magnetic field which is parallel to the light propagation direction, the two LSPR modes are non-degenerate arising from the Lorentz and electric field forces acting on electrons. The total force $\boldsymbol{F}$ is expressed as:

$$\boldsymbol{F} = -e\boldsymbol{E} - e(\boldsymbol{v} \times \boldsymbol{B}) \qquad (1.7)$$

where e and $\boldsymbol{v}$ are the charge and velocity of electrons, respectively; $\boldsymbol{E}$ and $\boldsymbol{B}$ refer to external electric and magnetic fields, respectively.

Magnetic circular dichroism (MCD) provides new opportunities to explore the structure and magneto-optical properties of semiconductor NCs. MCD spectroscopy can detect the differential absorption of left (ρ^-) and right (ρ^+) circularly polarized (LCP and RCP) light of a sample, where the magnetic field is oriented parallel to the direction of light propagation (Figure 1.17).[20] Without an external magnetic field, LCP and RCP terms are degenerate at zero field thus indistinguishable. However, under the influence of an external magnetic field, two modes are split as they are experiencing an opposite Lorentz force, resulting in a derivative-shaped MCD spectrum and a shift of frequency ($\Delta\omega$) which is given as:

$$\Delta\omega = |\omega_B - \omega_0| = g(\omega_0)B \qquad (1.8)$$

where ω_B is the frequency of the separated magneto-plasmonic mode (ω_B^-, ω_B^+), ω_0 is the zero-field LSPR frequency, B is the given magnetic field strength, and $g(\omega_0)$ is the proportionality constant. In the light of Equation (1.8), it straightforwardly reveals that the MCD signal of LSPR is only related to the magnetic field and shows a linear relationship, while irrelevant to temperature.

Additionally, MCD measurement could also detect the splitting in DMSs. In such materials, the interaction between d-electrons from magnetic impurities and s- and p-electrons from host lattices would lead to the splitting of VB and CB hinging on spin orientation. Therefore, this spin-polarized semiconductor band structure would change the absorption between LCP and RCP beams, and the absorption difference could be collected by MCD spectra.[87]

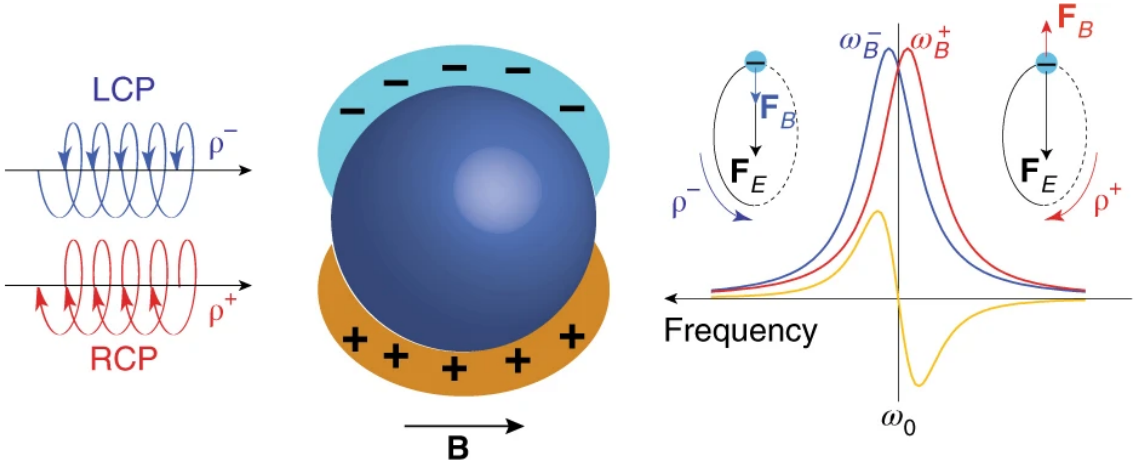

Figure 1.17 Schematic representation of the origin of the MCD signal of LSPR in plasmonic NCs (yellow curve), represented as the difference between the absorption of the LCP (ρ^-) beam (blue curve) and RCP (ρ^+) beam (red curve) for a magnetic field.[20]

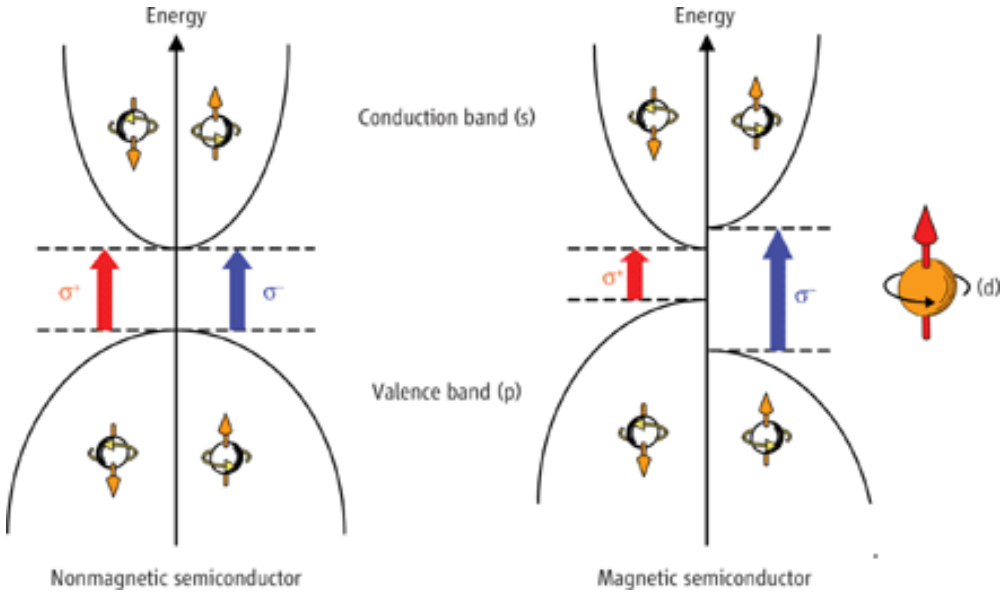

Figure 1.18 Schematic representation of the origin of the MCD signal in magnetic semiconductors. Left figure: for nonmagnetic semiconductors, electronic energy is independent on the direction of electron spin. Right figure: for magnetic semiconductors, the splitting of conduction band and valence band is related to the direction of electron spin.[87]

MCD signal emanates from Zeeman splitting for which a transition from the ground state to an excited state. MCD intensity is usually expressed as a sum of three Faraday terms, i.e. A, B and C terms. And the fundamental equation is described as Equation (1.9):[88]

$$\frac{\Delta A}{E} = \gamma \mu_B B \left[A_1 \left(-\frac{\partial f(E)}{\partial E} \right) + \left(B_0 + \frac{C_0}{k_B T} \right) f(E) \right] \qquad (1.9)$$

where A_1, B_0, and C_0 are constants referring to A, B and C terms of MCD, respectively; ΔA is the differential absorption between LCP and RCP light; γ is a constant which is related to the

units chosen; μ_B is the Bohr magneton; B is the magnetic field; E is the energy and $f(E)$ refers to the line-shape function; k_B is the Boltzmann constant; and T is the temperature.

A term, a temperature-independent MCD signal term with a derivative line shape, indicates the degeneracy of excited states. As shown in Figure 1.19a, the originally degenerate $J_{-1,+1}$ state is split into two sublevels of J_{+1} and J_{-1} when exerting a magnetic field along the direction of light. The absorption of LCP and RCP light occurs in the transition of $A_0 \rightarrow J_{+1}$ and $A_0 \rightarrow J_{-1}$, respectively, giving rise to the energy difference of the transition, namely, the Zeeman splitting.[88] B term is also a temperature-independent factor, which originates from the mixing effect of zero-field functions between non-degenerate states in a magnetic field but exhibits a "absorption-like" signal (Figure 1.19b).[88] Generally, the analysis of B term is simplified to evaluate only a few mixing states close in energy. Compared with A or C terms, B term is much weaker and hard to distinguish in an MCD spectrum, even though it contributes to almost every molecule's MCD signal. Different from A and B terms, C term has a temperature-dependent nature with a Gaussian line shape as a result of the ground-state degeneracy in the presence of an external magnetic field (Figure 1.19c).[88] The intensity of C term is especially sensitive to temperature owing to the strong dependency of the population of filed-split ground states on temperature. In a diamagnetic system, C term equals zero as the molecules are of non-degenerate ground states. Whereas, for paramagnetic molecules, C term becomes dominant in MCD spectra especially at low temperature, in accordance with the Curie-type relationship the signal has the following temperature dependence, Equation (1.10):

$$M = \frac{N}{T} \qquad (1.10)$$

where M is the resulting magnetization, N is the fitting parameter, and T is the temperature. This equation will be adapted to the future fitting of MCD spectra in this thesis.

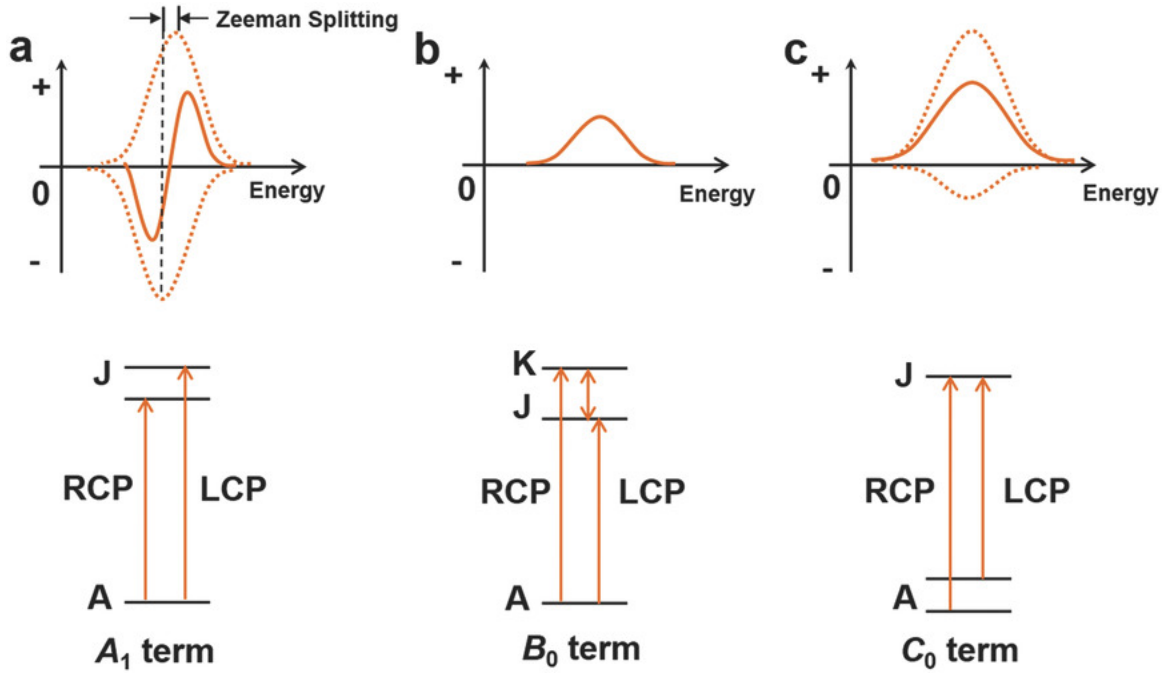

Figure 1.19 The simplified diagram of the mechanism of a) A; b) B; and c) C terms in MCD. The dashed curves represent absorption of LCP light (positive peaks along the vertical axis) and RCP light (negative peaks along the vertical axis). The solid curves in the top graphs stand for the resultant MCD responses.[88]

1.5 Two Major Metal Oxide Semiconductor NCs

1.5.1 Tin(IV) Oxide (SnO_2) NCs

Tin (IV) oxide (SnO_2) with mineral form in nature called cassiterite has engaged immense interest in scientific research and industrial application. SnO_2 which has a rutile crystal structure is an n-type oxygen-deficient semiconductor having a band gap energy of 3.6 eV.[89] Figure 1.20 depicts that the SnO_2 lattice is of a tetragonal unit cell in the space group of $P4_2/mnm$ with lattice parameters of a = b = 4.70 3Å and c = 3.173 Å.[90]

The presence of oxygen vacancies (V_O) in SnO_2 semiconductors induces electrons conduction, and the Kröger-Vink notation is shown as follows:

$$O_O^X \rightarrow V_O^{\cdot\cdot} + 2e' + \frac{1}{2} O_2(g) \qquad (1.11)$$

In light of this equation, one doubly ionized vacancy site and two free electrons are generated by one oxygen vacancy, providing a source for charge carriers.[90] The other potential source of free electrons comes from tin interstitials, Sn_i. [91] Kilic and Zunger [91] indicated that interstitial tin played a dominant role in conductivity. Sn_i forms a donor level within the conduction band because of its loosely bound outer free electrons, resulting in prompt donor conductivity.[91] Moreover, Sn_i exists abundantly owing to its low formation energy, and it is able to reduce the formation energy of V_O as well.

Tin oxide (SnO_2) can be regarded as a transparent conducting oxide (TCO) due to its high band gap energy as well as mechanical and chemical stability.[92] As a consequence, SnO_2

is a promising material for wide applications in sensors, solar cells, and lithium-ion batteries. Additionally, there are several synthesis approaches to make pure or doped SnO_2, such as solvothermal, polymerized complexes, sol-gel, co-precipitation etc.

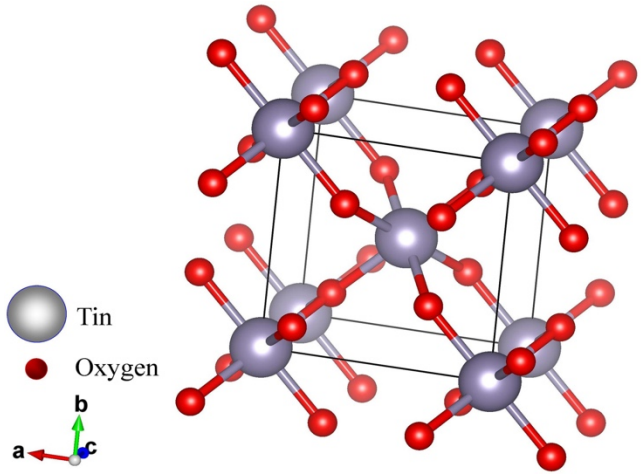

Figure 1.20 Schematic of the tin(IV) oxide with rutile crystal structure. Grey spheres represent tin atoms and red spheres represent oxygen atoms.[90]

1.5.2 Zinc Oxide (ZnO) NCs

Zinc oxide (ZnO) has always been a research subject of great concern in the past few decades due to its non-toxic, cost-effective, and environment-benign merits. ZnO has three different crystalline forms: cubic rocksalt, cubic zincblende, and hexagonal wurtzite, as shown in Figure 1.21. Particularly, the wurtzite phase is of major attraction because of its better thermodynamical standability at ambient pressure and temperature. For the wurtzite structure, the lattice spacing of a and c are 0.325 and 0.521 nm, respectively.[93] The calculated ratio of

c/a is around 1.603 that is very close to the ideal value for unit hexagonal cell in the ratio of c/a = 1.633.[93] In this hexagonal structure, as shown in Figure 1.21c, tetrahedral zinc and oxygen atoms are stacked alternately along the c-axis and each zinc atom is surrounded by four oxygen atoms, and vice versa.[94] Zinc-blende form is metastable and can be stabilized by growth on cubic substrates.[93] The rocksalt crystal structure has been rarely discussed since it may only exist at relatively high pressure.[94]

ZnO is a common semiconductor with n-type electrical conductivity, a wide direct band gap of ca. 3.37 eV and a large exciton binding energy of ca. 60 meV at room temperature.[95] Additionally, ZnO exhibits strong optical absorption in both UVA (315-400 nm) and UVB (280-315 nm), giving a new way of improving antibacterial response.[93] These unique features in optical, electrical, semiconducting and chemical sensing aspects capacitate ZnO having significant applications in diverse areas, such as photocatalyst, transistors, optoelectronic devices, and chemical sensors.[93,96,97]

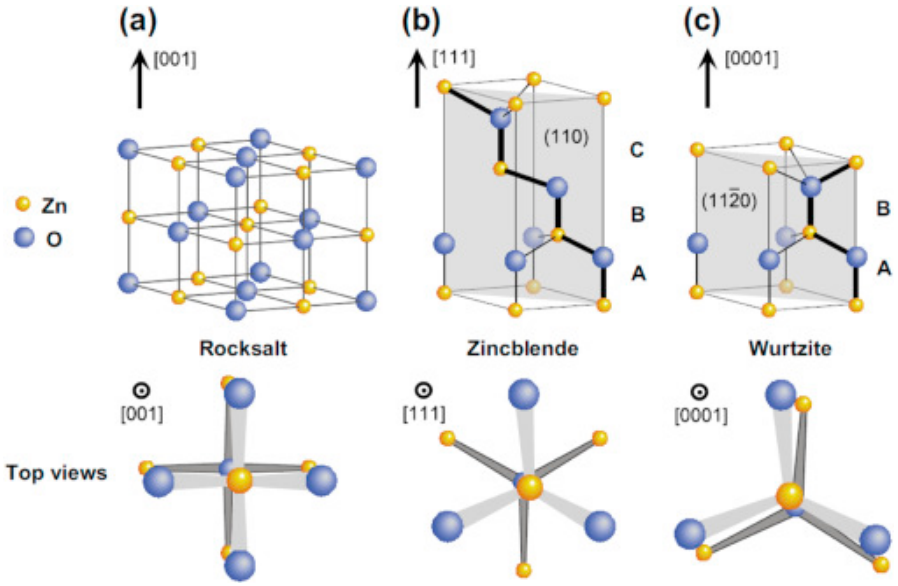

Figure 1.21 Stick and ball representation of ZnO crystal structures: (a) rocksalt (cubic); (b) zinc blende (cubic); and (c) wurtzite (hexagonal). Yellow spheres represent zinc atoms and blue spheres represent oxygen atoms.[94]

ZnO-based DMSOs have been one of the most attractive research subjects for application in spintronics.[98] After substantive theoretical and experimental investigations, native point defects are considered as the cause of ferromagnetism at room temperature.[99] Nevertheless, the origin of d_0 ferromagnetism in ZnO semiconductors is still under debate. There are four major defect forms present in ZnO materials: oxygen vacancies (V_O), oxygen interstitials (O_i), zinc vacancies (V_{Zn}), and zinc interstitials (Zn_i).[98] Normally, V_O serves as donors, whilst V_{Zn} acts as acceptors. For instance, Liu *et al.* demonstrated three different sources of defect-related visible emission in ZnO NPs: electrons trapped in (a) single ionized oxygen vacancies (V_O^+); (b) doubly ionized oxygen vacancies (V_O^{++}); and (c) intrinsic oxygen interstitials (O_i) behaving as traps for photo-generated holes.[100] Moreover, Das *et al.* proposed

that the visible emission derived from electronic transitions between defect levels within band gaps of ZnO NPs.[101] They reported two types of these electronic transitions (as shown in Figure 1.22): (a) from neutral oxygen vacancies (V_O) to zinc vacancies (V_{Zn}) and (b) from singly charged oxygen vacancies ($V_O^{\cdot}$) to zinc vacancies (V_{Zn}).[101]

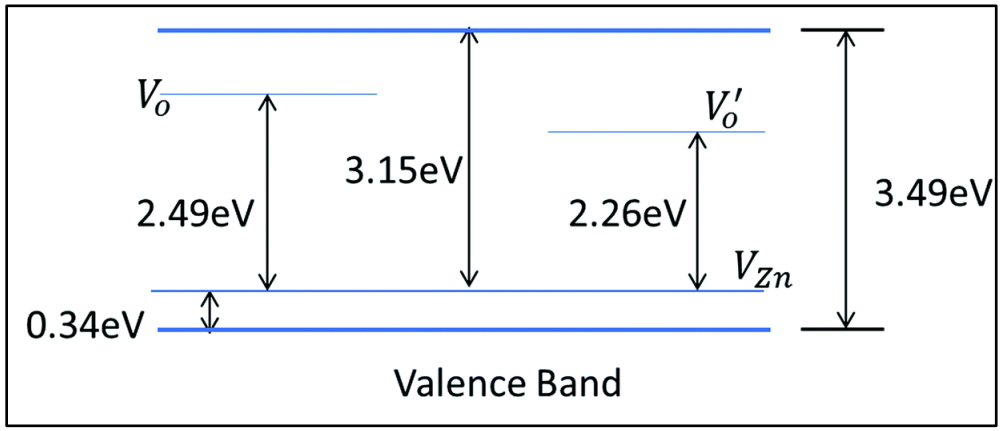

Figure 1.22 Diagram of band states including relevant defect levels. V_O and $V_O^{\cdot}$ are donor levels localized at 2.49 eV and 2.26 eV above V_{Zn}, respectively.[101]

1.6 Motivations and Scope of the Thesis

In order to contribute to potential breakthroughs in multifunctional quantum devices and optoelectronic devices, the vital motivation of this thesis is to manipulate plasmonic properties in n-type antimony-doped SnO_2 (ATO) NCs *via* multiple mechanisms and to investigate the effect of point defects on carrier polarization and band splitting in ZnO and SnO_2 NCs. Additionally, SnO_2 NCs synthesized under different conditions or having different compositions will contribute to our database of LSPR in metal oxide semiconductors and

further help to build up a universal model to demonstrate the plasmon-exciton coupling mechanism.

Considerable work on LSPR properties of noble metal nanoparticles has been done in the past few decades. Although Ag and Au's nanostructures have high free charge carrier concentration leading to a strong LSPR signal, the tunability of LSPRs in these metals is constrained, and noble metals are pricey. On the contrary, SnO_2 is a cost-effective and environmental-benign semiconductor, and its optical properties can be controlled over *via* an aliovalent doping approach. Moreover, degenerately doped SnO_2 semiconductors possess significant LSPRs, regarded as promising materials in optoelectronic applications. Antimony (Sb) is in group V of the periodic table of elements and was selected as a dopant in SnO_2 because it has a similar atom radius as the adjacent Sn. Besides, Sb itself has various oxidation states such as +3 and +5, providing an opportunity for aliovalently doping in SnO_2 semiconductors, where the valence of Sb is +5. However, few studies of LSPR properties in ATO NCs were done. Therefore, in the first part of this thesis, I attempted different methodologies to synthesis ATO NCs with various doping concentrations. Going forward, a series of techniques including UV-vis-NIR spectroscopy, MCD spectroscopy, and X-ray diffraction (XRD) measurements were employed to characterize optical and magneto-optical properties, as well as crystal structures in pure and/or doped SnO_2 semiconductor NCs. Moreover, post-synthesis processing such as thermal annealing was applied to this work to tune the LSPR absorption. And the plasmon intensity and the oxidation states of Sb are correlated by analyzing X-ray photoelectron spectroscopy (XPS).

ZnO is highlighted as a third-generation semiconductor owing to its wide band gap, high exciton bind energy at room temperature, and other merits including chemical stability,

rich-defect properties, and nontoxicity. One of the most renowned research on ZnO is native defect-induced ferromagnetism for potential applications in spintronics. Unlike diluted magnetic semiconductors (DMSs), the magnetic property in pure ZnO NCs reflects its independent relation with the presence of magnetic impurities. Hence, it is necessary to clarify this mechanism and elucidate how point defects influence the carrier polarization and band state splitting in the NCs. In the second part of this thesis, I leveraged photoluminescence (PL) spectroscopy to detect the point defects and combined with MCD spectra to study the defect-related charge carrier polarization and band splitting in ZnO NCs prepared under varying atmosphere. Subsequently, I treated the NC samples with thermal annealing in the air to further confirm the relationship between oxygen deficiencies and the excitonic splitting. More interestingly, I also observed this Zeeman splitting in SnO_2 NCs. These results imply the universality of carrier polarization and band splitting associated with native defects in metal oxide NCs, and it is worth exploring further.

Chapter 2
Experimental Section

2.1 Chemicals

All chemicals were purchased from the manufacturers and used without any future purification. Tin (IV) chloride pentahydrate ($SnCl_4 \cdot 5H_2O$, 98%) and antimony (III) chloride (99%-Sb) were purchased from STREM Chemicals.[89] Zinc stearate ($ZnSt_2$, 12.5-14 %) was purchased from Alfa Aesar. Oleylamine (OAm, 70%), oleic acid (OA, 90%), tri-n-octylphosphine oxide (TOPO, 90%), dodecylamine (DDA, 98%), 1-dodecanol (DDOL, 98%), 1-octadecene (ODE, 90%), ammonium hydroxide (NH_4OH, 28.0-30.0%), 1,4-dioxane (99%), acetone (HPLC grade), toluene (HPLC grade), hexane (HPLC grade), tetrachloroethylene (TCE, 99.5%), and ethanol (EtOH, HPLC grade) were all purchased from Sigma-Aldrich company.[89] The mixture gas of hydrogen and nitrogen (7 % H2 in N2) was purchased from Praxair.

2.2 Synthesis Procedure

2.2.1 Solvothermal Synthesis of SnO_2 and ATO NCs

Solvothermal SnO_2 and ATO NCs were synthesized using a modified form of a previously reported procedure.[89,102,103] In a typical synthesis of SnO_2 NCs, 1.0 g of $SnCl_4 \cdot 5H_2O$, 7 mL of EtOH, 20 mL of OA, and 4 mL of OAm were mixed into a 45 mL Teflon-lined stainless-steel autoclave (as shown in Figure 2.1), and then the autoclave was

placed into a preheated oven (185 °C). The reaction duration was 4 h, after which the autoclave was taken out and cooled down to room temperature naturally in the fume hood. The acquired xerogel was washed with acetone and centrifuged three times. Afterward, the washed NCs were treated with TOPO at 90 °C for 1 hour to remove dopant ions bounded on the surface.[104] The post-synthesized SnO_2 NCs were repeatedly washed with acetone and centrifuged three times. Finally, one portion of SnO_2 NCs was dispersed in hexane for optical measurements, and the left was dried out onto a watch glass at room temperature for crystalline structure analysis. To avoid $SbCl_3$ exposure to moisture leading to weighing inaccuracy, a stock solution of $SbCl_3$ was prepared in the glove box *via* dissolving 1.625 g of $SbCl_3$ solids to 50 mL of EtOH, for which 1 mL of the stock solution is corresponding to 5% Sb doping content. For the preparation of ATO NCs with variable doping concentration, a certain molar ratio portion ([Sb]/[Sn] = 0.05, 0.10, 0.15, and 0.20) of $SbCl_3$ stock solution was added into the reactants, and then the addition of EtOH was decreased to 6, 5, 4, and 3 mL, respectively. The reaction temperature, duration time, washing process, and post-synthesis treatment were consistent with the pure SnO_2 NCs preparation. For future study, small portions of solvothermal-made powdered SnO_2 and ATO NCs were annealed at 500 and 1000 °C from 1 min to 24 h in a muffle furnace. The reaction mechanism is shown as the Kröger-Vink notation (Equation 2.1):

$$2Sb_2O_5 \xrightarrow{SnO_2} 4Sb_{Sn}^{\cdot} + 10O_O^X + V_{Sn}^{4\prime} \qquad (2.1)$$

Figure 2.1 Pressure Vessel for solvothermal NCs synthesis, including stainless-steel shells and lids, teflon cups, and bursting discs.

2.2.2 Coprecipitation Synthesis of SnO_2 and ATO NCs

Coprecipitation synthesis of SnO_2 and Sb:SnO_2 (ATO) NCs was performed using a previously reported procedure.[105,106] Briefly, 0.7 g of $SnCl_4 \cdot 5H_2O$ and different amounts of $SbCl_3$ were added to 10 mL of deionized water, followed by stirring until precursors were fully dissolved. The reaction mixture was then placed into an ice bath to cool down for 15 min and then concentrated NH_4OH was slowly added to the mixture until the pH became 6. After allowing the content to settle down for 3 h, the obtained fine powder was washed multiple times with deionized water. Dilute NH_4OH was added to the washed precipitate. The clear

suspension was transferred to a three-neck round-bottom flask and refluxed at 90 °C for 15 h, after which it was cooled to room temperature. The resulting NCs were extracted with 1,4-dioxane, followed by centrifugation and washing with EtOH three times. The precipitated NCs were resuspended in excess DDA and heated at 120 °C for 30 min to give a clear suspension which was precipitated and triple washed with EtOH. The DDA-capped NCs were then resuspended in melted TOPO, heated at 90 °C for 1 h, and precipitated and washed with EtOH. This process allows for further removal of surface-bound dopant ions and NC capping with TOPO. Finally, a portion of NCs was dispersed in hexane for optical measurements, and the rest was dried out onto a watch glass at room temperature for crystal structure analysis. For further processing investigation, small portions of powder SnO_2 and ATO NCs were annealed at 500 °C and 1000 °C from 1 min to 24 h in a muffle furnace.

2.2.3 Colloidal Synthesis of ZnO NCs

The synthesis of zinc oxide NCs was conducted by an existing non-injection procedure.[107] In a typical reaction, 1.89 g of $ZnSt_2$ was added to a three-neck round bottom flask (RBF) mixed with 16.00 g of ODE, 2.65 g of OA, and 4.80 g of DDOL. Then the mixture was degassed under the hydrogen (or air) flow for 10 min. The reactants were first heated up to 100-140 ℃ for 30 min for dissolving evenly and then heated to 250 ℃ for 1 h under hydrogen (air) flux. Finally, the obtained solution was centrifuged after cooling down to room temperature, and the precipitate was washed with toluene and acetone three times. For future measurements, portions of NCs were suspended in hexane and toluene, and the rest was dried

on a watch glass naturally overnight. Small portions of powder ZnO NCs were annealed at 500 ℃ for 12 h in a muffle furnace.

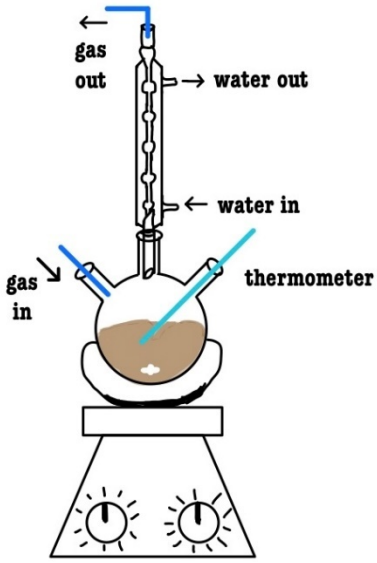

Figure 2.2 Colloidal setup for NC synthesis, including round bottom flask (RBF), condenser, thermometer, and hot and stir plate.

2.3 Characterization Techniques

2.3.1 Powder X-ray Diffraction (XRD)

Powder X-ray diffraction (XRD) is an effective measurement to identify the three-dimensional crystal structure of NPs. The size of NPs can be calculated based on the Scherrer equation:

$$L_{hkl} = \frac{K\lambda}{\beta \cos(\theta)} \qquad (2.2)$$

where L_{hkl} is the mean crystallite size of samples, λ is the X-ray wavelength, K is a dimensionless shape factor, β is the full width at half-maximum (FWHM), and θ is the Bragg angle.[108] The XRD patterns of all samples were collected with an INEL XRD diffractometer with a position-sensitive detector and monochromatic Cu-Kα radiation (λ = 1.5406 Å) in Dr. Holger Kleinke's group in the Department of Chemistry at the University of Waterloo.

2.3.2 Transmission Electron Microscopy (TEM)

Transmission electron microscopy (TEM) is used in investigating the morphology and nanoparticle size of NCs and energy dispersive X-ray (EDX) spectroscopy reveals the morphology and elemental composition of NCs. TEM can present high-resolution images, which is beneficial to study the nanostructure of plasmonic semiconductor NCs. In this work, TEM images were acquired with a JEOL-2010F microscope operating at 200 kV at McMaster University. TEM specimens were dropped onto copper grids with lacey Formvar/carbon support films purchased from Ted Pella, Inc.

2.3.3 X-ray Photoelectron Spectroscopy (XPS)

X-ray photoelectron spectroscopy (XPS) is a surface-sensitive quantitative tool measuring the elemental composition, electronic state and chemical state of the elements existing within materials.[109] XPS was conducted in precisely evaluating the doping concentration of Sb and Sn contents. In this thesis, XPS measurements were carried out with a Thermo-VG Scientific ESCALab 250 microprobe featuring a monochromatic AI Kα source

(1486.6 eV) in Dr. Tong Leung's lab in the Department of Chemistry at the University of Waterloo.

2.3.4 Ultraviolet-Visible-Near-Infrared (UV-vis-NIR) Spectroscopy

UV-vis-NIR spectroscopy is the most commonly used technique to measure the absorption of NCs among a certain wavelength range, where optical properties (absorption of band gap and LSPR) and electronic structures (band edge) of the NCs could be determined through the spectra. In this study, optical absorption spectra were collected with a Varian Cary 5000 ultraviolet-visible-infrared (UV-vis-NIR) spectrophotometer operated at room temperature. The suspensions of NCs were drop-casted onto quartz substrates, and the spectra were recorded from 200 nm to 3300 nm.

2.3.5 Fourier Transform Infrared (FTIR) Spectroscopy

FTIR spectroscopy can obtain optical properties of samples in the mid-infrared range because of its distinct frequencies of vibrations, which is considered as a powerful tool to identify the organic molecules/groups remained on the surface of NCs. FTIR measurement can also be applied in ascertaining the LSPR absorption of some plasmonic semiconductor NCs with relatively low free charge carrier concentration, of which plasmonic absorption happens in the MIR range. In this research, FTIR spectra were recorded in the range between 400 and 4000 cm^{-1} with a resolution of 0.5 cm^{-1} on the FTIR Bruker Tensor 37 spectrometer. Samples were prepared by drop-casting to pressed KBr pellets before the measurement.

2.3.6 Photoluminescence (PL) Spectroscopy

PL spectroscopy is a widespread technique to characterize the light emission properties of semiconductors. In this work, steady-state PL spectra were acquired at room temperature with a Varian Cary Eclipse fluorescence spectrometer. All samples were measured in liquid phase by dispersing in a hexane solvent. SnO_2 NC samples were excited at 240 nm with both excitation and emission slits set to 5 nm. ZnO NC samples were excited at 350 nm with excitation and emission slits set to 10 and 5 nm, respectively.

2.3.7 Magnetic Circular Dichroism (MCD) Spectroscopy

MCD spectroscopy can detect the differential absorption of left (ρ^-) and right (ρ^+) circularly polarized light of a sample, where the magnetic field is oriented parallel to the direction of light propagation.[20] The working fundamental of MCD is similar to UV-Vis-NIR spectroscopy, however, it would show more details and offer higher resolution results.

Generally, the MCD intensity, defined as ΔA, needs to be converted from ellipticity (θ) to $\Delta A/A$ form by using this relationship:

$$\frac{\Delta A}{A} = \frac{\theta}{32982 \times A} \qquad (2.3)$$

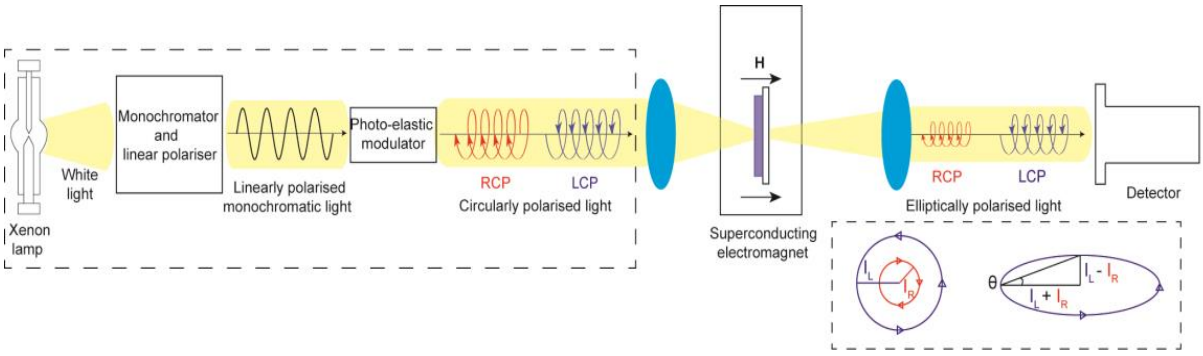

Figure 2.3 Magnetic circular dichroism setup, including three major parts: circularly polarized light generation component (left dashed frame), superconducting cryostat with external magnetic field, and detector.[20]

where $\Delta A = A_L - A_R$ (A_L and A_R refer to the absorption of LCP and RCP, respectively), A is the band gap absorbance collected by circular dichroism detector, and θ is ellipticity in millidegrees.

Figure 2.3 displays MCD experimental setup and basic measurement process.[20] The white light emitted by the xenon lamp is passed through a monochromator and a linear polarizer to produce linearly polarized monochromatic light. It is then passed through a photo-elastic modulator to generate LCP and RCP light. A sample is pre-mounted in a superconducting magneto-optical cryostat with a magnetic field parallel to the direction of light propagation. Upon moving through the sample, LCP and RCP beams are absorbed to a different degree. Different intensities of LCP and RCP light (I_L and I_R, respectively) are combined to form an elliptically polarized beam and the signal is collected by the detector. The ellipticity (θ) defined as the angle between the long and short axes of an ellipse is then converted to a differential absorption in accordance with Equation (2.3).

In this study, the MCD measurement was carried out in a Faraday configuration using a Jasco J815 spectropolarimeter. Samples deposited on clean and strain-free quartz substrates were placed in an Oxford SM 4000 magneto-optical cryostat with controllable temperature from 5 K to 300 K as well as a controllable field between 0 and 7 T.

In MCD data analysis, the Brillouin function is applied to fit the field-dependent MCD intensities, and the equation is dressed here:

$$M_S = \frac{1}{2} N g_S \mu_B [(2S+1)] \coth\left((2S+1)\frac{g_S \mu_B B}{2k_B T}\right) - \coth\left(\frac{g_S \mu_B B}{2k_B T}\right)] \qquad (2.3)$$

where N refers to the carrier concentration as the fitting parameter; B is the external magnetic field strength; M_S is the sample saturation magnetization; T is the temperature; k_B is the Boltzmann constant; and μ_B is the Bohr magneton.

Chapter 3

Manipulating Plasmonic Properties of Sb-Doped SnO_2 Nanocrystals

In this chapter, I investigated the role of the synthesis approach and post-synthesis processing on the plasmonic properties of antimony-doped SnO_2 NCs. I synthesized Sb:SnO_2 NCs by solvothermal and coprecipitation methods, and directly compared their structural, electronic, optical, and magneto-optical properties, including TEM, XRD, XPS, UV-vis-NIR, and MCD characterizations. The results of this work demonstrate that the choice of synthesis methodology and post-synthesis processing allows for the control of the plasmonic properties *via* redox chemistry of aliovalent dopant ions. This chapter is adapted from the following publication:

Zhang, C.; Yin, P.; Radovanovic, P.V. "Manipulating Plasmonic Properties of Sb-Doped SnO_2 Nanocrystals by Controlling Dopant Oxidation State via Synthesis Method and Processing Conditions" *ECS Trans*. **2020**, 98(3) 77-86.

I am the primary contributor in designing the experiment, analyzing the data, and writing the paper. The other co-authors contributed in guiding the experiment and writing the paper.

3.1 Structure and Morphology of SnO_2 and ATO NCs

Overview TEM images of typical ATO NCs synthesized by coprecipitation and solvothermal methods are shown in Figure 3.1a and b, respectively. The two images appear qualitatively similar, although NCs synthesized by coprecipitation method are somewhat smaller and more aggregated. High-resolution TEM images show lattice fringes in individual NCs indicating their single crystalline form (insets in the corresponding panels in Figure 3.1).

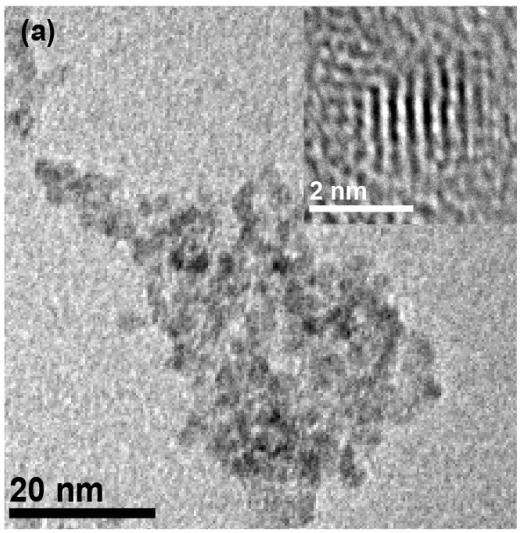

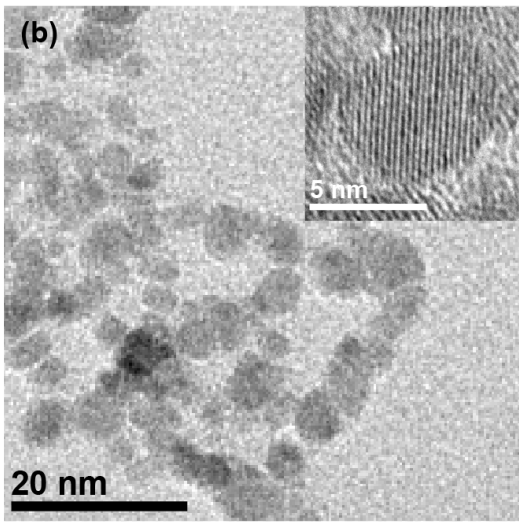

Figure 3.1 TEM images of typical ATO NCs synthesized by (a) coprecipitation and (b) solvothermal method. Insets are high-resolution images of representative individual NCs.

X-ray diffraction patterns of ATO NCs prepared by coprecipitation method, having different nominal doping concentrations, are shown in Figure 3.2a. All peaks can be readily indexed to cassiterite SnO_2 (vertical red lines), and no secondary phases are evident in any of the collected XRD patterns. However, significant peak broadening suggests that these NCs are very small, consistent with the TEM images in Figure 3.1a. The XRD patterns of typical solvothermally-synthesized ATO NCs having different nominal doping concentrations are shown in Figure 3.2b. These patterns are also in excellent agreement with that of bulk cassiterite SnO_2. The XRD peaks in Figure 3.2b are narrower, which is most likely associated with the larger average NC size. The accurate sizes of as-synthesized ATO NCs were determined according to the Scherrer equation (Equation 2.2), where K is a constant equal to 0.9. The calculated results of solvothermally and coprecipitation-prepared ATO NCs are shown in Tables 3.1 and 3.2.

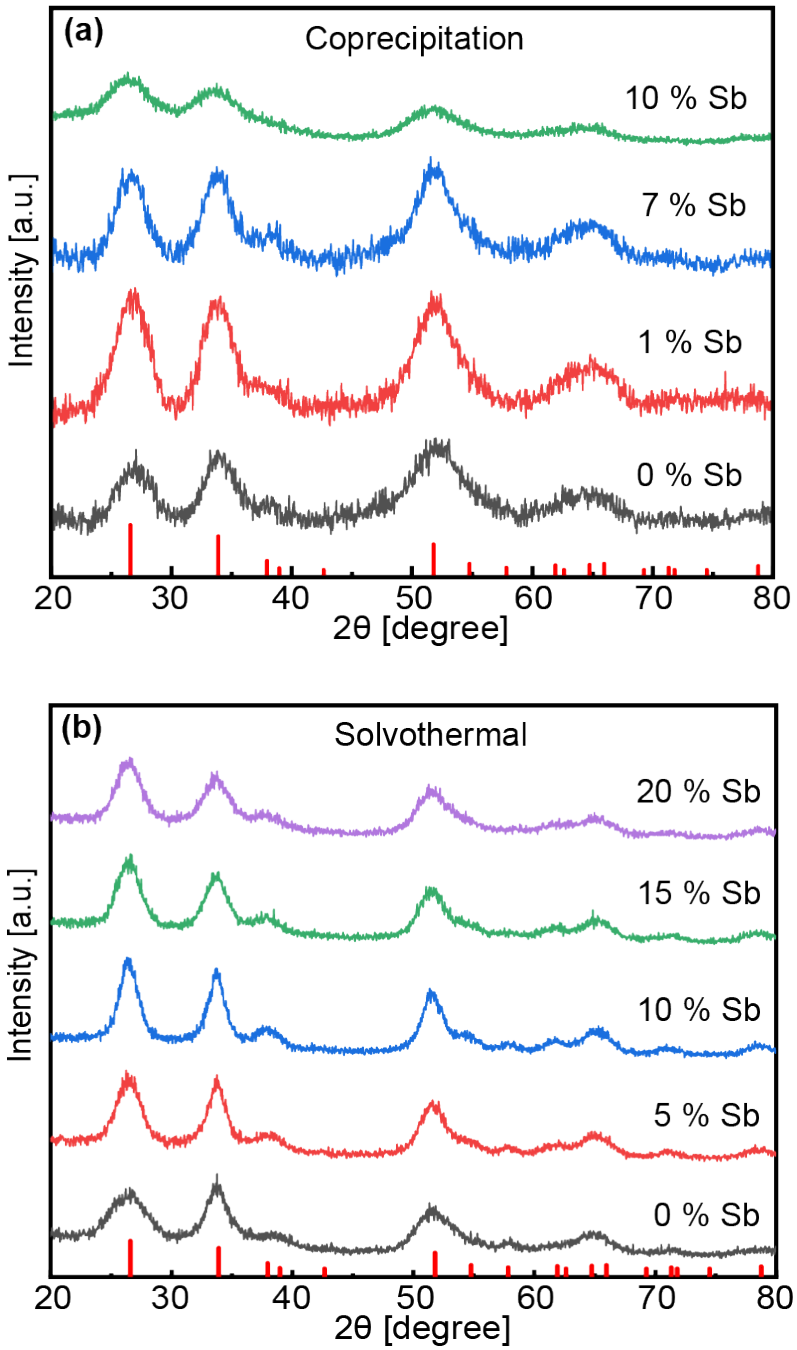

Figure 3.2 XRD patterns of ATO NCs having different nominal doping concentrations, as indicated in the graphs, synthesized by (a) coprecipitation and (b) solvothermal method. Vertical red lines represent the pattern of bulk cassiterite SnO_2 (JCPDS 41-1445).

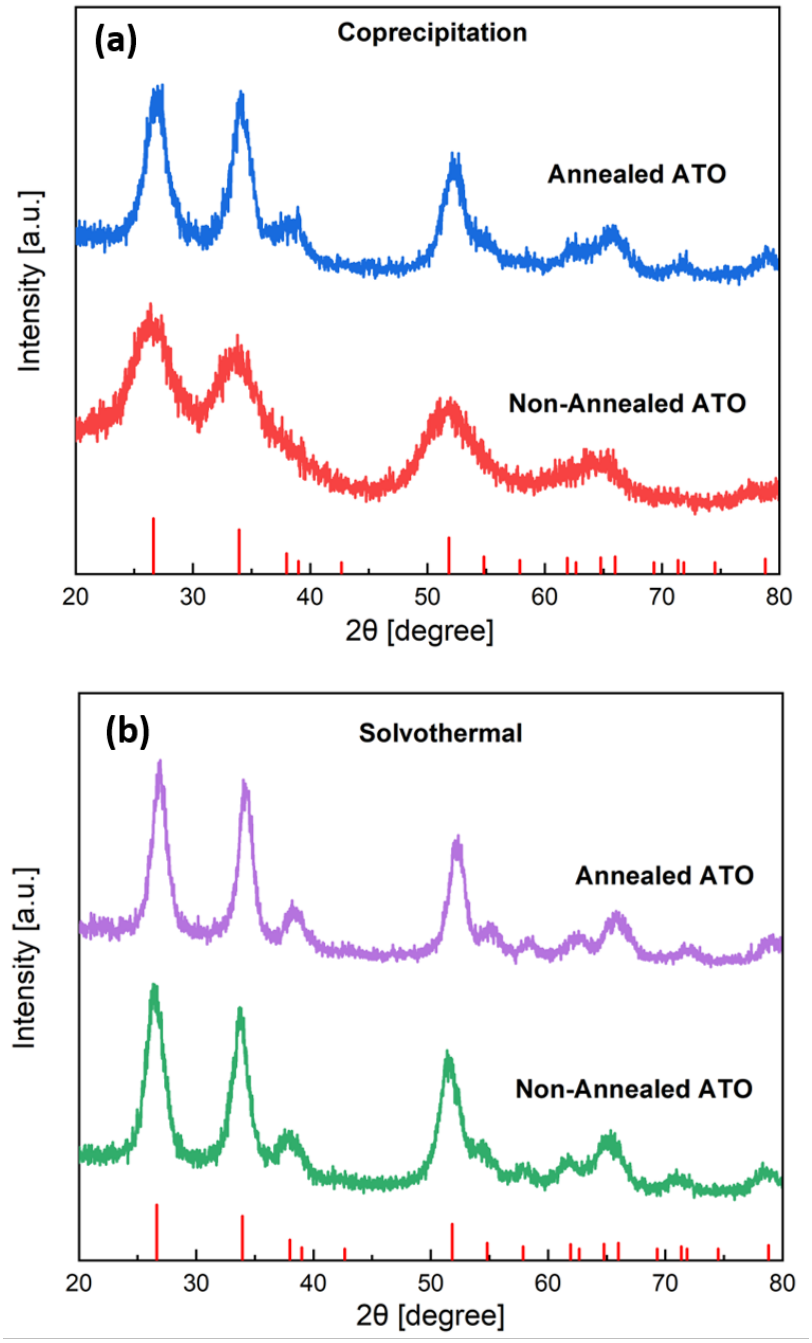

Figure 3.3 XRD patterns of 10 % Sb:SnO_2 NCs annealed at 500 °C for 2 hours under the same conditions for NCs synthesized by (a) coprecipitation and (b) solvothermal method. The XRD patterns of the same samples before annealing are shown in the graphs for comparison. Vertical red lines represent the pattern of bulk cassiterite SnO_2 (JCPDS 41-1445).

Table 3.1 Calculated size of coprecipitation-synthesized ATO NCs with different nominal doping concentrations.

Sample	SnO_2	1% ATO	7% ATO	10% ATO
Size (nm)	3.8	3.6	2.8	2.7

Table 3.2 Calculated size of solvothermally-synthesized ATO NCs with different nominal doping concentrations.

Sample	SnO_2	5% ATO	10% ATO	15% ATO	20% ATO
Size (nm)	3.1	3.8	5.1	4.2	3.5

X-ray diffraction patterns of coprecipitation and solvothermally-synthesized ATO NCs upon annealing at 500 °C for 2 h are shown in Figure 3.3a and b (blue and purple traces). Compared with the XRD patterns of the same samples before thermal annealing (red and green traces), especially for the coprecipitation-prepared ATO NCs, remarkable peak narrowing and FWHM reducing reveal that these NCs became much larger after annealing processing, which can be attributed to the increase in particle size and/or grain growth due to the high-temperature annealing thus improving the crystallinity of Sb-doped SnO_2.[110]

3.2 Optical Properties of SnO_2 and ATO NCs

Optical absorption spectra of ATO NCs from Figure 3.2a are shown in Figure 3.4a. The most notable spectral feature is a strong band gap absorption with the onset at ca. 300 nm. No discernable absorption was detected in the NIR range, suggesting the absence of a strong LSPR. It is not excluded, however, that some plasmon oscillations exist, but result in a broad and weak absorption band below the detection limit of our spectrophotometer. Figure 3.4b shows the Tauc plots for ATO NCs in Figure 3.4a. The band-edge absorption of ATO NCs shifts to slightly higher energies relative to undoped SnO_2 NCs, and varies within ca. 0.1 eV for the studied doping concentration range. This shift suggests a change in the NC host lattice electronic structure induced by quantum confinement[104] and/or the substitutional incorporation of Sb dopants. Figure 3.4c shows absorption spectra of solvothermally-prepared ATO NCs having varying doping concentrations. In contrast to coprecipitation-synthesized NCs, these spectra display a broad band in the NIR range that increases in intensity and blue shifts with increasing doping concentration. Based on their behaviour, these bands are readily attributed to the LSPR.[30] The increase in the intensity of the LSPR band is accompanied by a systematic shift of the band edge absorption to higher energies (Figure 3.4d), despite the fact the solvothermally-synthesized NCs have larger average sizes, and therefore less pronounced quantum confinement effects. The shift in the absorption arises from the Burstein-Moss effect, which is associated with increased electron occupancy of the conduction band states, and is consistent with the appearance of LSPR band in NIR.[19,30]

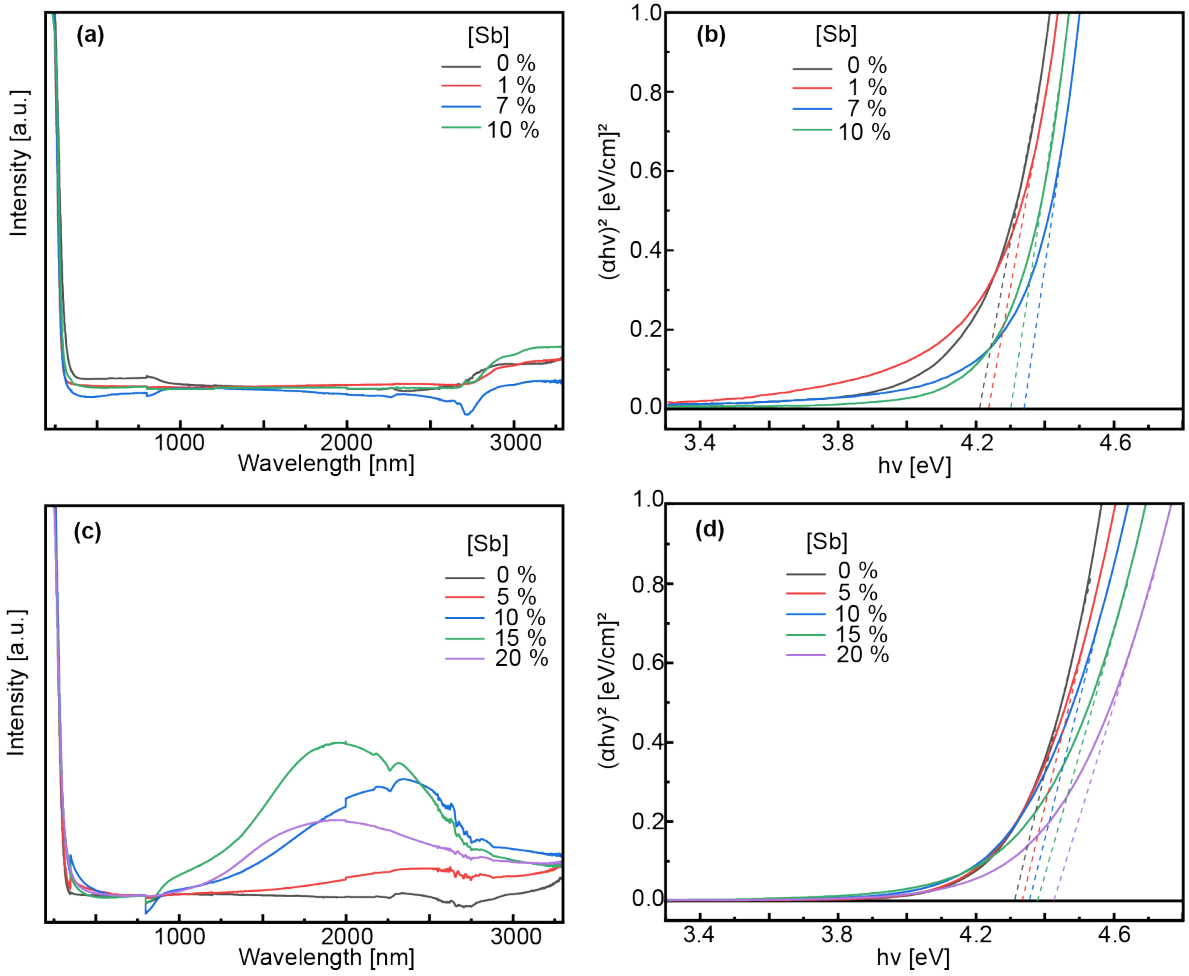

Figure 3.4 (a, c) Band-gap-normalized absorption spectra of ATO NCs having different nominal doping concentrations, as indicated in the graphs, synthesized by (a) coprecipitation and (c) solvothermal method. (b, d) Tauc plots for ATO NCs synthesized by (b) coprecipitation and (d) solvothermal method.

Several important questions emerge from these results. For example, what is the origin of the difference in plasmonic properties of ATO NCs synthesized by different methods? What roles do the synthesis methodology and conditions play in defining the plasmonic properties of ATO NCs? How can the plasmonic properties of ATO NCs be controlled? One of the simplest ways to test the possibility of post-synthesis manipulation of LSPR in ATO NCs is through thermal annealing. Figure 3.5a shows the absorption spectra of typical ATO NCs synthesized by coprecipitation method upon annealing at 500 °C for different durations. Upon annealing the NCs for only 5 minutes, a robust LSPR band appears in the absorption spectrum, suggesting a strong dopant activation. Further annealing causes only incremental enhancement in the LSPR intensity. On the other hand, annealing solvothermally-synthesized NCs at the same temperature and for the same durations leads to much less pronounced and more gradual increase in the LSPR intensity (Figure 3.5b). To directly compare the effect of the synthesis conditions on the plasmonic properties of ATO NCs, we show in Figure 3.6 the band-gap-normalized absorption spectra of ATO NCs, synthesized by the two methods, before and after annealing at 1000 °C. Interestingly, the NCs synthesized by coprecipitation method experience comparable LSPR intensity to that of the NCs synthesized by the solvothermal method upon annealing. This is despite the fact that the LSPR band is non-observable in solvothermally-synthesized NCs before annealing. These results emphasize the ability to optimize plasmonic properties of ATO NCs by simple post-synthesis treatment.

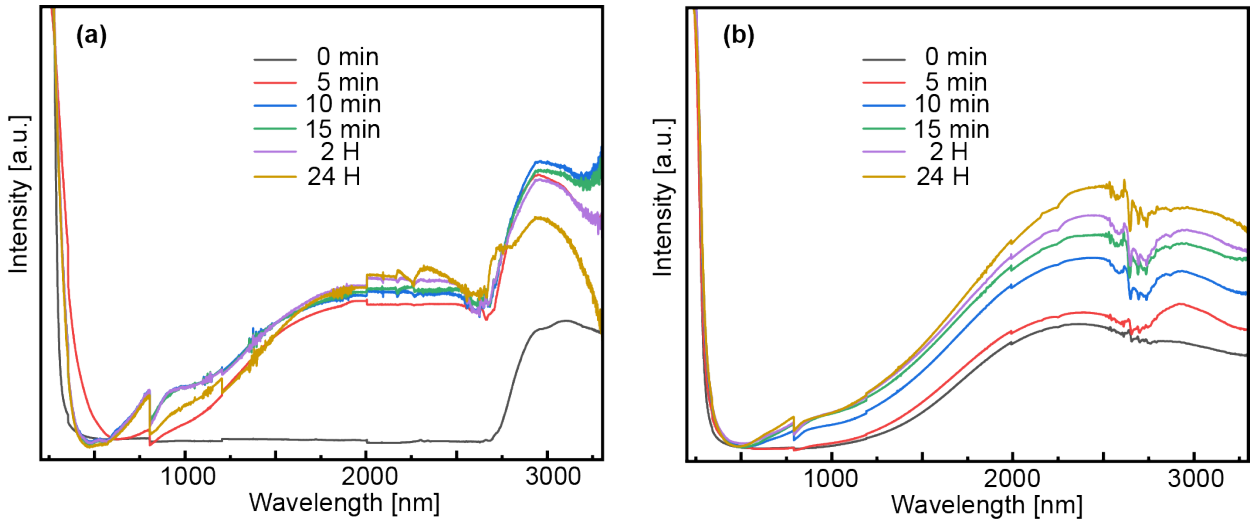

Figure 3.5 Absorption spectra of 10 % Sb:SnO_2 (ATO) NCs annealed at 500 °C for different durations, as indicated in the graphs, for NCs synthesized by (a) coprecipitation and (b) solvothermal method.

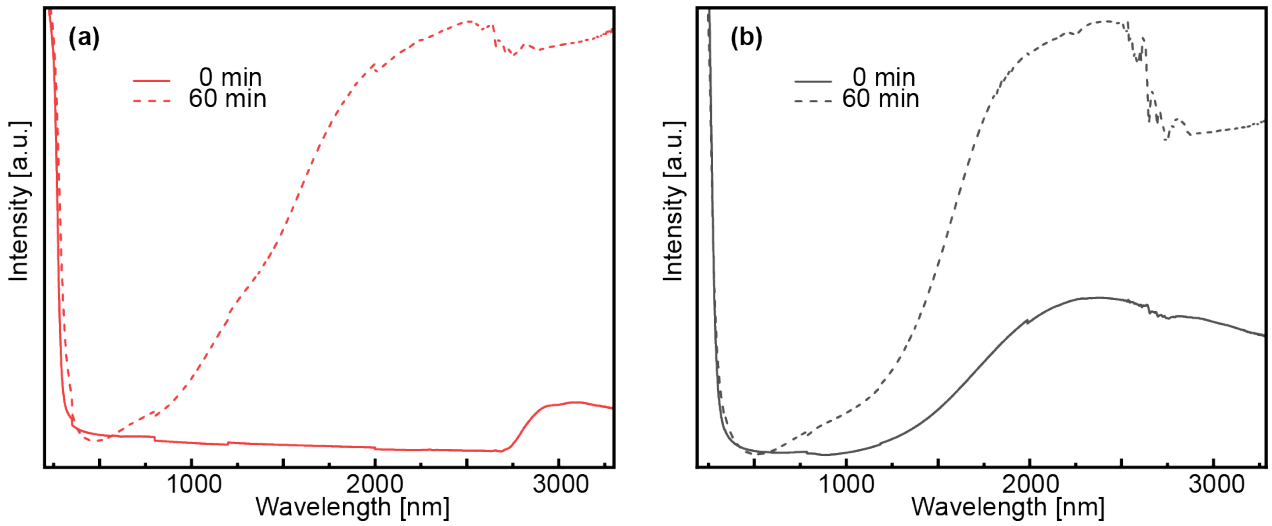

Figure 3.6 Band-gap-normalized absorption spectra of ATO NCs annealed at 1000 °C for 60 minutes under the same conditions for NCs synthesized by (a) coprecipitation and (b) solvothermal method. The spectra of the same samples before annealing are shown in the graphs for comparison.

3.3 Magneto-optical Properties of SnO_2 and ATO NCs

Figure 3.7 (bottom panel) compares the MCD spectra of 10 % Sb:SnO_2 NCs synthesized by coprecipitation (red solid line) and solvothermal (black solid line) method in the range between 200 and 450 nm, recorded at 5 K and 7 T. Both negative MCD bands with maximum intensities at ca. 4.5 (red band) and 4.3 (black band) eV coincide with the band gap absorption shown in the top panel, affirming the excitonic origin of these bands. By comparison of the MCD intensities, it is clearly seen that the MCD intensity of solvothermally-prepared ATO NCs is around twice as strong as that of coprecipitation-prepared ones, suggesting a strong plasmon-exciton interaction in the former NCs. This result is in agreement with the LSPR absorption spectra where ATO NCs synthesized by solvothermal method had a strong plasmonic absorption with a broad peak in the NIR range, while no discernable LSPR was detected for the NCs synthesized by coprecipitation approach in the accessible spectral range. Additionally, based on the excitonic MCD spectra of coprecipitation-prepared ATO NCs, we could confirm the presence of free charge carriers, but the plasmon is too week to be detected due to the limitation of our spectrophotometer. Combined with UV-vis-NIR absorption and MCD spectra, it is concluded that the plasmonic properties of Sb-doped SnO_2 NCs could be manipulated by synthesis methods.

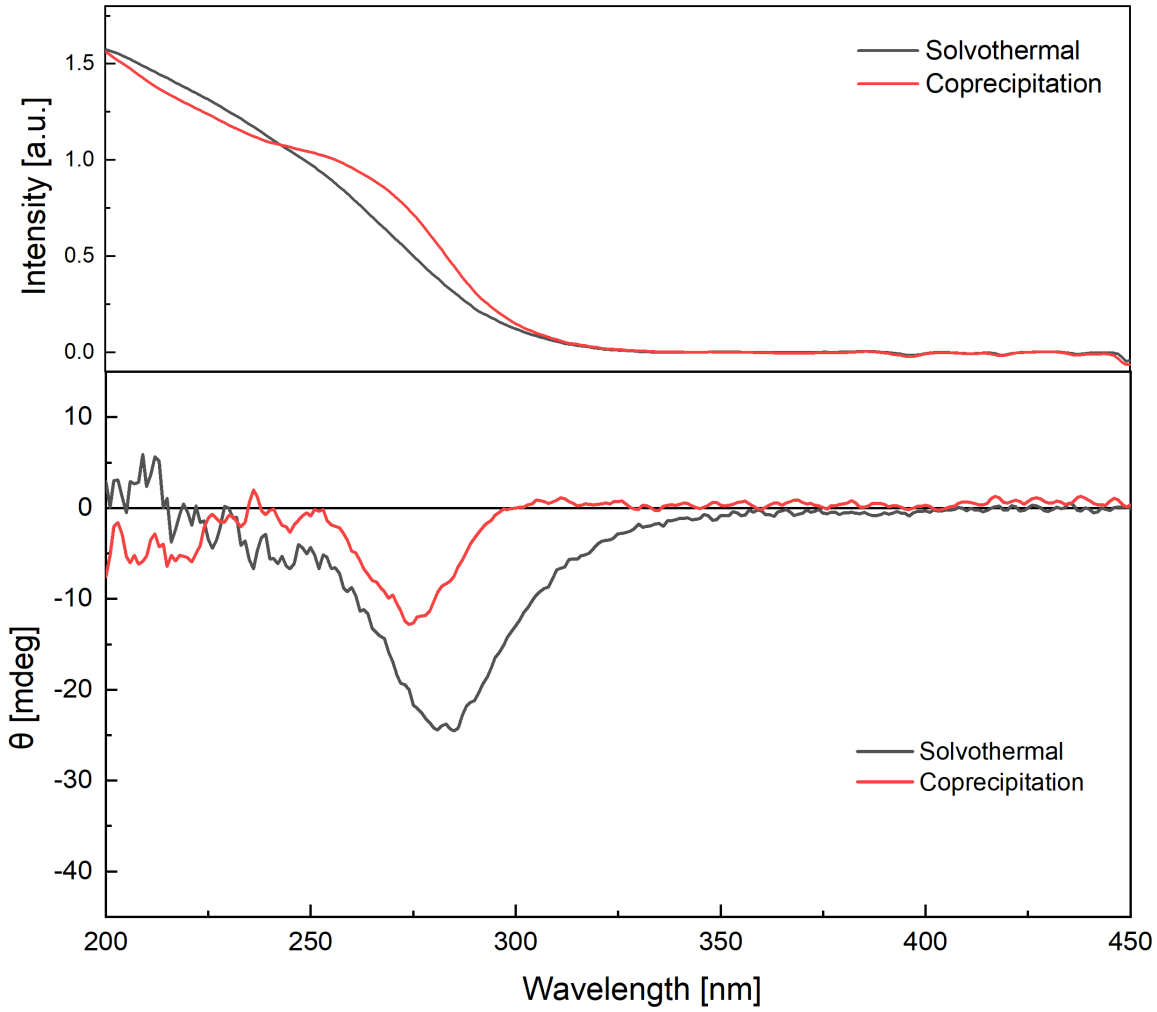

Figure 3.7 Absorption (top panel) and MCD (bottom panel) spectra of 10 % Sb:SnO_2 NCs synthesized by coprecipitation (red solid lines) and solvothermal (black solid lines) method. MCD spectra were recorded at 5 K and 7 T.

In order to further present the effects of thermal annealing on the LSPR properties of Sb-doped SnO_2 NCs, the MCD measurements were performed for coprecipitation-synthesized ATO NCs annealed at 500 °C for varying durations from 1 to 10 min, collected at 300 K and 7 T (Figure 3.8, bottom panel). The band gap absorptions are shown in the top panel of Figure 3.8 to confirm their excitonic origin. From the MCD spectra, a sustained increase from 18 to 32 mdeg in excitonic MCD intensities was observed with increasing annealing time, which is strongly correlated with an increased LSPR absorption. These results further suggest enhanced plasmon-exciton correlation. These results are consistent with the optical absorption spectra and evidently demonstrate the feasibility of post-synthesis treatment to modulate plasmonic properties of ATO NCs.

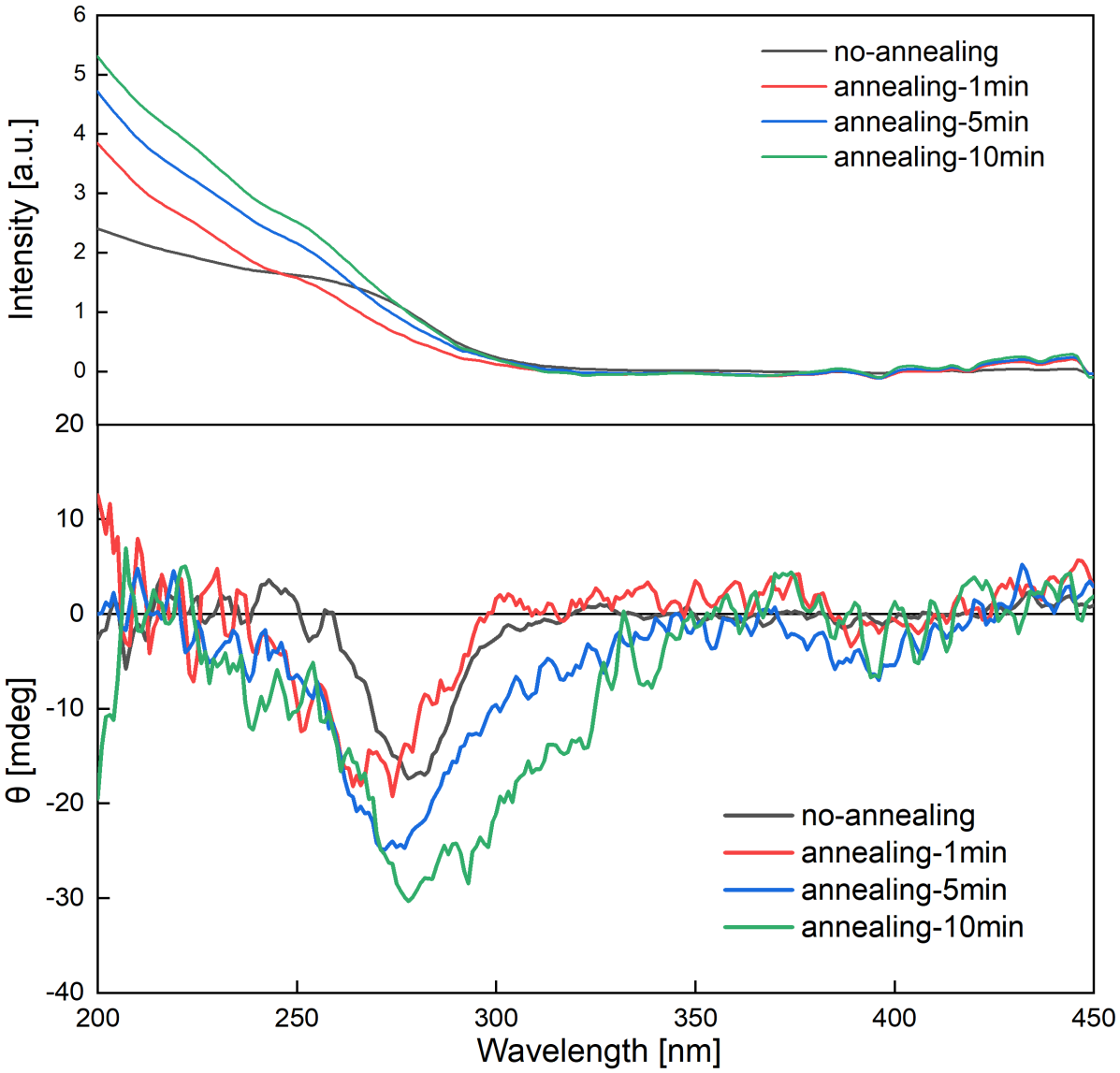

Figure 3.8 Absorption (top panel) and MCD (bottom panel) spectra of coprecipitation-synthesized 10 % Sb:SnO_2 NCs annealed at 500 °C for different durations, as indicated in the graph. MCD spectra were collected at 300 K and 7 T.

3.4 Electronic Properties of SnO_2 and ATO NCs

Based on the redox properties of the antimony ions discussed in the Introduction, we hypothesized that the dependence of the plasmonic properties of ATO NCs on the synthesis conditions and annealing is largely associated with the dopant ion oxidation states. To test this hypothesis we performed XPS measurements on typical ATO NCs prepared by coprecipitation and solvothermal methods before and after their annealing. One of the challenges associated with the antimony XPS analysis is the fact the Sb $3d_{5/2}$ peaks, as the most prominent Sb spectral feature, overlaps with O 1s peak. Therefore, we used Sb $3d_{3/2}$ region for the oxidation state analysis. Figure 3.9a shows Sb $3d_{3/2}$ XPS spectrum of ATO NCs synthesized by the coprecipitation method. The asymmetric configuration of the band suggests the presence of Sb with at least two different speciations. By fitting the XPS spectrum with Voigt function we identified two peaks at ca. 539.7 eV and 541.3 eV, which can be assigned to Sb^{3+} and Sb^{5+}, respectively,[19] with Sb^{3+} having the dominant contribution. This is exactly opposite from the ATO NC prepared by solvothermal method, for which Sb^{5+} is the dominant feature (Figure 3.9c). The presence of a larger amount of Sb^{5+} in solvothermally-synthesized ATO NCs is consistent with the stronger LSPR in these NC samples. Upon annealing the NCs from Figure 3.9a, the intensities of $3d_{3/2}$ peaks for Sb^{3+} and Sb^{5+} reverse (Figure 3.9b), indicating that Sb^{3+} is oxidized to Sb^{5+} in the annealing process. Similarly, annealing ATO NCs from Figure 3.9c causes further increase in the amount of Sb^{5+} at the expense of Sb^{3+} (Figure 3.9d). The final Sb^{3+}/Sb^{5+} ratio in Figure 3.9b and d is very similar, suggesting that the equilibrium between these two oxidation states is reached for the given annealing conditions. One of the key questions is what determines the different average oxidation state for the two synthetic

methodologies explored in this work. One of the possibilities is that the coprecipitation method provides more reducing conditions, enabled by the presence of NH_4OH, which prevents an effective oxidation of Sb^{3+}. This phenomenon has been observed for other dopant ions in transparent metal oxide NCs synthesized under reducing conditions.[111,112]

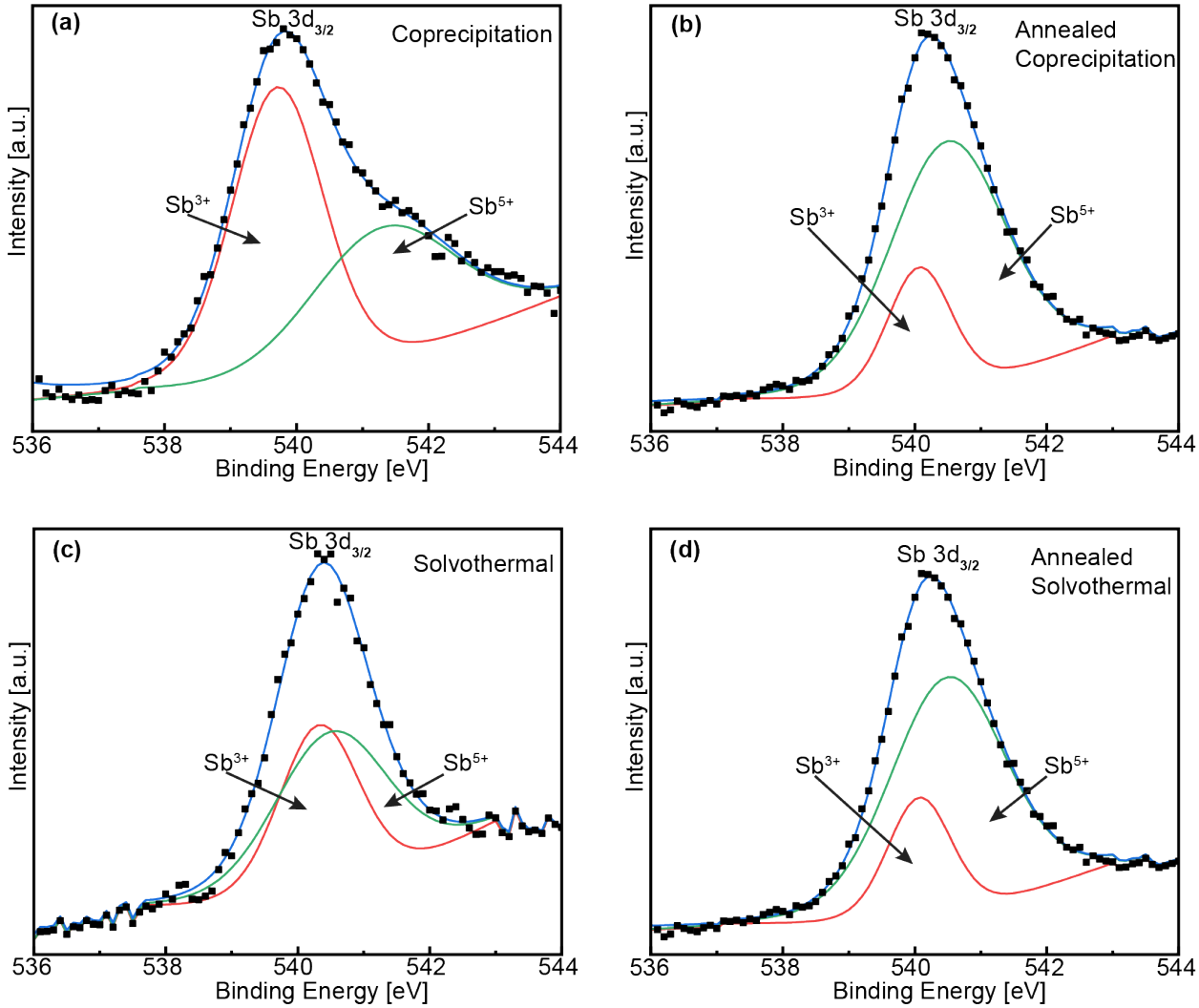

Figure 3.9 (a, b) Sb $3d_{3/2}$ XPS spectra of typical coprecipitation-synthesized ATO NCs (a) before and (b) after annealing. (c, d) Sb $3d_{3/2}$ XPS spectra of typical solvothermally-

synthesized ATO NCs (c) before and (d) after annealing. Red and green traces are best fits for Sb^{3+} and Sb^{5+}, respectively, and blue trace is the overall fit to the experimental data points.

3.5 Conclusions

In summary, we investigated the effect of the synthesis method and subsequent thermal annealing on the plasmonic properties of ATO NCs. The ATO NCs having variable doping concentration were prepared by the coprecipitation and solvothermal methods and their structure, optical, and magneto-optical properties were investigated. Unlike solvothermally-synthesized ATO NCs, those prepared by the coprecipitation method do not show discernable LSPR band in the NIR. However, upon thermal annealing, the LSPR absorption emerges in the NCs prepared by coprecipitation method. Annealing also enhances the existing LSPR intensity in solvothermally-synthesized NCs. For both synthetic methods the LSPR intensity is correlated with the oxidation of Sb^{3+} to Sb^{5+}. The difference in the ratio of the antimony oxidation states in ATO NCs synthesized by the two applied methods suggests a more reducing environment for coprecipitation method, which may be enabled by the presence of ammonium hydroxide as a reducing agent. The results of this work demonstrate that synthesis methodology can dramatically influence the plasmonic properties of aliovalently-doped semiconductor NCs *via* dopant oxidation state, and the selection of synthesis methodology and processing conditions can be used to design semiconductor NCs with targeted plasmonic properties.

Chapter 4

Effect of Oxygen Vacancy on Excitonic Splitting in ZnO and SnO_2 Nanocrystals

In this chapter, I demonstrated the effect of oxygen vacancies on conduction band splitting in ZnO and SnO_2 NCs. I synthesized ZnO NCs by colloidal and SnO_2 NCs by coprecipitation and solvothermal methods, and conducted several measurements including TEM, UV-vis-NIR, PL, and MCD spectroscopy to investigate their morphology, optical properties, and carrier polarization. The result of this work suggests that localized electrons affiliated with oxygen vacancies can activate electron polarization and NC band splitting in ZnO and SnO_2 NCs without the addition of magnetic impurities.

4.1 Study of ZnO NCs

4.1.1 Morphological and Optical Properties of ZnO NCs

Colloidal ZnO NCs were synthesized by a non-injection method under a reducing atmosphere (7% hydrogen in nitrogen, referred to as hydrogen) and under an oxidizing surrounding (air) to manipulate the defect density, particularly the oxygen deficiency in the crystal lattices. As shown in Figure 4.1a, the top low-resolution TEM image reveals that as-synthesized NCs in hydrogen atmosphere have spherical and quasi-spherical shapes with uniform size distribution. While the bottom low-resolution TEM image shows that the NCs synthesized in air have irregular shapes with relatively uniform size distribution. By

comparison between the high-resolution TEM images, it can be intuitively seen that the NCs synthesized in the air have a larger size than those synthesized in hydrogen, implying the oxidizing condition would be apt to tune the crystal growth rate and promote the NC growth. The reason could be explained that the air atmosphere surrounded by oxygen and water molecules could saturate the oxygen vacancies and supply hydroxyl groups to accelerate the NC growth.[113] The UV-Vis absorption spectra were obtained and their corresponding Tauc plots are given in Figure 4.1b to determine the approximate optical band gaps. The ZnO NCs prepared in hydrogen have a larger band gap as reducing conditions lead to increasing the probability for forming oxygen vacancies and maximizing their concentration. In contrast, the ZnO NCs synthesized in the air would limit oxygen vacancies, resulting in a lower band gap energy. Moreover, the band gap result is consistent with the TEM images, which shows smaller NCs possess higher optical band gaps.[59] Additionally, the exciton Bohr radius of bulk ZnO has been reported as 2.34 nm,[114] which is much smaller than the as-synthesized NCs according to their sizes displayed in TEM images, therefore, the quantum confinement effects can be neglected. Figure 4.1c shows PL emission spectra of ZnO NCs. A broad emission peak with the maximum emission at ca. 500 nm appears for ZnO NCs formed in reducing atmosphere. This visible emission peak may be attributed as defect-related emission caused by the combination of singly charged oxygen vacancies (V_O^+) and neutral oxygen vacancies (V_O^X).[115] Interestingly, no discernable PL emission peak (red trace) was detected for ZnO NCs prepared in air, indicating the lack of oxygen vacancies.

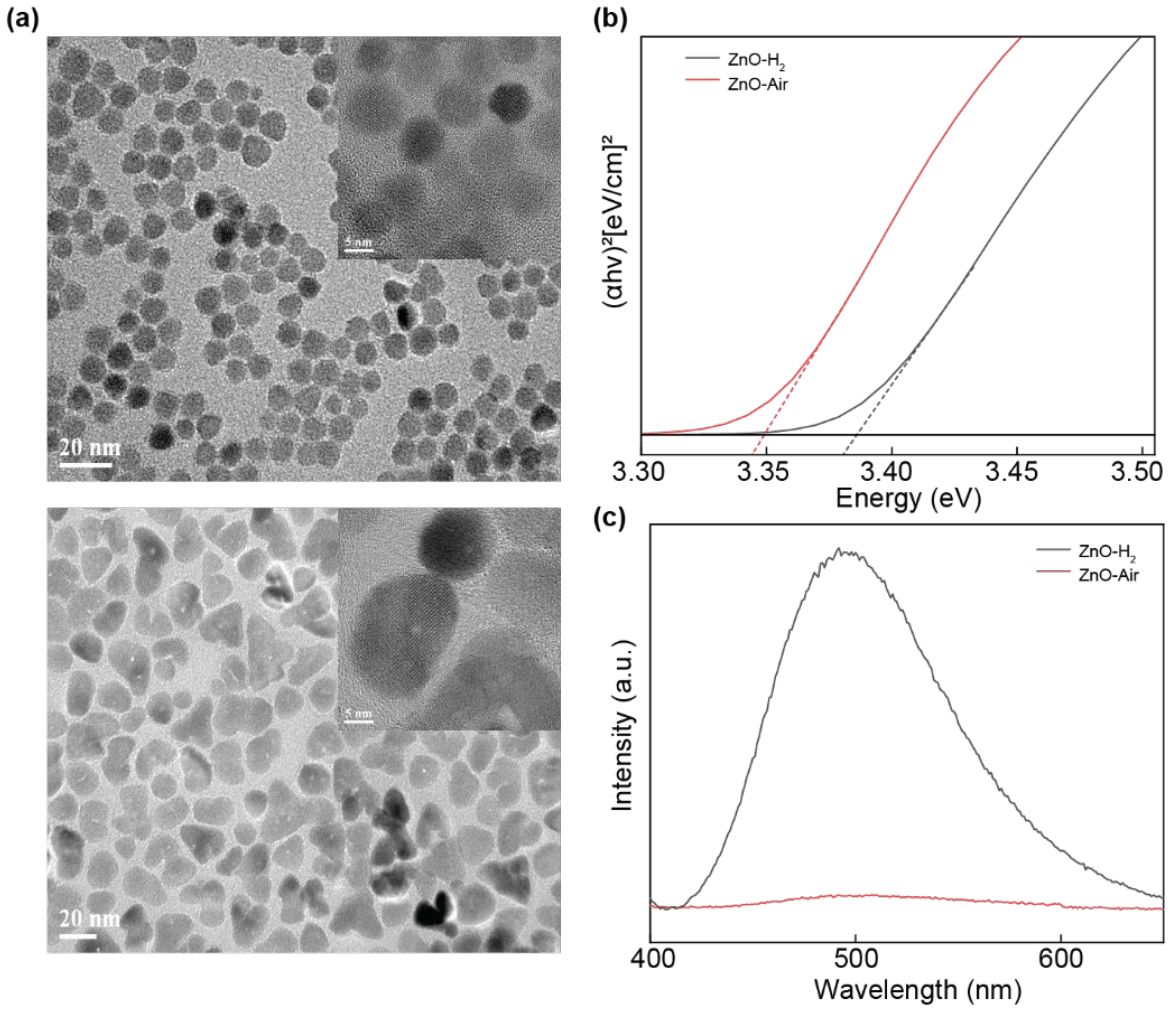

Figure 4.1 (a) TEM images of ZnO NCs synthesized in hydrogen (top panel) and air (bottom panel). (b) Tauc plots for optical band gap determination of the hydrogen- and air-ZnO NCs. (c) PL emission spectra of as-synthesized hydrogen- and air-ZnO NCs with the excitation wavelength of 350 nm.

4.1.2 Carrier Polarization in ZnO NCs

MCD spectroscopy was used in this work to examine the excitonic properties and evaluate the role of defects in the magneto-optical response of ZnO NCs. Figure 4.2a shows 5 K MCD spectra of ZnO NCs synthesized in oxygen-free conditions with variable magnetic fields. The spectra were collected in the range of 330 to 400 nm which is around the band gap region. Intriguingly, a robust derivative-shape signal appears cohering with the band gap absorption, announcing strong excitonic splitting in these ZnO NCs. The integrated MCD intensity is plotted as a function of the applied magnetic fields from 0 to 6 T (Figure 4.2b). The red curve exhibits a saturation at high magnetic fields, and this behaviour is always characteristic of paramagnetic materials. Providing this splitting comes from the localized unpaired electrons affiliated with defects, in this case, oxygen vacancies, we used a Brillouin function with spin state S = 1/2, electron-spin Landé g-factor, g_S = 2.002, and carrier concentration N as the sole fitting parameter to fit the integrated MCD intensity data points:

$$M_S = \frac{1}{2} N g_S \mu_B [(2S+1)] \coth\left((2S+1)\frac{g_S \mu_B B}{2k_B T}\right) - \coth\left(\frac{g_S \mu_B B}{2k_B T}\right)].$$

As expected, the red curve in Figure 4.2b demonstrates an ideal Brillouin fit, suggesting that the NC band states are able to be spin-split by defects such as oxygen vacancies, associated with localized unpaired electrons, which is analogous to transition metal dopants in DMSs.[71,116] We also collected the MCD spectra at 7 T with various temperatures to investigate the temperature dependence. As shown in Figure 4.2c, the absolute value of MCD intensity decreases sharply at the low temperature and levels off after 200 K. We plotted the integrated MCD intensity with respect to the temperature in Figure 4.2d. The red curve shows an inversely

proportional relationship to temperature in light of Curie's law, indicating that paramagnetic centers exist in hydrogen-synthesized ZnO NCs.

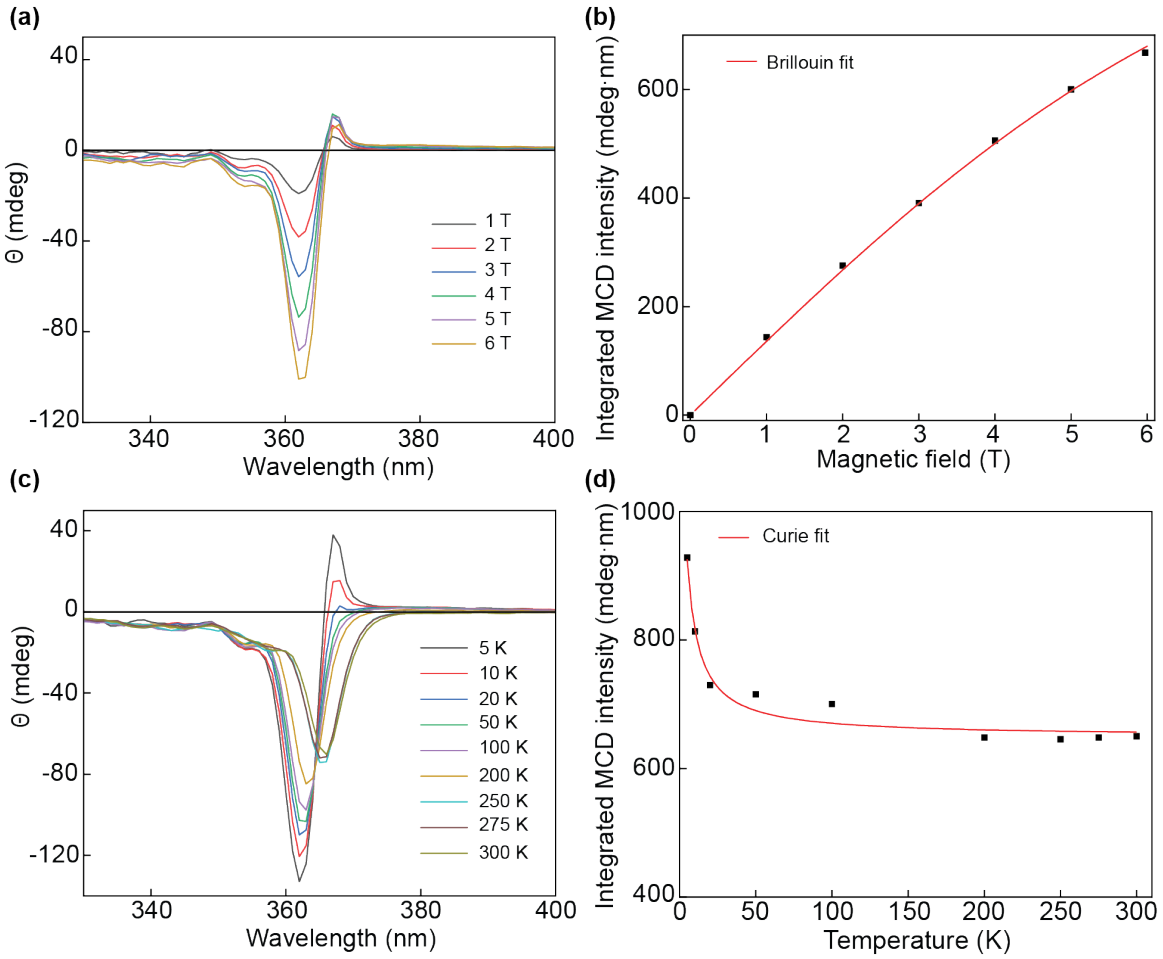

Figure 4.2 (a) MCD spectra of ZnO NCs prepared in hydrogen recorded at 5 K for different external magnetic fields. (b) Magnetic-field dependence of integrated MCD intensity for ZnO NCs synthesized in hydrogen. Red line is the best fit of the integrated excitonic intensity with the Brillouin function for *S* = 1/2. (c) MCD spectra collected at 7 T for varying temperatures of ZnO NCs prepared in hydrogen. (d) Temperature dependence of integrated MCD intensity for ZnO NCs synthesized in hydrogen. Red line is the best fit of the Curie-Weiss law to the corresponding experimental data points.

Temperature-dependence MCD measurement plays a vital role in addressing the nature of band splitting in semiconductor NCs. To further investigate the defect impacts on excitonic splitting, we conducted the MCD measurement at 7 T for temperatures between 5 and 200 K for ZnO NC samples which were synthesized in air and subsequently annealed at 500 ℃ for 12 hours (Figure 4.3). Thermal annealing processing is taken advantage of cramming the oxygen vacancies in the ZnO NC lattices. Surprisingly, Curie-type decay completely disappeared. Instead, all spectra are practically identical, revealing the temperature-independent behaviour of the excitonic MCD intensity. This indicates that there are very few unpaired localized electrons owing to the filled oxygen vacancies in the oxygen-rich synthesis conditions and annealing post-processing. Taken together with PL results, it can be concluded that the Curie behaviour can be tuned *via* manipulating NC defects by means of controlling synthesis conditions and/or post-processing treatment. This result is novel and thrilling as it is the first demonstration that ZnO NC band splitting and carrier polarization can be induced by localized electrons associated with oxygen vacancies instead of incorporating magnetic dopants in semiconductor NCs.

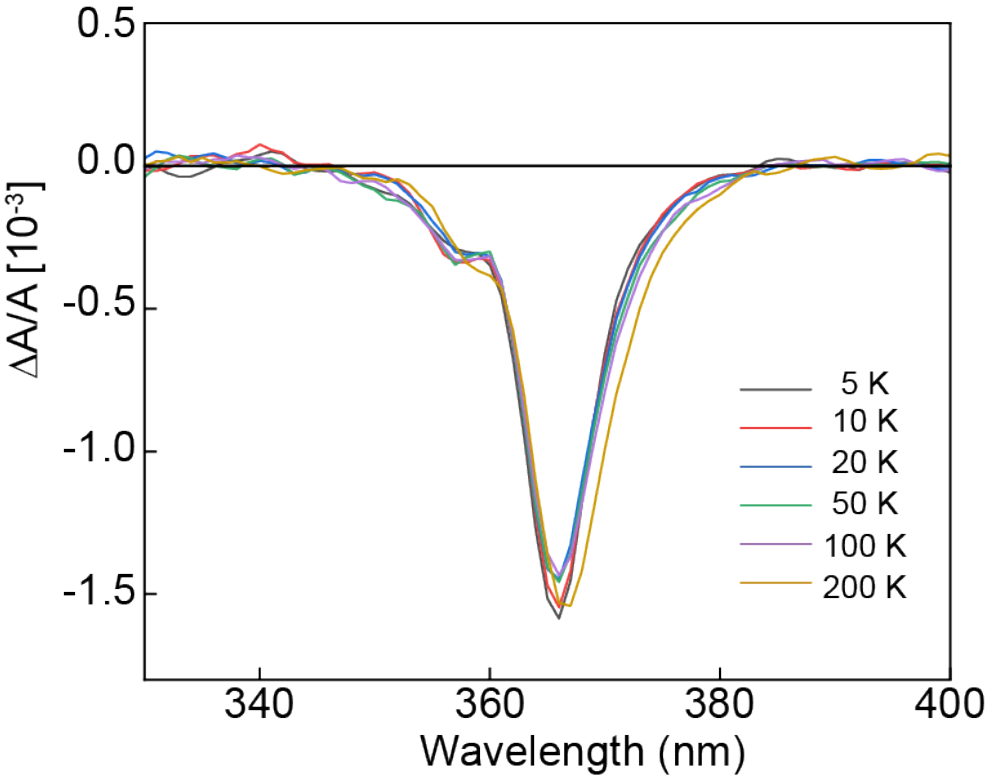

Figure 4.3 MCD spectra collected at 7 T for varying temperatures of ZnO NCs prepared in air and annealed at 500 ℃ for 12 hours.

4.2 Study of SnO_2 NCs

4.2.1 Carrier Polarization in Solvothermally-Synthesized SnO_2 NCs

In order to demonstrate the universality of defect-induced band splitting, we synthesized SnO_2 semiconductor NCs using two different synthesis methodologies,

solvothermal and coprecipitation approaches. Figure 4.4a shows the MCD spectra of solvothermally-synthesized SnO_2 NCs at 5 K with different external magnetic field strengths. As with the MCD results of ZnO NCs, the baseline for each MCD spectrum of SnO_2 NCs is well-matched, and we can see that the difference of the maximum MCD intensity between each adjacent trace becomes smaller with increasing external magnetic field, implying a characteristic paramagnetic behaviour. The Brillouin function best fit (red curve in Figure 4.4b) to the integrated MCD intensity has achieved for the $S = 1$ and $g_S = 2.002$. Surprisingly, the net spin state is 1 rather than 1/2 which could correspond to isolated non-interacting oxygen-vacancy sites. It could be hypothesized that two oxygen vacancy-trapped electrons are localized around two nearest-neighbour ions to form a triplet ground state, leading to the net spin state equal to 1. The same effect also showed in TiO_2 NCs, where a pair of exchange-coupled Ti^{3+} ions give the net spin state of 1.[116] In Figure 4.4c, it can be clearly observed that the MCD intensity drops steeply when heating up from 5 to 20 K, while declines gradually for temperatures above 50 K. The decay follows the Curie-Weiss law (red curve in Figure 4.4d) which reveals the presence of ground-state splitting attributed to sufficient amounts of oxygen vacancies existing in SnO_2 NCs.

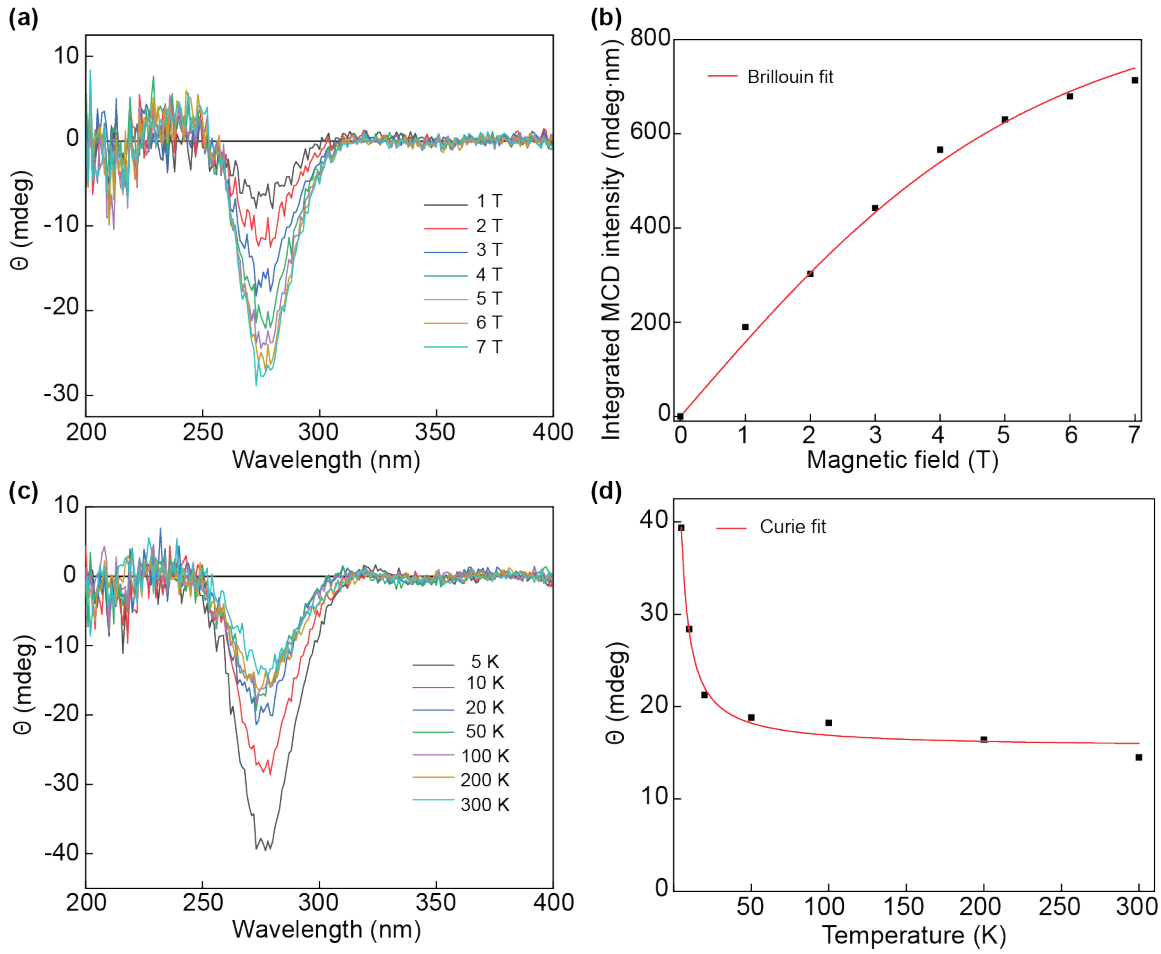

Figure 4.4 (a) MCD spectra of solvothermally-synthesized SnO_2 NCs recorded at 5 K for different external magnetic fields. (b) Magnetic-field dependence of integrated MCD intensity for SnO_2 NCs in (a). Red line is the best fit of the integrated excitonic intensity with the Brillouin function for $S = 1$. (c) MCD spectra collected at 7 T for varying temperatures of solvothermally-synthesized SnO_2 NCs. (d) Temperature dependence of integrated MCD intensity for SnO_2 NCs in (c). Red line is the best fit of the Curie-Weiss law to the corresponding experimental data points.

4.2.2 Carrier Polarization and Optical Properties of Coprecipitation-Synthesized SnO_2 NCs

To further study this carrier polarization, we also recorded the MCD spectra for coprecipitation-prepared SnO_2 NCs. Figure 4.5a shows that the variable-field MCD spectra collected at 5 K, and a strong single-signed MCD signal appears, which is similar to the MCD signal of solvothermally-prepared SnO_2 NCs, pointing out the polarization of excitons. And a sign of saturation is revealed at a high external magnetic field. As shown in Figure 4.5b, the integrated MCD intensity data points are plotted as the best fit (green line) combing the linear and Brillouin functions. In this case, the net spin sate is considered as 1, which is consistent with that of solvothermally-prepared SnO_2 NCs. In Figure 4.5c, a relatively slight MCD intensity decay occurs when heating the sample, and this decay also follows the Curie-Weiss law (red line in Figure 4.5d), confirming the Curie-type paramagnetism and indicating the existence of ground-state splitting in coprecipitation-synthesized SnO_2 NCs as well. Taken together MCD spectra of both types of SnO_2 NCs gives evidence that the defect induced band splitting is a general phenomenon in SnO_2 NCs, although the saturation and Curie-type paramagnetism of the solvothermally-synthesized NCs are not as strong as those prepared by coprecipitation method due to the relatively small concentration of unpaired localized electrons associated with oxygen vacancies.

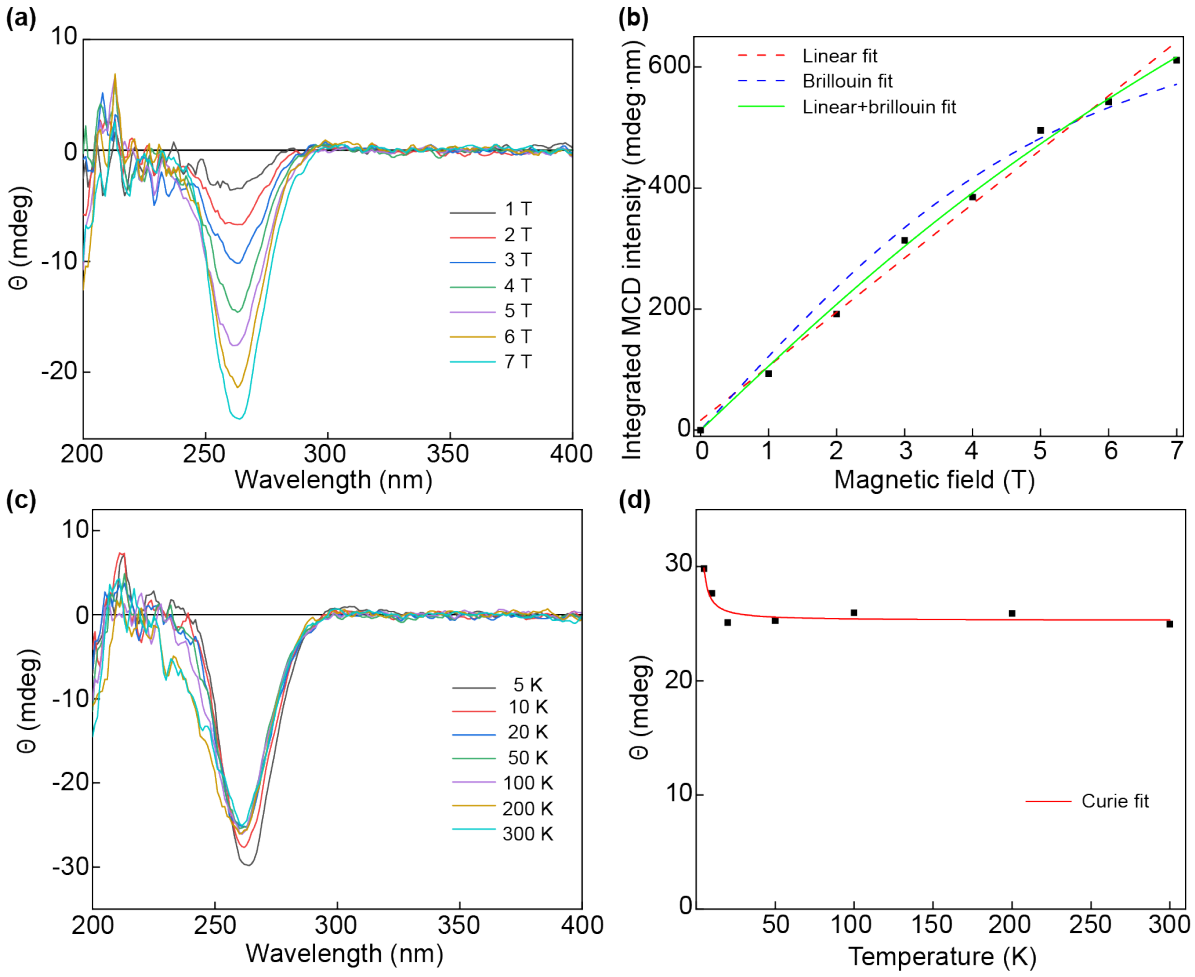

Figure 4.5 (a) MCD spectra of coprecipitation-synthesized SnO_2 NCs recorded at 5 K for various external magnetic fields. (b) Magnetic-field dependence of integrated MCD intensity for SnO_2 NCs in (a). Dashed red line is the best fit of the integrated excitonic intensity with a linear function. Dashed blue line is the best fit of the integrated excitonic intensity with the Brillouin function for $S = 1$. Green line is the best fit of the integrated excitonic intensity with a combination of the linear and Brillouin function for $S = 1$. (c) MCD spectra collected at 7 T for varying temperatures of coprecipitation-synthesized SnO_2 NCs. (d) Temperature dependence of integrated MCD intensity for SnO_2 NCs in (c). Red line is the best fit of the Curie-Weiss law to the corresponding experimental data points.

To investigate the post-processing effect on the defects in NCs, we annealed the coprecipitation-synthesized SnO_2 NCs at 500 ℃ for 2 hours followed by MCD measurement at the temperature of 5 K and the external magnetic field of 7 T. As shown in Figure 4.6a, the absolute value of the peak intensity in MCD spectra has a significant decrease after annealing (red trace), which drops almost twice compared to those without annealing processing (black trace). Furthermore, the PL emission spectra were collected for SnO_2 NCs synthesized by coprecipitation method. In Figure 4.6b, a broad PL peak with the maximum at ca. 530 nm appears for the NCs before annealing (black trace), which is presumed to be generated by the combination of singly charged oxygen vacancies and neutral oxygen vacancies.[101,117] However, the peak is fully quenched after annealing (red trace). This PL result is in agreement with MCD spectra and demonstrates that defect-related emission was diminished, together with the reduction in paramagnetic behaviour of unpaired localized electrons due to the insufficiency of oxygen vacancies for SnO_2 NCs synthesized in the oxygen-rich atmosphere and post-processed with thermal annealing.

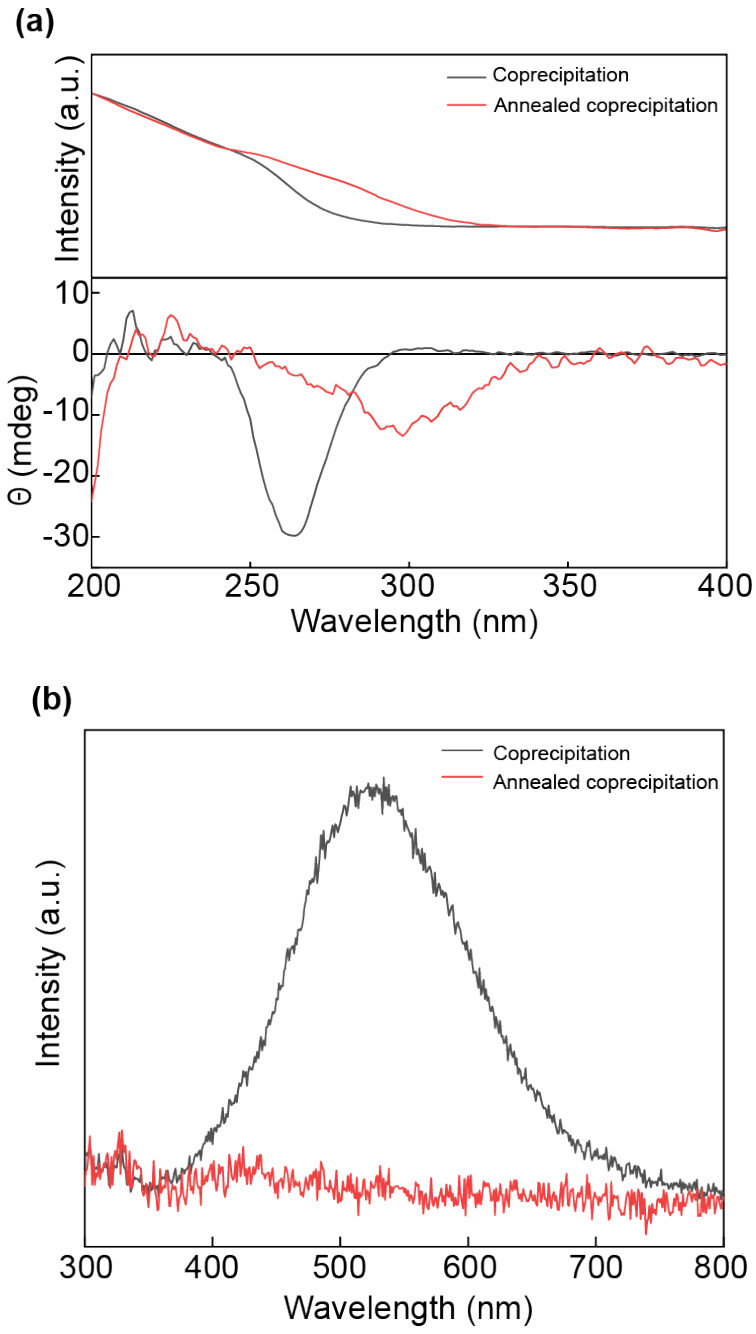

Figure 4.6 (a) Absorption (top panel) and MCD (bottom panel) spectra of coprecipitation-synthesized SnO_2 NCs before (black solid lines) and after (red solid lines) thermal annealing, recorded at 5 K and 7 T. (b) PL emission spectra of coprecipitation-synthesized SnO_2 NCs before (black trace) and after (red trace) thermal annealing, with the excitation wavelength of 240 nm.

According to the result, we obtained from Figure 4.7, oxygen vacancies in the coprecipitation-synthesized SnO_2 NCs have been filled up after thermal annealing. In this scenario, there should be no (or very few) unpaired localized electrons inside the lattice. A straightforward way to demonstrate this effect is by measuring the temperature-dependent MCD spectra. The blue and green lines in Figure 4.7 (bottom panel) show the excitonic MCD signals collected at 7 T and 5 and 300 K, respectively. The MCD spectra display negative bands which coincide with their band edge absorption (top panel in Figure 4.7). As expected, the Curie-type decay disappears and MCD intensities in both temperatures are practically the same. The result is a further proof of the validity of our hypothesis that the excitonic splitting in SnO_2 NCs is generated by unpaired electrons which are localized in oxygen vacancies, and the splitting could be manipulated by means of post-synthesis treatments such as thermal annealing.

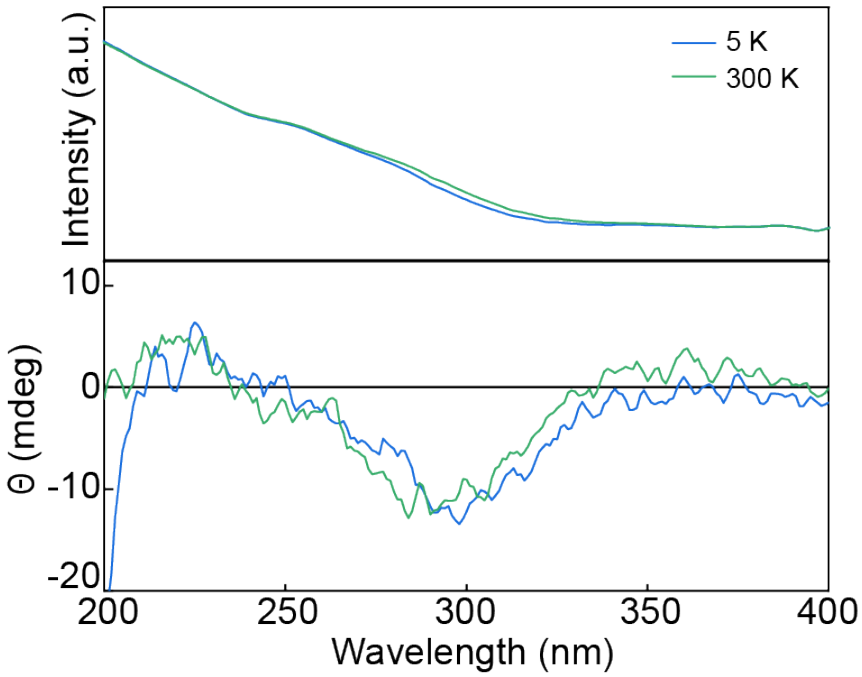

Figure 4.7 Absorption (top panel) and MCD (bottom panel) spectra recorded at 7 T under 5 and 300 K (blue and green curves, respectively) for coprecipitation-prepared SnO_2 NCs annealed at 500 °C for 2 hours.

4.3 Conclusions

In summary, we reported the excitonic splitting produced by oxygen vacancies in ZnO and SnO_2 NCs. The colloidally-synthesized ZnO NCs and solvothermally- as well as coprecipitation-synthesized SnO_2 NCs were successfully prepared and their morphology, optical, and magneto-optical properties were evaluated. For ZnO NCs synthesized under reducing atmosphere, the defect-related PL emission is observed and synchronistically, the excitonic splitting caused by the singly charged oxygen vacancies with a strong Curie-type

decay are detected through the MCD measurements. To the contrary, neither paramagnetic polarization nor discernable PL emission in the visible range are revealed for the ZnO NCs prepared and post-treated under oxidizing conditions, which indicates that oxygen vacancies are saturated in the oxygen-rich atmosphere and consequently, the defect-induced PL emission disappears and carrier polarization would no longer be produced by singly ionized oxygen vacancies as only V_O^+ state is paramagnetic and can induce unpaired electrons.[117] In analogy to ZnO NCs, SnO_2 NCs also show paramagnetic properties without external magnetic impurities. Moreover, we can control the defect concentration and thus paramagnetism *via* synthesis conditions and post-synthesis treatment. The results of this work demonstrate for the first time that oxygen vacancies can lead to the excitonic band splitting without magnetic ion doping into ZnO and SnO_2 semiconductor NCs. This novel outcome enables applications of spintronics and related quantum technologies more promising.

Future Work

In this thesis, we reported the role of the synthesis approach and post-synthesis treatment on the plasmonic properties of Sb-doped SnO_2 NCs. We have measured the MCD spectra of coprecipitation-prepared SnO_2 NCs for varying annealing time at 300 K and 7 T. However, it is necessary to measure MCD signal for SnO_2 NCs prepared in both ways at low temperature and high magnetic field, which will present a more direct and accurate result showing the dependence on plasmonic properties related to synthesis approach. Additionally, due to the limit of our spectrometer, we did not observe the LSPR in ATO NCs synthesized by coprecipitation method, while we detected the excitonic MCD signal, indicating there exists plasmonic absorption but too weak and broad. Hence it is helpful to utilize a blackbody infrared light source to record the faint LSPR. Furthermore, it is also important to thoroughly understand the mechanism of the plasmon-exciton coupling by expanding the library of plasmonic materials.

The intrinsic origin of defect-induced paramagnetism is still controversial due to the complexity of the ZnO system, and more work needs to be performed to determine this mechanism. It can be more straightforward and convincing if magnetic-field-dependent MCD measurement would be done for annealed ZnO NCs prepared in an oxidizing atmosphere. Moreover, we demonstrated the defect-related carrier polarization and band splitting in ZnO and SnO_2 NCs. It is necessary to investigate more metal oxide samples to extend this generality, which may provide with new ideas in applications of spintronics.

Bibliography

(1) Agrawal, A.; Cho, S. H.; Zandi, O.; Ghosh, S.; Johns, R. W.; Milliron, D. J. Localized Surface Plasmon Resonance in Semiconductor Nanocrystals. *Chem. Rev.* **2018**, *118* (6), 3121–3207.

(2) Stockman, M. I.; Kneipp, K.; Bozhevolnyi, S. I.; Saha, S.; Dutta, A.; Ndukaife, J.; Kinsey, N.; Reddy, H.; Guler, U.; Shalaev, V. M.; Boltasseva, A.; Gholipour, B.; Krishnamoorthy, H. N. S.; MacDonald, K. F.; Soci, C.; Zheludev, N. I.; Savinov, V.; Singh, R.; Groß, P.; Lienau, C.; Vadai, M.; Solomon, M. L.; Barton, D. R.; Lawrence, M.; Dionne, J. A.; Boriskina, S. V.; Esteban, R.; Aizpurua, J.; Zhang, X.; Yang, S.; Wang, D.; Wang, W.; Odom, T. W.; Accanto, N.; de Roque, P. M.; Hancu, I. M.; Piatkowski, L.; van Hulst, N. F.; Kling, M. F. Roadmap on Plasmonics. *J. Opt.* **2018**, *20* (4), 043001.

(3) Stauffer, M. *Applications of Molecular Spectroscopy to Current Research in the Chemical and Biological Sciences.* IntechOpen, **2016**.

(4) Homola, J.; Yee, S. S.; Gauglitz, G. Surface Plasmon Resonance Sensors: Review. *Sens. Actuators B Chem.* **1999**, *54* (1), 3–15.

(5) Rycenga, M.; Cobley, C. M.; Zeng, J.; Li, W.; Moran, C. H.; Zhang, Q.; Qin, D.; Xia, Y. Controlling the Synthesis and Assembly of Silver Nanostructures for Plasmonic Applications. *Chem. Rev.* **2011**, *111* (6), 3669–3712.

(6) Stewart, M. E.; Anderton, C. R.; Thompson, L. B.; Maria, J.; Gray, S. K.; Rogers, J. A.; Nuzzo, R. G. Nanostructured Plasmonic Sensors. *Chem. Rev.* **2008**, *108* (2), 494–521.

(7) Sheldon, M. T.; van de Groep, J.; Brown, A. M.; Polman, A.; Atwater, H. A. Nanophotonics. Plasmoelectric Potentials in Metal Nanostructures. *Science* **2014**, *346* (6211), 828–831.

(8) Auguié, B.; Barnes, W. L. Collective Resonances in Gold Nanoparticle Arrays. *Phys. Rev. Lett.* **2008**, *101* (14).

(9) Comin, A.; Manna, L. New Materials for Tunable Plasmonic Colloidal Nanocrystals. *Chem. Soc. Rev.* **2014**, *43* (11), 3957–3975.

(10) Garcia, G.; Buonsanti, R.; Runnerstrom, E. L.; Mendelsberg, R. J.; Llordes, A.; Anders, A.; Richardson, T. J.; Milliron, D. J. Dynamically Modulating the Surface Plasmon Resonance of Doped Semiconductor Nanocrystals. *Nano Lett.* **2011**, *11* (10), 4415–4420.

(11) Hergert, W.; Wriedt, T. *The Mie Theory: Basics and Applications*. Springer, **2012**.

(12) Mulvaney, P. Surface Plasmon Spectroscopy of Nanosized Metal Particles. *Langmuir* **1996**, *12* (3), 788–800.

(13) Nütz, T.; Felde, U. zum; Haase, M. Wet-Chemical Synthesis of Doped Nanoparticles: Blue-Colored Colloids of n-Doped SnO_2:Sb. *J. Chem. Phys.* **1999**, *110* (24), 12142–12150.

(14) Naik, G.; Boltasseva, A. Plasmonics and Metamaterials: Looking beyond Gold and Silver. *SPIE Newsroom* **2012**, 3–5.

(15) Mendelsberg, R. J.; Garcia, G.; Milliron, D. J. Extracting Reliable Electronic Properties from Transmission Spectra of Indium Tin Oxide Thin Films and Nanocrystal Films by Careful Application of the Drude Theory. *J. Appl. Phys.* **2012**, *111* (6), 063515.

(16) Zhong, Y.; Malagari, S. D.; Hamilton, T.; Wasserman, D. M. Review of Mid-Infrared Plasmonic Materials. *JNP* **2015**, *9* (1), 093791.

(17) Niezgoda, J. S.; Rosenthal, S. J. Synthetic Strategies for Semiconductor Nanocrystals Expressing Localized Surface Plasmon Resonance. *ChemPhysChem* **2016**, *17* (5), 645–653.

(18) Underwood, S.; Mulvaney, P. Effect of the Solution Refractive Index on the Color of Gold Colloids. *Langmuir* **1994**, *10* (10), 3427–3430.

(19) Fang, H.; Hegde, M.; Yin, P.; Radovanovic, P. V. Tuning Plasmon Resonance of In_2O_3 Nanocrystals throughout the Mid-Infrared Region by Competition between Electron Activation and Trapping. *Chem. Mater.* **2017**, *29* (11), 4970–4979.

(20) Yin, P.; Tan, Y.; Fang, H.; Hegde, M.; Radovanovic, P. V. Plasmon-Induced Carrier Polarization in Semiconductor Nanocrystals. *Nat. Nanotechnol.* **2018**, *13* (6), 463–467.

(21) Luther, J. M.; Jain, P. K.; Ewers, T.; Alivisatos, A. P. Localized Surface Plasmon Resonances Arising from Free Carriers in Doped Quantum Dots. *Nat. Mater.* **2011**, *10* (5), 361–366.

(22) Lounis, S. D.; Runnerstrom, E. L.; Llordés, A.; Milliron, D. J. Defect Chemistry and Plasmon Physics of Colloidal Metal Oxide Nanocrystals. *J. Phys. Chem. Lett.* **2014**, *5* (9), 1564–1574.

(23) Gerlach, E. Carrier Scattering and Transport in Semiconductors Treated by the Energy-Loss Method. *J. Phys. Condens. Matter* **1986**, *19* (24), 4585–4603.

(24) Donovan, B. F.; Sachet, E.; Maria, J.-P.; Hopkins, P. E. Interplay between Mass-Impurity and Vacancy Phonon Scattering Effects on the Thermal Conductivity of Doped Cadmium Oxide. *Appl. Phys. Lett.* **2016**, *108* (2), 021901.

(25) Chattopadhyay, D.; Queisser, H. J. Electron Scattering by Ionized Impurities in Semiconductors. *Rev. Mod. Phys.* **1981**, *53* (4), 745–768.

(26) V. Besteiro, L.; Kong, X.-T.; Wang, Z.; Rosei, F.; Govorov, A. O. Plasmonic Glasses and Films Based on Alternative Inexpensive Materials for Blocking Infrared Radiation. *Nano Lett.* **2018**, *18* (5), 3147-3156.

(27) Hwang, J.-H.; Edwards, D. D.; Kammler, D. R.; Mason, T. O. Point Defects and Electrical Properties of Sn-Doped In-Based Transparent Conducting Oxides. *Solid State Ionics* **2000**, *1–4* (129), 135–144.

(28) Tandon, B.; Yadav, A.; Khurana, D.; Reddy, P.; Santra, P. K.; Nag, A. Size-Induced Enhancement of Carrier Density, LSPR Quality Factor, and Carrier Mobility in Cr-Sn Doped In_2O_3 Nanocrystals. *Chem. Mater.* **2017**, *29* (21), 9360–9368.

(29) Crockett, B. M.; Jansons, A. W.; Koskela, K. M.; Sharps, M. C.; Johnson, D. W.; Hutchison, J. E. Influence of Nanocrystal Size on the Optoelectronic Properties of Thin, Solution-Cast Sn-Doped In_2O_3 Films. *Chem. Mater.* **2019**, *31* (9), 3370–3380.

(30) Wang, T.; Radovanovic, P. V. Free Electron Concentration in Colloidal Indium Tin Oxide Nanocrystals Determined by Their Size and Structure. *J. Phys. Chem. C* **2011**, *115* (2), 406–413.

(31) Zandi, O.; Agrawal, A.; Shearer, A. B.; Reimnitz, L. C.; Dahlman, C. J.; Staller, C. M.; Milliron, D. J. Impacts of Surface Depletion on the Plasmonic Properties of Doped Semiconductor Nanocrystals. *Nat. Mater.* **2018**, *17* (8), 710–717.

(32) Johns, R. W.; Bechtel, H. A.; Runnerstrom, E. L.; Agrawal, A.; Lounis, S. D.; Milliron, D. J. Direct Observation of Narrow Mid-Infrared Plasmon Linewidths of Single Metal Oxide Nanocrystals. *Nat. Commun.* **2016**, *7* (1), 11583.

(33) Runnerstrom, E. L.; Bergerud, A.; Agrawal, A.; Johns, R. W.; Dahlman, C. J.; Singh, A.; Selbach, S. M.; Milliron, D. J. Defect Engineering in Plasmonic Metal Oxide Nanocrystals. *Nano Lett.* **2016**, *16* (5), 3390–3398.

(34) Lounis, S. D.; Runnerstrom, E. L.; Bergerud, A.; Nordlund, D.; Milliron, D. J. Influence of Dopant Distribution on the Plasmonic Properties of Indium Tin Oxide Nanocrystals. *J. Am. Chem. Soc.* **2014**, *136* (19), 7110–7116.

(35) Dorfs, D.; Härtling, T.; Miszta, K.; Bigall, N. C.; Kim, M. R.; Genovese, A.; Falqui, A.; Povia, M.; Manna, L. Reversible Tunability of the Near-Infrared Valence Band Plasmon Resonance in $Cu_{2-X}Se$ Nanocrystals. *J. Am. Chem. Soc.* **2011**, *133* (29), 11175–11180.

(36) Mendelsberg, R. J.; McBride, P. M.; Duong, J. T.; Bailey, M. J.; Llordes, A.; Milliron, D. J.; Helms, B. A. Dispersible Plasmonic Doped Metal Oxide Nanocrystal Sensors That Optically Track Redox Reactions in Aqueous Media with Single-Electron Sensitivity. *Adv. Opt. Mater.* **2015**, *3* (9), 1293–1300.

(37) Schimpf, A. M.; Ochsenbein, S. T.; Buonsanti, R.; Milliron, D. J.; Gamelin, D. R. Comparison of Extra Electrons in Colloidal N-Type Al^{3+}-Doped and Photochemically Reduced ZnO Nanocrystals. *Chem. Commun.* **2012**, *48* (75), 9352–9354.

(38) Cohn, A. W.; Janßen, N.; Mayer, J. M.; Gamelin, D. R. Photocharging ZnO Nanocrystals: Picosecond Hole Capture, Electron Accumulation, and Auger Recombination. *J. Phys. Chem. C* **2012**, *116* (38), 20633–20642.

(39) Shim, M.; Guyot-Sionnest, P. Organic-Capped ZnO Nanocrystals: Synthesis and n-Type Character. *J. Am. Chem. Soc.* **2001**, *123* (47), 11651–11654.

(40) Faucheaux, J. A.; Jain, P. K. Plasmons in Photocharged ZnO Nanocrystals Revealing the Nature of Charge Dynamics. *J. Phys. Chem. Lett.* **2013**, *4* (18), 3024–3030.

(41) Llorente, V. B.; Dzhagan, V. M.; Gaponik, N.; Iglesias, R. A.; Zahn, D. R. T.; Lesnyak, V. Electrochemical Tuning of Localized Surface Plasmon Resonance in Copper Chalcogenide Nanocrystals. *J. Phys. Chem. C* **2017**, *121* (33), 18244–18253.

(42) Li, Y. *Plasmonic Optics: Theory and Applications*. SPIE, **2017**.

(43) Grahn, H. T. *Introduction to Semiconductor Physics*. World Scientific Publishing Company, **1999**.

(44) West, A. R. *Solid State Chemistry and Its Applications*. John Wiley & Sons, **2014**.

(45) Erwin, S. C.; Zu, L.; Haftel, M. I.; Efros, A. L.; Kennedy, T. A.; Norris, D. J. Doping Semiconductor Nanocrystals. *Nature* **2005**, *436* (7047), 91–94.

(46) Schimpf, A. M.; Knowles, K. E.; Carroll, G. M.; Gamelin, D. R. Electronic Doping and Redox-Potential Tuning in Colloidal Semiconductor Nanocrystals. *Acc. Chem. Res.* **2015**, *48* (7), 1929–1937.

(47) Agoston, P.; Erhart, P.; Klein, A.; Albe, K. Geometry, Electronic Structure and Thermodynamic Stability of Intrinsic Point Defects in Indium Oxide. *J. Phys. Condens. Matter* **2009**, *21* (45), 455801.

(48) Elimelech, O.; Liu, J.; Plonka, A. M.; Frenkel, A. I.; Banin, U. Size Dependence of Doping by a Vacancy Formation Reaction in Copper Sulfide Nanocrystals. *Angew. Chem. Int. Ed. Engl.* **2017**, *56* (35), 10335–10340.

(49) Mączka, M.; Sieradzki, A.; Bondzior, B.; Dereń, P.; Hanuza, J.; Hermanowicz, K. Effect of Aliovalent Doping on the Properties of Perovskite-like Multiferroic Formates. *J. Mater. Chem. C* **2015**, *3* (36), 9337–9345.

(50) Buonsanti, R.; Milliron, D. J. Chemistry of Doped Colloidal Nanocrystals. *Chem. Mater.* **2013**, *25* (8), 1305–1317.

(51) Chong, S. K.; Azizan, S. N. A.; Chan, K. W.; Nguyen, H.-Q.; Chiu, W. S.; Aspanut, Z.; Dee, C. F.; Rahman, S. A. Structure Deformation of Indium Oxide from Nanoparticles into Nanostructured Polycrystalline Films by in Situ Thermal Radiation Treatment. *Nanoscale Res. Lett.* **2013**, *8* (1), 428.

(52) Mendelsberg, R. J.; Zhu, Y.; Anders, A. Determining the Nonparabolicity Factor of the CdO Conduction Band Using Indium Doping and the Drude Theory. *J. Phys. D: Appl. Phys.* **2012**, *45* (42), 425302.

(53) Sachet, E.; Losego, M. D.; Guske, J.; Franzen, S.; Maria, J.-P. Mid-Infrared Surface Plasmon Resonance in Zinc Oxide Semiconductor Thin Films. *Appl. Phys. Lett.* **2013**, *102* (5), 051111.

(54) Goings, J. J.; Schimpf, A. M.; May, J. W.; Johns, R. W.; Gamelin, D. R.; Li, X. Theoretical Characterization of Conduction-Band Electrons in Photodoped and Aluminum-Doped Zinc Oxide (AZO) Quantum Dots. *J. Phys. Chem. C* **2014**, *118* (46), 26584–26590.

(55) Chen, A.; Zhu, K.; Zhong, H.; Shao, Q.; Ge, G. A New Investigation of Oxygen Flow Influence on ITO Thin Films by Magnetron Sputtering. *Sol. Energy Mater. Sol. Cells* **2014**, *120*, 157–162.

(56) Hu, H.; Ji, H.-F.; Sun, Y. The Effect of Oxygen Vacancies on Water Wettability of a ZnO Surface. *Phys. Chem. Chem. Phys.* **2013**, *15* (39), 16557–16565.

(57) Kim, J.; Agrawal, A.; Krieg, F.; Bergerud, A.; Milliron, D. J. The Interplay of Shape and Crystalline Anisotropies in Plasmonic Semiconductor Nanocrystals. *Nano Lett.* **2016**, *16* (6), 3879–3884.

(58) Gabka, G.; Bujak, P.; Ostrowski, A.; Tomaszewski, W.; Lisowski, W.; Sobczak, J. W.; Pron, A. Cu–Fe–S Nanocrystals Exhibiting Tunable Localized Surface Plasmon Resonance in the Visible to NIR Spectral Ranges. *Inorg. Chem.* **2016**, *55* (13), 6660–6669.

(59) Huang, Y.-C.; Yang, Z.-L.; Hsieh, P.-L.; Huang, M. H. Size-Tunable Cu_3Se_2 Nanocubes Possessing Surface Plasmon Resonance Properties for Photothermal Applications. *ACS Appl. Nano Mater.* **2020**, *3* (8), 8446–8452.

(60) Shen, G.; Guyot-Sionnest, P. HgS and HgS/CdS Colloidal Quantum Dots with Infrared Intraband Transitions and Emergence of a Surface Plasmon. *J. Phys. Chem. C* **2016**, *120* (21), 11744–11753.

(61) Chen, M.; Guyot-Sionnest, P. Reversible Electrochemistry of Mercury Chalcogenide Colloidal Quantum Dot Films. *ACS Nano* **2017**, *11* (4), 4165–4173.

(62) Coughlan, C.; Ibáñez, M.; Dobrozhan, O.; Singh, A.; Cabot, A.; Ryan, K. M. Compound Copper Chalcogenide Nanocrystals. *Chem. Rev.* **2017**, *117* (9), 5865–6109.

(63) Zhao, Y.; Pan, H.; Lou, Y.; Qiu, X.; Zhu, J.; Burda, C. Plasmonic $Cu_{2-x}S$ Nanocrystals: Optical and Structural Properties of Copper-Deficient Copper(I) Sulfides. *J. Am. Chem. Soc.* **2009**, *131* (12), 4253–4261.

(64) Kriegel, I.; Rodríguez-Fernández, J.; Wisnet, A.; Zhang, H.; Waurisch, C.; Eychmüller, A.; Dubavik, A.; Govorov, A. O.; Feldmann, J. Shedding Light on Vacancy-Doped Copper Chalcogenides: Shape-Controlled Synthesis, Optical Properties, and Modeling

of Copper Telluride Nanocrystals with Near-Infrared Plasmon Resonances. *ACS Nano* **2013**, *7* (5), 4367–4377.

(65) Singh, J. Exciton-Phonon Interactions. *Excitation Energy Transfer Processes in Condensed Matter: Theory and Applications*. Springer US, **1994**.

(66) Perebeinos, V.; Tersoff, J.; Avouris, P. Effect of Exciton-Phonon Coupling in the Calculated Optical Absorption of Carbon Nanotubes. *Phys. Rev. Lett.* **2005**, 4.

(67) Krauss, T. D.; Wise, F. W. Raman-Scattering Study of Exciton-Phonon Coupling in PbS Nanocrystals. *Phys. Rev. B* **1997**, *55* (15), 9860–9865.

(68) Mooradian, A.; Wright, G. B. Observation of the Interaction of Plasmons with Longitudinal Optical Phonons in GaAs. *Phys. Rev. Lett.* **1966**, *16* (22), 999–1001.

(69) Faust, A.; Amit, Y.; Banin, U. Phonon–Plasmon Coupling and Active Cu Dopants in Indium Arsenide Nanocrystals Studied by Resonance Raman Spectroscopy. *J. Phys. Chem. Lett.* **2017**, *8* (11), 2519–2525.

(70) Mooradian, A.; McWhorter, A. L. Polarization and Intensity of Raman Scattering from Plasmons and Phonons in Gallium Arsenide. *Phys. Rev. Lett.* **1967**, *19* (15), 849–852.

(71) Yin, P.; Hegde, M.; Tan, Y.; Chen, S.; Garnet, N.; Radovanovic, P. V. Controlling the Mechanism of Excitonic Splitting in In_2O_3 Nanocrystals by Carrier Delocalization. *ACS Nano* **2018**, *12* (11), 11211–11218.

(72) DeLacy, B. G.; Miller, O. D.; Hsu, C. W.; Zander, Z.; Lacey, S.; Yagloski, R.; Fountain, A. W.; Valdes, E.; Anquillare, E.; Soljačić, M.; Johnson, S. G.; Joannopoulos, J. D. Coherent Plasmon-Exciton Coupling in Silver Platelet-J-Aggregate Nanocomposites. *Nano Lett.* **2015**, *15* (4), 2588–2593.

(73) Okamoto, K.; Niki, I.; Shvartser, A.; Narukawa, Y.; Mukai, T.; Scherer, A. Surface-Plasmon-Enhanced Light Emitters Based on InGaN Quantum Wells. *Nat. Mater.* **2004**, *3* (9), 601–605.

(74) Okamoto, K.; Funato, M.; Kawakami, Y.; Tamada, K. High-Efficiency Light Emission by Means of Exciton–Surface-Plasmon Coupling. *JPPC* **2017**, *32*, 58–77.

(75) Lee, J.; Hernandez, P.; Lee, J.; Govorov, A. O.; Kotov, N. A. Exciton-Plasmon Interactions in Molecular Spring Assemblies of Nanowires and Wavelength-Based Protein Detection. *Nat. Mater.* **2007**, *6* (4), 291–295.

(76) Zhang, J.; Tang, Y.; Lee, K.; Ouyang, M. Tailoring Light–Matter–Spin Interactions in Colloidal Hetero-Nanostructures. *Nature* **2010**, *466* (7302), 91–95.

(77) Beye, M.; Hennies, F.; Deppe, M.; Suljoti, E.; Nagasono, M.; Wurth, W.; Föhlisch, A. Dynamics of Electron-Phonon Scattering: Crystal- and Angular-Momentum Transfer Probed by Resonant Inelastic X-Ray Scattering. *Phys. Rev. Lett.* **2009**, *103* (23), 237401.

(78) Wolf, S. A.; Awschalom, D. D.; Buhrman, R. A.; Daughton, J. M.; Molnár, S. von; Roukes, M. L.; Chtchelkanova, A. Y.; Treger, D. M. Spintronics: A Spin-Based Electronics Vision for the Future. *Science* **2001**, *294* (5546), 1488–1495.

(79) Furdyna, J. K. Diluted Magnetic Semiconductors. *J. Appl. Phys.* **1988**, *64* (4), R29–R64.

(80) Hegde, M.; Farvid, S. S.; Hosein, I. D.; Radovanovic, P. V. Tuning Manganese Dopant Spin Interactions in Single GaN Nanowires at Room Temperature. *ACS Nano* **2011**, *5* (8), 6365–6373.

(81) Farvid, S. S.; Hegde, M.; Hosein, I. D.; Radovanovic, P. V. Electronic Structure and Magnetism of Mn Dopants in GaN Nanowires: Ensemble vs Single Nanowire Measurements. *Appl. Phys. Lett.* **2011**, *99* (22), 222504.

(82) Radovanovic, P. V.; Stamplecoskie, K. G.; Pautler, B. G. Dopant Ion Concentration Dependence of Growth and Faceting of Manganese-Doped GaN Nanowires. *J. Am. Chem. Soc.* **2007**, *129* (36), 10980–10981.

(83) Lekshmy, S. N. S.; Anitha, V. S. N.; Thomas, P. V.; Joy, K. Magnetic Properties of Mn-doped SnO_2 Thin Films Prepared by the Sol–Gel Dip Coating Method for Dilute Magnetic Semiconductors. *J. Am. Ceram. Soc.* **2014**, *10* (97), 3184–3191.

(84) Coey, J. M. D.; Venkatesan, M.; Fitzgerald, C. B. Donor Impurity Band Exchange in Dilute Ferromagnetic Oxides. *Nat. Mater.* **2005**, *4* (2), 173–179.

(85) Babu, S. H.; Rao, N. M.; Kaleemulla, S.; Amarendra, G.; Krishnamoorthi, C. Room-Temperature Ferromagnetic and Photoluminescence Properties of Indium–Tin-Oxide Nanoparticles Synthesized by Solid-State Reaction. *Bull. Mater. Sci.* **2017**, *40* (1), 17–23.

(86) Orlov, A. F.; Balagurov, L. A.; Konstantinova, A. S.; Perov, N. S.; Yarkin, D. G. Giant Magnetic Moments in Dilute Magnetic Semiconductors. *J. Magn. Magn. Mater.* **2008**, *320* (6), 895–897.

(87) Ando, K. Seeking Room-Temperature Ferromagnetic Semiconductors. *Science* **2006**, *312* (5782), 1883–1885.

(88) Han, B.; Gao, X.; Lv, J.; Tang, Z. Magnetic Circular Dichroism in Nanomaterials: New Opportunity in Understanding and Modulation of Excitonic and Plasmonic Resonances. *Adv. Mater.* **2020**, *32* (41), 1801491.

(89) Ghodsi, V.; Radovanovic, P. V. Turning Weakly Luminescent SnO_2 Nanocrystals into Tunable and Efficient Light Emitters by Aliovalent Alloying. *Chem. Mater.* **2018**, *30* (10), 3578–3587.

(90) Raju, M. J. S.; Bhattacharya, S. S. Structural and Optical Properties of Nanocrystalline Pure and Indium Doped Tin Oxide Powders Synthesized in a Single Step by Flame Spray Pyrolysis. *Mater. Res. Express* **2017**, *4* (7), 075034.

(91) Kılıç, Ç.; Zunger, A. Origins of Coexistence of Conductivity and Transparency in SnO_2. *Phys. Rev. Lett.* **2002**, *88* (9), 095501.

(92) Minami, T. Transparent Conducting Oxide Semiconductors for Transparent Electrodes. *Semicond. Sci. Technol.* **2005**, *20* (4), S35–S44.

(93) Sirelkhatim, A.; Mahmud, S.; Seeni, A.; Kaus, N. H. M.; Ann, L. C.; Bakhori, S. K. M.; Hasan, H.; Mohamad, D. Review on Zinc Oxide Nanoparticles: Antibacterial Activity and Toxicity Mechanism. *Nano-Micro Lett.* **2015**, *7* (3), 219–242.

(94) Ong, C. B.; Ng, L. Y.; Mohammad, A. W. A Review of ZnO Nanoparticles as Solar Photocatalysts: Synthesis, Mechanisms and Applications. *Renew. Sustain. Energy Rev.* **2018**, *81*, 536–551.

(95) Lee, K. M.; Lai, C. W.; Ngai, K. S.; Juan, J. C. Recent Developments of Zinc Oxide Based Photocatalyst in Water Treatment Technology: A Review. *Water Res.* **2016**, *88*, 428–448.

(96) Wang, Z. L.; Song, J. Piezoelectric Nanogenerators Based on Zinc Oxide Nanowire Arrays. *Science* **2006**, *312* (5771), 242–246.

(97) Jeem, M.; Zhang, L.; Ishioka, J.; Shibayama, T.; Iwasaki, T.; Kato, T.; Watanabe, S. Tuning Optoelectrical Properties of ZnO Nanorods with Excitonic Defects via Submerged Illumination. *Nano Lett.* **2017**, *17* (3), 2088–2093.

(98) Qi, B.; Ólafsson, S.; Gíslason, H. P. Vacancy Defect-Induced D0 Ferromagnetism in Undoped ZnO Nanostructures: Controversial Origin and Challenges. *Prog. Mater. Sci.* **2017**, *90*, 45–74.

(99) Opel, M.; Goennenwein, S. T. B.; Althammer, M.; Nielsen, K.-W.; Karrer-Müller, E.-M.; Bauer, S.; Senn, K.; Schwark, C.; Weier, C.; Güntherodt, G.; Beschoten, B.; Gross, R. Zinc Oxide -From Dilute Magnetic Doping to Spin Transport. *Phys. Status Solidi B* **2014**, *251* (9), 1700–1709.

(100) Liu, W.; Li, W.; Hu, Z.; Tang, Z.; Tang, X. Effect of Oxygen Defects on Ferromagnetic of Undoped ZnO. *J. Appl. Phys.* **2011**, *110* (1), 013901.

(101) Das, S.; Ghorai, U. K.; Dey, R.; Ghosh, C. K.; Pal, M. Novel Multiple Phosphorescence in Nanostructured Zinc Oxide and Calculations of Correlated Colour Temperature. *Phys. Chem. Chem. Phys.* **2017**, *19* (34), 22995–23006.

(102) Das, S.; Chaudhuri, S.; Maji, S. Ethanol−Water Mediated Solvothermal Synthesis of Cube and Pyramid Shaped Nanostructured Tin Oxide. *J. Phys. Chem. C* **2008**, *112* (16), 6213–6219.

(103) Huang, H.; Ng, M.; Wu, Y.; Kong, L. Solvothermal Synthesis of Sb:SnO_2 Nanoparticles and IR Shielding Coating for Smart Window. *Mater. Des.* **2015**, *88*, 384–389.

(104) Sabergharesou, T.; Wang, T.; Ju, L.; Radovanovic, P. V. Electronic Structure and Magnetic Properties of Sub-3 Nm Diameter Mn-Doped SnO_2 Nanocrystals and Nanowires. *Appl. Phys. Lett.* **2013**, *103* (1), 012401.

(105) Dave, N.; Pautler, B. G.; Farvid, S. S.; Radovanovic, P. V. Synthesis and Surface Control of Colloidal Cr^{3+}-Doped SnO_2 Transparent Magnetic Semiconductor Nanocrystals. *Nanotechnology* **2010**, *21* (13), 134023.

(106) Garnet, N. S.; Ghodsi, V.; Hutfluss, L. N.; Yin, P.; Hegde, M.; Radovanovic, P. V. Probing the Role of Dopant Oxidation State in the Magnetism of Diluted Magnetic Oxides Using Fe-Doped In_2O_3 and SnO_2 Nanocrystals. *J. Phys. Chem. C* **2017**, *121* (3), 1918–1927.

(107) Della Gaspera, E.; Chesman, A. S. R.; van Embden, J.; Jasieniak, J. J. Non-Injection Synthesis of Doped Zinc Oxide Plasmonic Nanocrystals. *ACS Nano* **2014**, *8* (9), 9154–9163.

(108) Holzwarth, U.; Gibson, N. The Scherrer Equation versus the "Debye-Scherrer Equation." *Nat. Nanotechnol.* **2011**, *6* (9), 534–534.

(109) Mahoney, L.; Koodali, R. T. Versatility of Evaporation-Induced Self-Assembly (EISA) Method for Preparation of Mesoporous TiO_2 for Energy and Environmental Applications. *Materials* **2014**, *7* (4), 2697–2746.

(110) Mallika, A. N.; Reddy, A. R.; Reddy, K. V. Annealing Effects on the Structural and Optical Properties of ZnO Nanoparticles with PVA and CA as Chelating Agents. *J. Adv. Ceram.* **2015**, *4* (2), 123–129.

(111) Layek, A.; Yildirim, B.; Ghodsi, V.; Hutfluss, L. N.; Hegde, M.; Wang, T.; Radovanovic, P. V. Dual Europium Luminescence Centers in Colloidal Ga_2O_3

Nanocrystals: Controlled in Situ Reduction of Eu(III) and Stabilization of Eu(II). *Chem. Mater.* **2015**, *27* (17), 6030–6037.

(112) Ghodsi, V.; Layek, A.; Hegde, M.; Yildirim, B.; Radovanovic, P. V. Native Defects Determine Phase-Dependent Photoluminescence Behavior of Eu^{2+} and Eu^{3+} in In_2O_3 Nanocrystals. *Chem. Commun.* **2016**, *52* (23), 4353–4356.

(113) Musino, D.; Rivard, C.; Landrot, G.; Novales, B.; Rabilloud, T.; Capron, I. Hydroxyl Groups on Cellulose Nanocrystal Surfaces Form Nucleation Points for Silver Nanoparticles of Varying Shapes and Sizes. *J. Colloid Interface Sci.* **2021**, *584*, 360–371.

(114) Zhou, D.; Wang, P.; Roy, C. R.; Barnes, M. D.; Kittilstved, K. R. Direct Evidence of Surface Charges in N-Type Al-Doped ZnO. *J. Phys. Chem. C* **2018**, *122* (32), 18596–18602.

(115) Liao, Z.-M.; Zhang, H.-Z.; Zhou, Y.-B.; Xu, J.; Zhang, J.-M.; Yu, D.-P. Surface Effects on Photoluminescence of Single ZnO Nanowires. *Phys. Lett. A* **2008**, *372* (24), 4505–4509.

(116) Yin, P.; Hegde, M.; Garnet, N. S.; Tan, Y.; Radovanovic, P. V. Faceting-Controlled Zeeman Splitting in Plasmonic TiO_2 Nanocrystals. *Nano Lett.* **2019**, *19* (9), 6695–6702.

(117) Gu, F.; Wang, S. F.; Lü, M. K.; Cheng, X. F.; Liu, S. W.; Zhou, G. J.; Xu, D.; Yuan, D. R. Luminescence of SnO_2 Thin Films Prepared by Spin-Coating Method. *J. Cryst. Growth* **2004**, *262* (1), 182–185.